FABRICATION AND TESTING OF NOVEL NANOCOMPOSITES FOR SOLAR-DRIVEN ENVIRONMENTAL AND ENERGY APPLICATIONS

A Thesis

by

MUHAMMAD DANYAL IMAM

Submitted to the Graduate and Professional School of
Texas A&M University
in partial fulfillment of the requirements for the degree of

MASTER OF SCIENCE

Chair of Committee,	Ahmed Abdel-Wahab
Co-Chair of Committee,	Konstantinos Kakosimos
Committee Member,	Mahmood Amani
Head of Department,	Arul Jayaraman

December 2021

Major subject: Chemical Engineering

ABSTRACT

The need to meet the growing energy demands of global society in a sustainable fashion requires the development of techniques and processes to avoid fossil fuel consumption and switch to renewable sources of energy. Environmentally benign wastewater treatment and technologies for alternative fuel production in the form of hydrogen can be achieved via heterogenous photocatalysis, a process based on solar energy. To this end, two distinct photocatalytic materials were developed to address each of the processes described above.

V_2O_5 is a promising candidate for organic contaminant degradation due its narrow band gap, however, its fast electron-hole recombination rate and subsequently low photoactivity hinders its application for degradation purposes. To this end, mirroring the technique used to improve TiO_2 by introducing surface defects in the form of oxygen vacancies has been applied on V_2O_5, forming reduced, or black V_2O_5. SEM and TEM imaging confirm the surface defect formation and predominant growth of the (001) facet, with XRD analysis showing the formation of V_2O_5 phases instead of the darker V_2O_3, reiterating the notion that black V_2O_5 exhibits the dark color due to oxygen vacancy formation and not phase change. XPS analysis confirms the formation of oxygen vacancies, proving the success of the facile reduction technique used and confirming material purity.

Photocatalytic degradation experiments were conducted with methylene blue (MB) as the model contaminant. Typical experiments involved a catalyst dose of 0.5 g/L, 20 ppm MB concentration in solution after adsorptive equilibrium had been established and an incident light intensity of 700 W/m^2. Black V_2O_5 was shown to exhibit a much higher equilibrium adsorptive capacity for MB compared to pristine V_2O_5, and a significantly enhanced photocatalytic dye degradation rate, with the black V_2O_5 material achieving nearly 93% degradation of 20 ppm MB in 1 hour of irradiation

time, compared to only 3%, 58.7%, 62.9% and 81.3% achieved by pristine V_2O_5, ZnO, $pTiO_2$ and $bTiO_2$ respectively. In addition, the degradation kinetics were improved 58-fold after the reduction procedure. The effect of contaminant charge was also studied, with bV_2O_5 achieving 93% degradation of cationic MB, 82% degradation of neutral quinoline yellow and only 34% degradation of methylene orange (MO), confirming the greater affinity of the negatively charged bV_2O_5 surface for cationic species.

For photocatalytic hydrogen production, a cadmium sulfide (CdS) based material was developed, doped with MoS_2 in a one-pot hydrothermal synthesis technique and coupled with multi-walled carbon nanotubes (MWCNTs) as a carbonaceous support. Typical experimental procedure involved a 0.2 g/L catalyst dose added to 25 mL of 0.5 M lactic acid solution (used as the sacrificial reagent) and irradiated with 1 kW/m^2 light intensity. The material exhibiting the highest rate of hydrogen evolution involved a MWCNTs loading of 3% and MoS_2 loading of 5%. Compared to pure CdS, the 3% CNT loading improved the rate of hydrogen production by nearly 7-fold, and the optimal 5% MoS_2 loading further improved the HER performance by 60%. The optimal composite, labelled CM5C3, achieved an apparent quantum efficiency of 26.25%.

SEM and TEM imaging confirmed the nanorod-like growth of CdS – MoS_2 on the CNT surface, with TEM elemental mapping used to confirm good dispersion of MoS_2 and CNTs. In addition, high resolution TEM images showed the presence of cubic and hexagonal CdS growing predominantly along the (111) and (002) planes respectively, in addition to MoS_2 distributed throughout the crystal lattice. XRD analysis confirmed the presence of hexagonal and cubic CdS, however, MoS_2 phases were not registered perhaps due to the low concentration present in the bulk of the material. XPS survey scans showed the presence of C, Cd, Mo, and S only, with trace oxygen impurities. Peak deconvolution indicated the presence of characteristic peaks for CdS and

MoS_2, in addition to evidence of the presence of Cd – C bonds, with strong CdS attachment to the CNT surface.

DEDICATION

To my parents, Muhammad Qaisar Imam and Naila Aftab, for their unquestioning love, support and guidance throughout my life. Their guidance and sacrifices are the reason I stand where I am today, and will continue to be the reason I achieve anything hereafter.

To my siblings, Muhammad Hamza Imam and Ayesha Qaisar, for keeping me in check and ensuring a healthy balance to an otherwise rather rigorous schedule.

To my grandparents and extended family back home in Pakistan. Their prayers and blessings have remained unconditional, and I could not be here without their love and support.

ACKNOWLEDGEMENTS

I would like to acknowledge the immense support and guidance of my advisor, Dr. Ahmed Abdel-Wahab, throughout my graduate studies and research endeavors. His invaluable insights, attention to detail, patience and continuous push for excellence helped shape my research mindset and keep me on track. I would like to thank Dr. Konstantinos Kakosimos for serving as my graduate committee co-chair, guiding my experimental activities and helping me with the reactor set-up. I would also like to acknowledge the unwavering guidance and support I have received from my committee member, Dr. Mahmood Amani, throughout my graduate career thus far.

Additionally, I would like to thank Dr. Kumaravel Vignesh for his guidance related to the theoretical framework of photocatalysis at the start of my research career in addition to all laboratory-based activities. I would like to express my gratitude to members of our research team, Dr. Abdellatif ElGhenymy for his help and support in the laboratory, and Ahmed Badreldin, for his invaluable advice, support, and imparted experience that helped provide answers and alternative routes to the many experimental and theoretical challenges faced throughout this work.

Finally, I would also like to express my appreciation for Dr. Wubulikasimu Yiming at the Central Materials Facility in TAMUQ for conducting all relevant characterization experiments and providing valuable insights aiding this research work.

CONTRIBUTORS AND FUNDING SOURCES

This work was made possible by the financial support provided by Texas A&M University at Qatar. I would like to thank the contributions made by Ahmed Badreldin throughout this work.

TABLE OF CONTENTS

Page

LIST OF FIGURES

Page

LIST OF TABLES

Page

CHAPTER I - INTRODUCTION

The last century, humanity has progressed at a rapid pace in terms of social and economic development. An exponentially growing population coupled with rapid technological growth has not only resulted in a tremendous increase in the demand for energy, but the traditional exploitation of energy sources has placed a severe strain on the global climate. Figure 1 below outlines the distribution of energy sources that are used to satisfy the global energy demand as of 2018.[1]

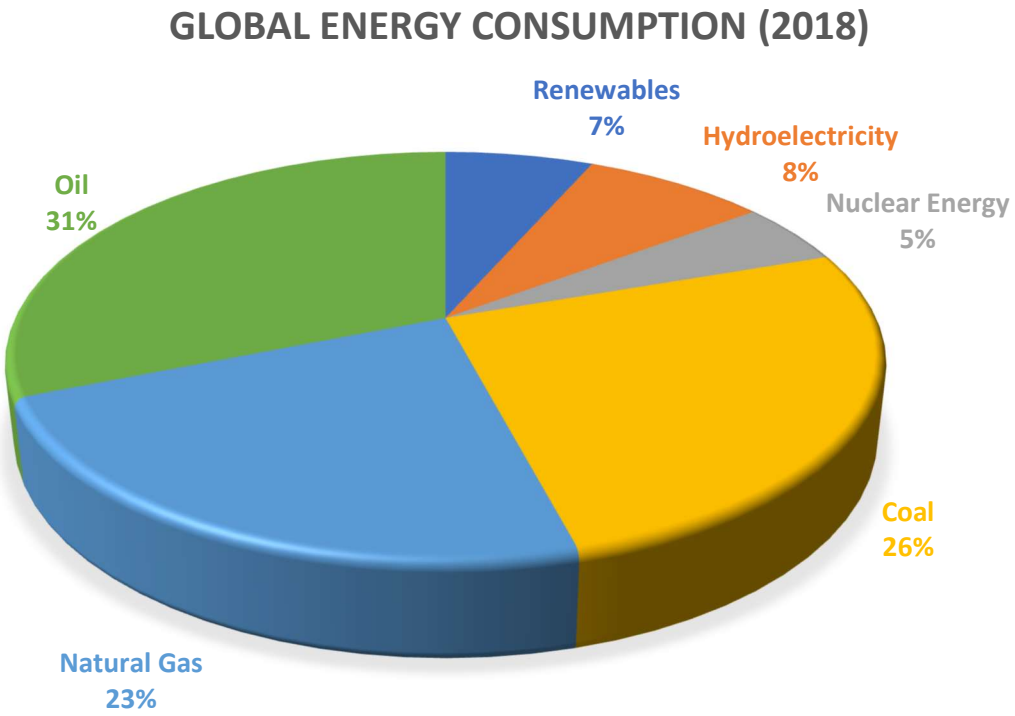

Figure 1: *Global energy consumption (2018), reprinted from BP Statistical Review of World Energy, 2018.*[1]

Fossil fuel consumption has been the main driving force of the rapid industrial growth of the last century in terms of energy supply. As seen from the diagram above, coal, oil and natural gas are still the main constituents of energy sources used today, accounting for nearly 80% of the global energy demand. However, while this approach has allowed for giant industrial, economic and

societal leaps, the continued use of fossil fuels to meet the constantly growing energy demand is not sustainable.

Fossil fuels are composed of organic carbon materials formed over millions of years at high temperatures and pressures deep under the Earth's surface.[2] Naturally, the formation of fossil fuels does not occur on a human time scale, with the effective non-renewable nature of fossil fuels resulting in resource depletion. According to the *BP Statistical Review of World Energy 2016*, currently known reserves of coal and oil are expected to run out in approximately 50 years, with coal reserves estimated to last another 115 years.[3] Even though new fossil fuel reserves are gradually being found, the total energy demand is also increasing at an exponential rate, challenging society to develop alternate fuels in order to avoid an energy vacuum in the near future.

Global climate change is a more immediate threat of the continued use of fossil fuels to meet energy requirements. Combustion of fossil fuels results in the emissions of greenhouse gases, including nitrogen oxides, sulfur oxides, carbon dioxide and carbon monoxide.[4] These greenhouse gases act to trap the sun's incident radiation in the Earth's atmosphere, warming up the planet and making it habitable for human population. However, excessive greenhouse emissions result in continual warming of the planet, resulting in severely adverse environmental effects and endangerment to the lives of all species. In addition, the increasing temperature of the climate has resulted in the melting of ice caps in the Arctic and Antarctic regions, the continued melting of which will result in potential flooding and a drastic impact to humans and agricultural activities.

The most collective effort to addressing the issues of global warming was manifested in the Paris Agreement of 2015, which states that global warming be limited to well below 2 °C above pre-industrial standards, pursuing efforts to limit this increase to 1.5 °C. Figure 2 below outlines the

estimated extent of global warming based on three representative concentration pathways (RCPs), based on models implemented by the Intergovernmental Panel on Climate Change (IPCC).[5]

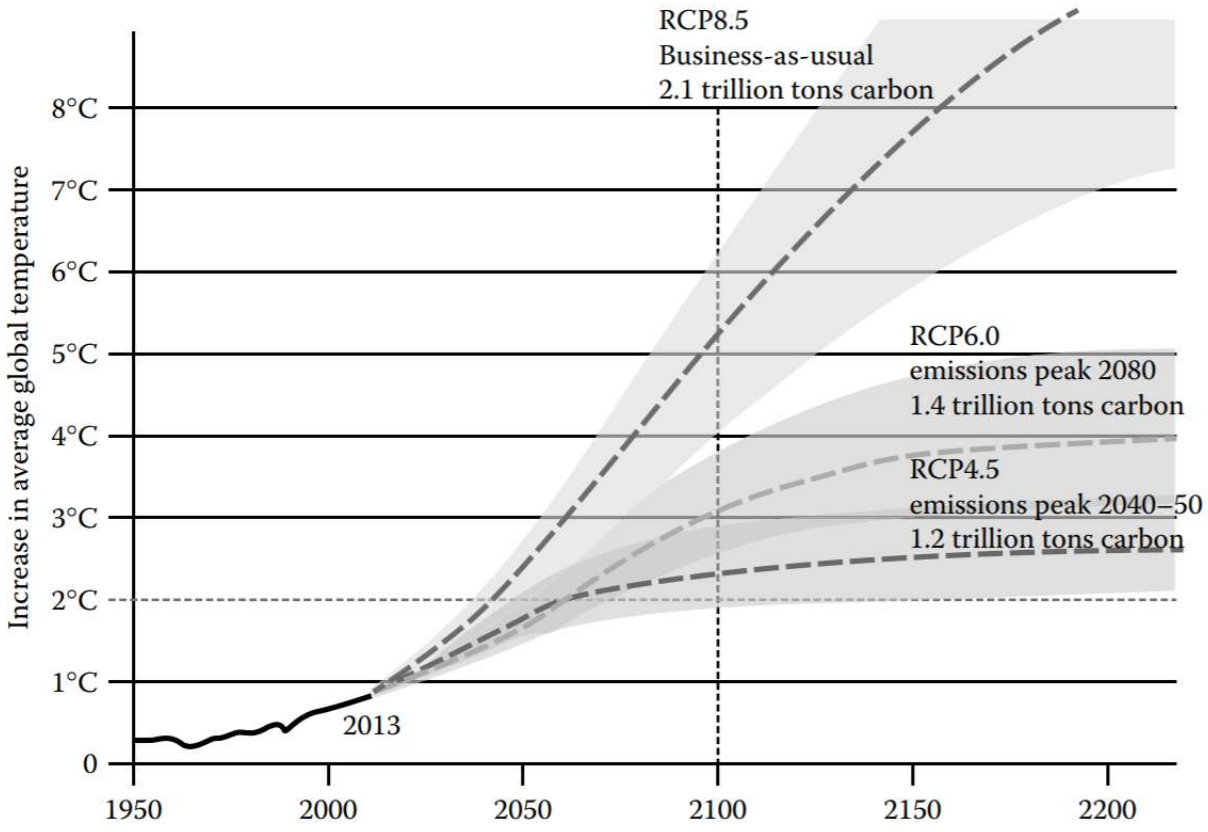

Figure 2: *Estimated global warming based on representative concentration pathways (RCPs), reprinted from O'Dwyer J et al.*[5]

Without any mitigation practices, the increase in average global temperature is expected to surpass 2°C before 2050, and 5°C (beyond catastrophic levels[6]) before the end of the century. The imminent effects of this excessive global warming will involve an increase in the frequency of extreme events such as floods, draughts and storm surges, inducing structural damage and loss of human life, in addition to an increase in the transmission, frequency and dispersion of waterborne infectious diseases.[5] As a result, limiting the effects of global warming becomes of vital

importance, not only to meet the environmental standards agreed upon in the Paris Agreement, but to ensure that humanitarian economic and technological advancement is not hindered due to adverse climate effects.

In the Unites States, 76% of total greenhouse emissions come from fossil fuels.[7] The burning of coal, oil and natural gas, therefore, renders the most significant contribution to global warming effects; limiting their use would provide the most efficient route towards combating climate change. As a result, the development of green, alternate fuels has become an area of considerable interest in modern research environments. Replacing traditional fossil fuels with alternate, carbon-free fuels, will cut off the carbon supply to the combustion process, with the potential to minimize the carbon dioxide and carbon monoxide emissions in industrial processes.

Hydrogen is widely regarded as the fuel for the future due to its emission-free combustion, a process which results in the formation of water as the only by-product, and its significantly higher energy density when compared to traditional fossil fuels.[8] However, the utilization of hydrogen as a fuel source may still incur a high carbon footprint as a result of the processes involved in hydrogen production. Conventional techniques of hydrogen production involve the steam reforming of natural gas, a process which accounts for nearly 95% of the hydrogen produced globally. This technique requires a hydrocarbon source, very high temperatures and incurs a substantial amount of carbon emissions, making the process unsustainable.[9] Other techniques of hydrogen production, such as electrolysis using electricity produced from combustion of fossil fuels, also incurs CO_2 emissions and negates the environmental benefits of utilizing hydrogen as a fuel source.[10]

Solar-hydrogen is deemed to be the way forward because hydrogen produced using solar energy is environmentally friendly, with solar energy available in abundance in most countries. However,

owing to the still low solar-to-chemical energy conversion efficiencies (typically less than 5%)[11] in current solar-driven hydrogen production techniques, the utilization of solar-hydrogen is still in the development phase. This is because the current operational costs still outweigh the benefits of the produced hydrogen and these techniques require significant improvements before solar-hydrogen may be used commercially for industrial and domestic use.

The utilization of solar energy can also be targeted towards other environmental applications. The availability of clean water has become increasingly challenging, due to the increased agricultural, domestic and industrial consumption. There has also been an increase in the level of organic contaminants and pathogens entering the water system due to continuous industrial and municipal activities.[12] The global consumption of water is approximately doubling every two decades owing to population growth[13], making the reuse of treated wastewater of great importance. Qatar faces the same issue: the increasing population coupled with an increased standard of living is creating a gap between demand and supply of clean water.[14]

Domestic wastewater and wastewater effluent from certain industrial plants is typically of a lower salinity than seawater, making it cost effective to treat and reuse for agricultural and industrial purposes. Traditional seawater desalination techniques are energy intensive, and thus costly, processes. Considering the need for alternative water resources at low cost, enhancing traditional wastewater treatment processes to enable greater operating efficiencies and high treated water quality becomes an essential task. Developing alternatives to traditional wastewater treatment techniques involve membrane filtration, with the latest advent in the technology coming in the form of nanofiltration.[15] However, as is the issue with membrane systems, many organic contaminants can result in membrane fouling[15], a phenomenon that may be bypassed by effective pretreatment systems that can remove the organic contaminants prior to the membrane system. In

addition, with growing awareness about emerging contaminants present in trace quantities in modern wastewater systems stemming from industrial activity (pharmaceuticals, fragrances, preservatives, etc)[16], techniques for the environmentally benign degradation of these contaminants need to be developed and implemented, so as to eliminate their chronically toxic effects to aquatic and human health.

Photocatalysis has attracted considerable attention in recent years for its ability to utilize solar energy to produce hydrogen from water as well as the degradation of organic contaminants in wastewater systems. Upon illumination of a photocatalytic material with solar radiation, the photonic energy is absorbed by electrons in the photocatalyst, which then move up an energy level from the material's valence band (VB) to the conduction band (CB), leaving positively charged holes (h^+) in the valence band. These photo-excited electrons can then migrate to the catalyst surface and act as strong reducing agents, while the holes can act as strong oxidizing agents.[17] As a result, photocatalysts are capable of catalyzing redox reactions, with the reaction conditions tailorable to either produce hydrogen from water splitting reactions, oxidize and degrade organic contaminants in aqueous solutions, photocatalytically reduce CO_2 to form hydrocarbon chains, etc.

Titanium dioxide (TiO_2) is one of the most widely studied photocatalysts for hydrogen production and contaminant degradation due to its low cost, low toxicity and chemical stability.[18] However, the photoactivity of TiO_2 is limited largely due to the existence of a large optical band gap (3.2 eV, for photoactive TiO_2 anatase)[19]. A material band gap refers to the difference between the conduction band and valence band energies, with a larger band gap requiring higher photonic energies for photo-activation. As a result, TiO_2 cannot be activated by visible light irradiation, which has a photonic energy between 2 – 3 eV[20], and thus it requires the presence of higher energy UV irradiation for photocatalytic reactions. However, UV light only constitutes 3 – 5% of the total

solar energy incident on the surface of the Earth, with the vast majority of the solar spectrum being composed of visible light and lower energy infrared radiation.[19] This results in a very low solar energy conversion efficiency, as the visible spectrum of light remains unharnessed. Recently, the advent of a reduced form of TiO_2, black TiO_2, has shed light on a novel technique of surface modifying TiO_2 to reduce its band gap and increase the absorption of visible light. By inducing surface defects in the form of oxygen vacancies, the subsequent lattice disorders generate mid-gap states, effectively up-shifting the valence band edge of TiO_2, resulting in a narrowing of the optical band gap and enhancement of photocatalytic activity under visible light irradiation.[21]

Vanadium pentoxide (V_2O_5), another oxide-based semiconductor like TiO_2, has also been widely investigated for the degradation of organic pollutants in aqueous solutions. Owing to its low cost, photostability and narrower band gap (2.4 eV), V_2O_5 has the potential to surpass TiO_2 in terms of organic contaminant degradation, with the pristine form inherently capable of harnessing visible light directly. In addition, with a greater density of oxygen atoms in the lattice structure and higher oxidation state of the transition metal (V^{5+}) in V_2O_5 (compared to Ti^{4+} in TiO_2), surface modifications to induce oxygen vacancies and additional oxidation states of V^{4+} and V^{3+} can be expected to significantly enhance the photocatalytic performance of the material compared to pristine V_2O_5.

Substantial research work has been performed towards improving the performance of TiO_2-based photocatalysts in the visible light region. However, other semi-conductors with inherently narrower optical band gaps have recently attracted significant interest towards solar hydrogen production. Figure 3 below summarizes some commonly studied photocatalysts and their respective band gap energies.

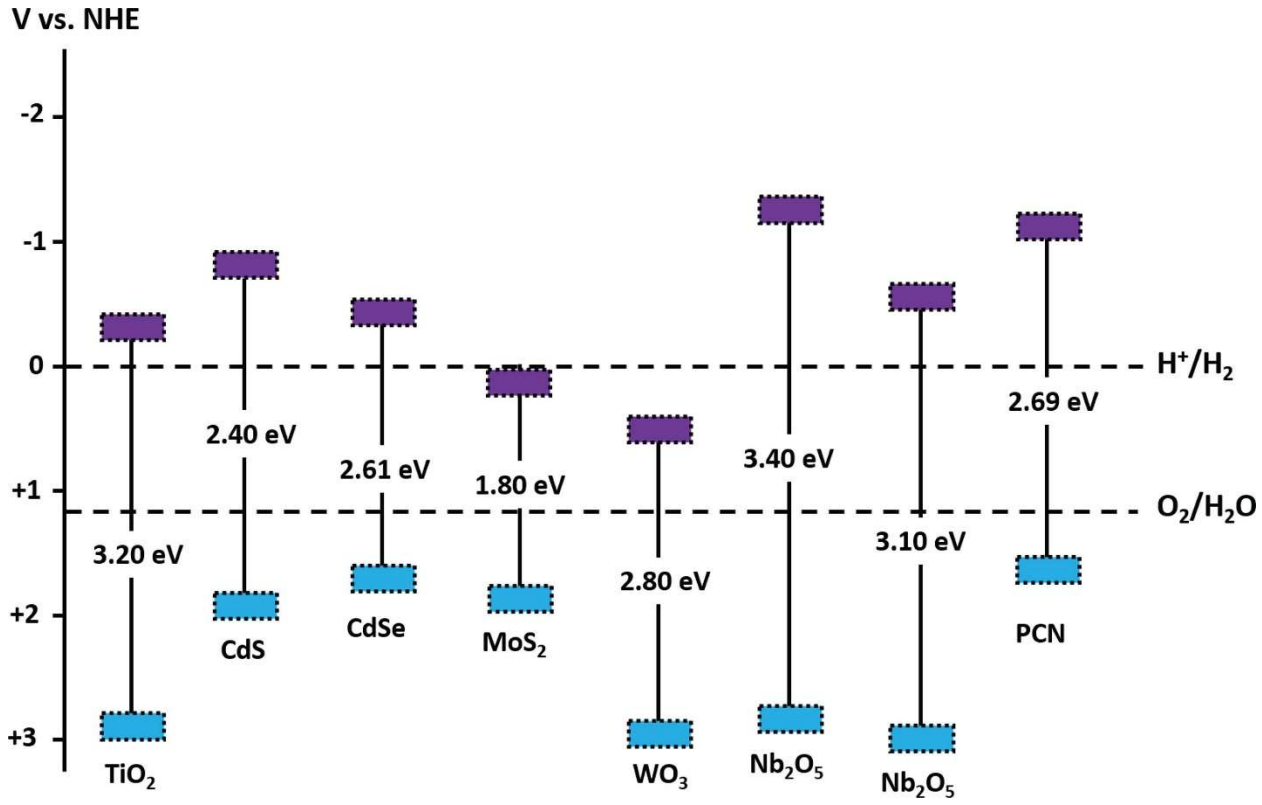

Figure 3: *Band edge positions and band gaps of various semiconductors, reprinted from Teixeira IF et al.*[22]

Cadmium sulfide (CdS) has been widely studied for photocatalytic hydrogen production from water, owing to its relatively narrower band gap (2.4 eV), rendering it capable of harnessing visible light for photocatalytic reactions. In addition, for H_2 production from water splitting, the conduction band edge of the catalyst must be more negative than the H^+/H_2 reduction potential, and the valence band edge must be more positive than the O_2/H_2O redox potential.[23] Referring to Figure 3 above, CdS fulfills this requirement with favorably positioned band edges, making it highly suitable for H_2 production from water splitting. However, as is generally the case with semiconductors possessing narrow band gaps, charge separation between the photo-excited electrons and produced holes is reduced, resulting in rapid electron-hole pair recombination, which

reduces the number of photo-excited electrons available for initiating redox reactions on the catalyst surface. In addition, CdS generally suffers from a rapid rate of photo-corrosion under solar irradiation, a phenomenon that results in a significant decrease in photocatalytic activity and catalyst lifetime.[24] Hence, it becomes imperative to develop techniques for photocatalyst design that allow for increased charge separation while maintaining as narrow a band gap as possible. The introduction of other semi-conductors as co-catalysts has proven to be an effective technique towards addressing some of the issues faced when using pure CdS as a photocatalyst. Creating a hetero-junction, or interface, between CdS and another suitable co-catalyst can suppress electron-hole pair recombination by allowing the photo-generated electrons and holes to migrate between the conduction and valence bands of the two semi-conductors. This leads to increasing charge separation and reducing the rate of electron-hole pair recombination.[25]

Additionally, the incorporation of a carbonaceous support, such as activated carbon, carbon nanotubes, graphene, etc., has been known to further enhance charge separation in photocatalytic materials. This is due to the migration of the photo-generated electrons along the length of the highly conductive carbon layer, which can effectively increase the charge separation between the electrons and holes, and thus enhance photocatalytic activity. Moreover, with CdS particles known to agglomerate rapidly in solution, the incorporation of a carbon support will improve particle dispersion, resulting in an increase in the total catalytic surface area available for H_2 evolution reactions.

This research work aims at developing photocatalytic materials targeting efficient organic contaminant degradation and H_2 production from water splitting under visible light irradiation. A facile reduction procedure was performed on V_2O_5 to induce surface oxygen vacancies and reduce the effective material band gap to enhance organic contaminant degradation under visible light

irradiation. This reduced form of the pristine V_2O_5 is evaluated for photocatalytic efficiency via the degradation of methylene blue, a model organic contaminant, under solar irradiation. In addition to the effect of the reduction process on the optical band gap, degradation kinetics is also evaluated. The material morphology will be characterized using SEM imaging and crystallinity and material phases will be determined via XRD analysis. In addition, catalyst surface area and pore distributions will be characterized by the Brunauer-Emmett-Teller (BET) technique, and the successful induction of oxygen vacancies will be determined by X-ray Photoelectron Spectroscopy (XPS).

For photocatalytic H_2 evolution from water splitting, CdS is coupled with a co-catalyst, MoS_2, and grown in-situ on multi-walled carbon nanotubes (CNTs) acting as the carbon support. The co-catalyst and CNT loading were optimized, and the effect on material crystallinity, optical band gap and rate of H_2 evolution from water were evaluated. Catalyst performance was quantified in terms of quantum efficiency, in addition to evaluating the material durability and recyclability for H_2 production.

Scope of Work

The scope of this work involves the development of materials capable of harnessing visible light for photocatalytic applications including the degradation of organic contaminants in aqueous systems and the photocatalytic water splitting. A reduced form of V_2O_5 was developed and tested for contaminant degradation under solar irradiation. In addition, CdS was coupled with MoS_2, a suitable co-catalyst, and combined with a carbonaceous support, with the aim of enhancing material photoactivity towards hydrogen evolution from water and addressing some operational challenges faced with the application of CdS for the same purpose.

The following specific objectives were pursued throughout the course of this work:

1. Design and synthesize reduced V_2O_5 (bV_2O_5) with active photocatalytic properties.
2. Design and synthesize a CdS – MoS_2 composite supported on multi-walled carbon nanotubes (CdS – MoS_2 / CNTs) for photocatalytic water splitting.
3. Evaluate performance of the bV_2O_5 photocatalyst for organic contaminant degradation in aqueous solution, using methylene blue as a model contaminant.
4. Evaluate performance of the CdS – MoS_2 / CNTs photocatalyst for water splitting reactions under solar irradiation in the presence of lactic acid as a sacrificial reagent.

CHAPTER II - LITERATURE REVIEW

Background

The rapid technological and industrial progress made by modern society can be directly attributed to the efficient utilization of our energy resources for societal benefit. The advent of the industrial revolution coincides with the birth of fossil fuel use for energy applications, kick-starting an exponential rate of industrial growth never seen before, and continuing ever since. As the Earth's population continues to increase and with every leap in technological progress we continue to push the levels of energy consumed. As shown in Figure 4 below, global energy demand has risen exponentially since the industrial revolution, increasing by over 7 times over the past century.[26]

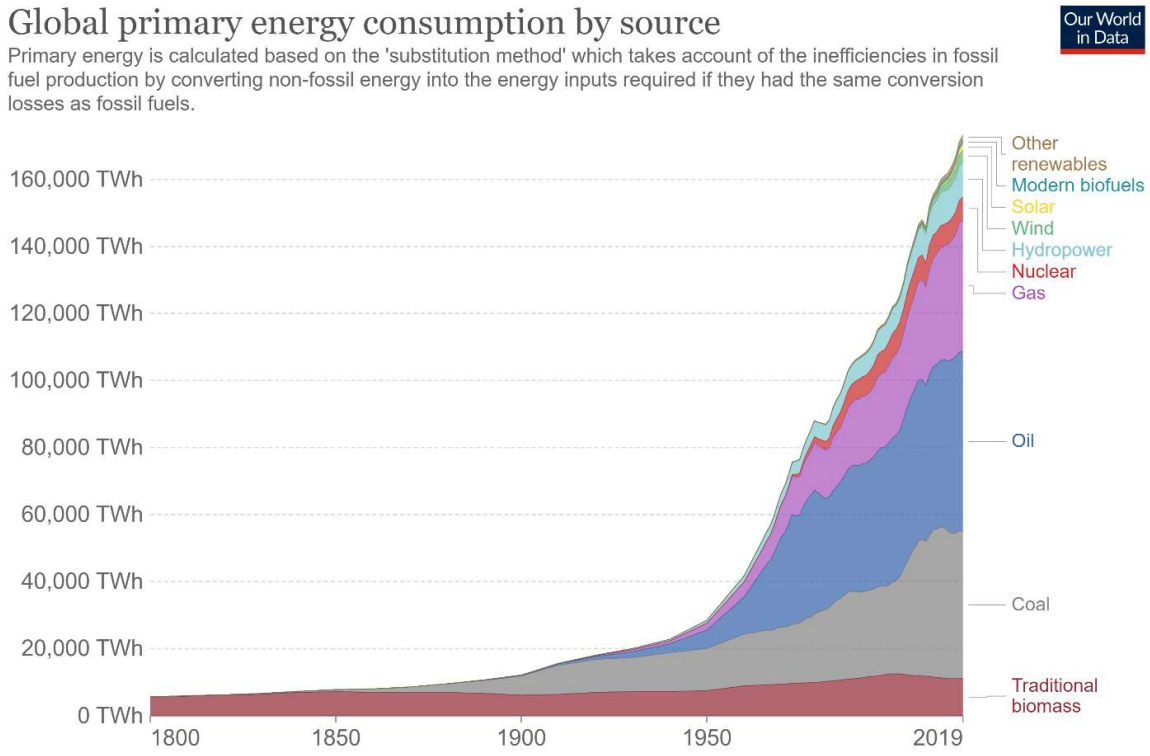

Figure 4: *Global primary energy consumption, reprinted from BP Statistical Review of World Energy, 2020.*[26]

Traditionally, global energy supply has been largely met using coal, oil, and natural gas. In 2019, these fossil fuels have accounted for nearly 80% of primary energy consumed, and while renewable and nuclear energy sources have recently started becoming more prominent, global reliance on fossil fuels for energy production remains absolute. However, the nature of fossil fuels inherently creates two significant challenges that can result in catastrophic developments should they remain unaddressed.

Optimistic literary assessments conclude that oil production will peak near 2100 and continue to decline after, while other sources claim that oil production has already peaked and natural gas production will soon follow a similar trend. However, severely detrimental social and economic effects are expected in the oil and gas decline phase, as rising fossil fuel prices may trigger food, water and security crises due to a shortage of fuel and electricity.[27]

Despite the concerns surrounding fossil fuel longevity, a more immediate threat arises from the nature of fossil fuel consumption. Fossil fuels are formed from organic sources and hence, their combustion generates CO_2, a major greenhouse gas, as a by-product. Climate change has rapidly become a globally discussed issue due to a rising number of direct tangible effects; melting glaciers, rising sea levels, severe weather conditions and hotter average annual global temperatures.[28] Mitigating these drastic effects has become a top global priority, with the adoption of the Paris Agreement in 2015 legally binding all signing nations to collectively limit global warming to 2°C (and preferably to 1.5°C) above pre-industrial levels. However, to achieve the desired goals, significant reductions in CO_2 emissions are necessary on a global scale. Studies show that the energy sector accounts for nearly 70% of total global greenhouse emissions produced annually, with fossil fuel combustion making the largest contribution to CO_2 from the energy sector, as shown in Figure 5 below, making it the area in need of greatest reform.[29]

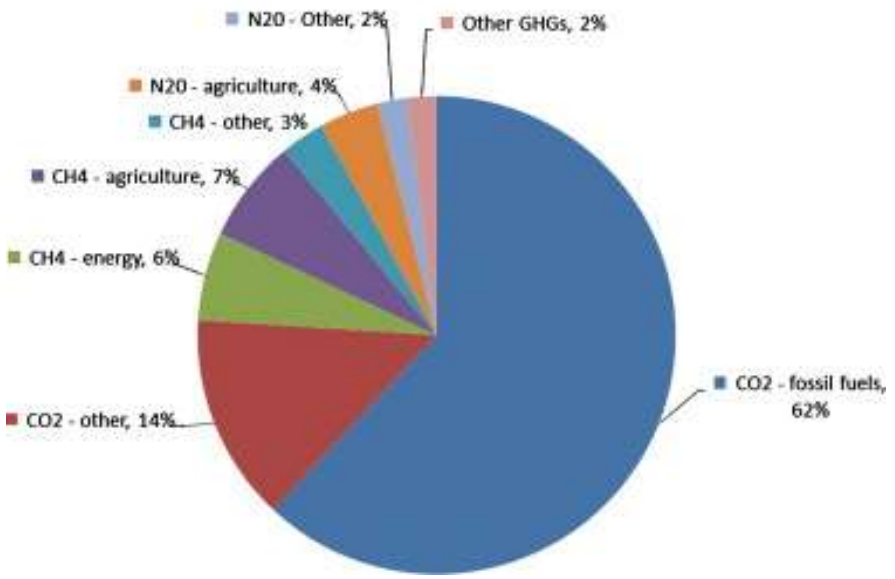

Figure 5: *Breakdown of total annual greenhouse emissions, reprinted from Höök M et al.*[29]

Developing alternative sources of energy to sustain the exponential rise in energy demand, therefore, becomes of vital importance to ensure that fossil fuel consumption is minimized to avert irreparable damage to the planet and ecosystem, avoiding catastrophic economic collapse and loss of human life. With fossil fuel reserves being continually depleted and there existing a definite, albeit unknown, cap on total reserves available, it becomes even more imperative to ensure alternative, renewable sources of energy are available to ensure humanity does not run out of all useable energy resources.

Hydrogen is widely regarded as the fuel of the future, with the use of hydrogen inherently providing solutions to several challenges faced during energy generation from fossil fuels. Hydrogen is a clean energy carrier, with the combustion of H_2 producing only energy and water and no harmful emissions. In addition, hydrogen has a much higher specific energy, on a weight

for weight basis, than any other source (Table 1 below), and when coupled with its extremely abundant nature, it becomes a near ideal candidate to meet global energy requirements.

Table 1: *Specific energies of hydrogen and other fossil fuels.*[30]

Fuel	Specific Energy (kWh/kg)
Hydrogen	33.3
Natural gas	13.9
Petrol	12.8
Diesel	12.6
Coal	8.2

However, the dream of switching to a hydrogen-powered economy is far from being realized, owing to several key challenges that must be overcome before it can be used on a global scale. The greatest of these challenges is the development of efficient and cost effective techniques for hydrogen production, with the current methods still unfeasible to be used on a commercial scale.[30]

Conventional technologies for hydrogen production

Despite the benefits of using hydrogen as a fuel, nearly all the current global demand for hydrogen is met via the use of fossil fuels in processes involving significant greenhouse emissions. Natural gas is the most widely used precursor for hydrogen generation, with the three widely used conventional technologies outlined below.

Reforming of hydrocarbons

Hydrocarbon reforming may involve several types of processes, the most common of which is the steam reforming of natural gas, primarily methane. In conventional steam reforming of methane (SRM), the hydrocarbon and steam are catalytically converted to hydrogen and other carbon oxides, in a process as outlined in the schematic below.

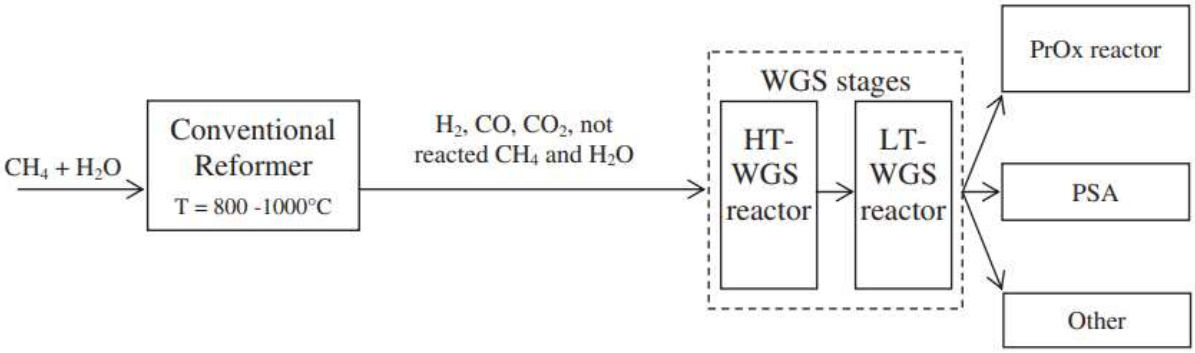

Figure 6: *Conventional reforming of methane, reprinted from Iulianelli A et al.*[31]

Methane and steam are fed into a conventional reformer operating at high temperatures (800 – 1000°C) and pressures (14 – 20 bar), where they endothermically react over nickel based catalysts to form a hydrogen-carbon monoxide (H_2/CO) mixture, as shown in the equation below, with CO concentration of 5 vol% or greater.[31]

$$CH_4 + H_2O \rightarrow CO + 3H_2$$

The product stream is then fed into water-gas shift reactors that are used to increase the hydrogen content in the stream by reacting the CO with steam to produce additional H_2 in the reaction shown below.

$$CO + H_2O \leftrightarrow CO_2 + H_2$$

Subsequently, additional purification steps in the form of pressure-swing adsorption (PSA), preferential oxidation reactors (PrOx) or others such as cryogenic distillation, methanation or physical scrubbing are applied in order to obtain high purity hydrogen.[31] The steam reforming of natural gas requires raw material purification to remove any sulfur impurities which can deactivate the catalyst. In addition, the highly endothermic nature of the reaction requires significant amounts of energy input, increasing production cost. An alternative method to conventional steam reforming is the partial oxidation of hydrocarbons, a technique exhibiting several advantages such as faster response times, compactness and less sensitivity for fuel variance than conventional steam reforming, in addition to involving an exothermic reaction.

In the partial oxidation, the raw materials used are typically gasified heavier hydrocarbons, while methane can also be used. The hydrocarbon raw material is heated in the presence of a stoichiometric amount of oxygen (Figure 7 below), with the following reactions taking place in the case of methane being used.[32]

$$CH_4 + \frac{1}{2}O_2 \rightarrow CO + 2H_2$$

$$CH_4 + 2O_2 \rightarrow CO_2 + 2H_2$$

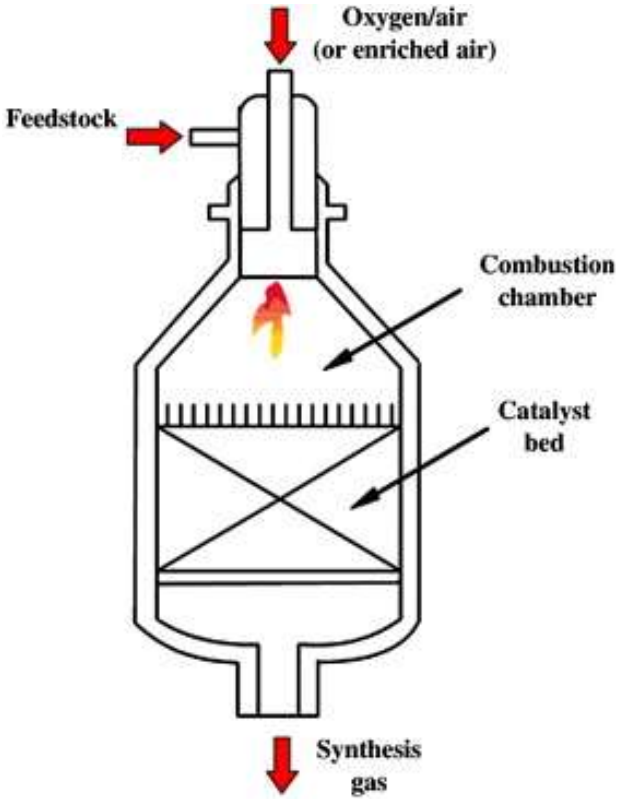

Figure 7: *Partial oxidation of methane, reprinted from Rowshanzamir S et al.*[33]

The reaction is generally carried out in the temperature range of 1300 – 1500°C and pressures in the 30 – 80 bar range without a catalyst, with milder operating conditions used in the presence of a catalyst.

The third process involving hydrocarbon reforming is autothermal reforming (ATR), a combination of conventional steam reforming and partial oxidation, with the partial oxidation reaction being carried out in the presence of steam as well. In addition to methane reacting with oxygen to form CO_2 and water, it also reacts with steam to produce carbon monoxide, combining the reactions of conventional steam reforming and partial oxidation to increase the overall yield of hydrogen, while also allowing the heat generated by the exothermic partial oxidation reaction to partially offset the external heating requirement for conventional steam reforming.[34]

The partial oxidation technique, while readily used with natural gas, can also be used with liquid hydrocarbons such as oil, as well as solid carbonaceous material like coal. However, liquid hydrocarbons and coal must go through a gasification process, which unlike complete combustion, only involves partial burning of the hydrocarbon to induce enough heat for CO formation (incomplete combustion).[35] The formed CO can then react with input steam to generate hydrogen and CO_2.

While still accounting for nearly 100% of the hydrogen demand today, these techniques for hydrogen generation are not sustainable for two main reasons. With the increasing global population and demand for fuel sources, hydrogen as a fuel can only be feasible if its production is free of fossil fuel consumption. Switching to hydrogen powered systems will require significantly larger quantities of hydrogen to be produced, with conventional production techniques suffering from substantial greenhouse emissions, rendering them unscalable for commercial use; it is estimated that the steam reforming of natural gas, the technique accounting for nearly 50% of all current hydrogen demand, involves the production of nearly 13.7 kg of CO_2 for every 1 kg of hydrogen produced.[36] Secondly, the use of these conventional fossil fuel based techniques still involves the challenge of fossil fuel depletion; if the development of hydrogen as an alternate fuel is inherently linked to the consumption of traditional fuels, the cost of hydrogen generation will inadvertently increase as fossil fuel reserves are expended and the drop in hydrogen production may mirror the eventual decline in fossil fuel extraction. Therefore, it becomes essential to develop technologies for hydrogen production independent of any fossil fuel use.

Wastewater treatment technologies

Municipal and industrial wastewaters contain a wide variety of contaminants, from fertilizers, pesticides, pathogens and human waste from agricultural activities to pharmaceuticals, fine chemicals, organic contaminants, heavy metals, suspended solids, toxic substances and more. Before these waste streams can be discarded into environmental bodies, adequate treatment processes must be employed to ensure sufficient removal of harmful contaminants to avoid damage to aquatic life, human health and the environment. In addition, with multiple steps of wastewater treatment, it is possible to generate clean water for direct reuse in agricultural, industrial and domestic applications.

Primary, secondary and tertiary wastewater treatment

Conventional wastewater treatment systems use integrated primary, secondary and tertiary techniques to remove a variety of contaminants. Primary treatment processes involve screening and skimming to remove large floating and suspended solids, before the wastewater is fed into sedimentation tanks. The effluent is subsequently subjected to physical sedimentation by allowing the water to remain undisturbed for a certain amount of time (2 – 6 hours), before the remaining finer contaminants are removed via chemical sedimentation, with the addition of coagulants inducing the finer solids to clump together and settle to the bottom of the tank.[37] Primary treatment removes between 60 – 80% of all suspended solids. Secondary treatment systems involve the use of microorganisms to remove the soluble organic impurities present in the wastewater. Suitable biological species such as bacteria are used to feed on the organic contaminants in aerobic or anaerobic systems.[37] The organic impurities are converted into CO_2, water and other end products.

Tertiary, or advanced, treatment systems are used to further purify the water by removing biodegradable organic matter, heavy metals and pathogens. Chlorination of the effluent is

generally used for disinfection. Chlorine gas reacts with the water to form hypo-chlorous acid (HOCl), which acts as a germicide and eliminates bacteria, viruses and other harmful pathogenic microorganisms. Ultraviolet (UV) light irradiation may also be used for disinfection purposes. Following secondary treatment, the wastewater is irradiated by UV lamps which sterilize the water by reacting with and genetically damaging any microorganisms present, rendering them incapable of causing any adverse effects to humans or aquatic life. Moreover, ozonation is also a common technique used for tertiary treatment, as ozone is highly reactive, destroying most microorganisms it encounters, and can be used much more safely for disinfection as compared to chlorine.

Adsorption using activated carbon and membrane systems targeting removal of specific contaminants is also conventionally employed. Activated carbon, in powdered or granular form, can be used as an adsorbent to remove specific contaminants from aqueous systems, due to its high specific surface area because of its high porosity, and good affinity for various organic species and metal ions. Contaminant adsorption is primarily governed by contaminant-carbon surface interactions via Van der Waals forces or electrostatic interactions, with wastewater type, contact time, solution pH and organic contaminant concentration crucially affecting the adsorption process.[38]

Membrane desalination via microfiltration (MF), ultrafiltration (UF), nanofiltration (NF) and reverse osmosis are also employed post-secondary treatment to achieve discharge requirements and requirements for water reuse. MF and UF membranes have pore sizes in the range 0.05 – 10 μm and 0.001 – 0.05 μm respectively[39], with both types of membranes operated at low transmembrane pressures. Due to their large pore sizes, MF membranes are not suitable for the removal of most natural organic matter (NOM) barring larger molecules such as polysaccharides, and are more generally used for color, turbidity and pathogen removal.[40] UF membranes operate

under the same principles of size exclusion and particle capture like MF membranes, however, due to their smaller pore sizes, they are generally used for the removal of smaller contaminant species than MF membranes, including leachate molecules, inorganic salts and other micro molecular organic particles.[41]

NF membranes are usually characterized by pore sizes in the range of 0.5 – 1 nm, typically having a molecular weight cut off (MWCO) of between 1000 – 200 Da (amu).[42] Nanofiltration requires the use of higher operating pressures (5 – 20 bar) when compared to MF and UF membranes, with the separation efficiency being governed by the sieving effect or by the solution and diffusion properties of the solute through the pores of the membrane, in addition to the effects of the electrical field in the case of charged contaminants. NF membranes characteristically achieve very high rejections of multivalent ions (>99%) and organic species with a molecular weight larger than the MWCO of the membrane (>90%), with moderate rejection of monovalent ionic species (~70%).[42] This technique is used to remove most organic matter, pathogens and a wide range of salts, with the near complete removal of divalent ions (species responsible for hard water) resulting in the partial softening of hard water as well.[42]

The fourth membrane desalination technique conventionally employed is reverse osmosis (RO), which utilizes the finest membranes amongst all four membrane filtration techniques, with pore sizes in the range of 0.1 – 0.5 nm.[43] Unlike MF, UF and NF filtration techniques that rely on the sieving effect to purify water, RO membranes are characterized by their effective semipermeable nature, with the RO process utilizing the difference in chemical potential of the solutions on both sides of the membrane for purification.

Membrane fouling is a significant challenge facing MF, UF, NF and RO filtration technologies. Fouling involves a reduction in permeate flux through the membrane overtime during the filtration

process, with an increase in pressure needed to maintain constant flux. Membrane fouling is caused by complex interactions between the contaminants present in solution and membrane surface; contaminant attachment and accumulation can cause concentration polarization (higher solute concentration as compared to the bulk solution) near the membrane surface which can decrease the driving force across the membrane, and smaller species that enter the membrane can cause pore clogging. The phenomenon can be reversible or irreversible, with reversible effects such as cake formation and concentration polarization near the membrane surface being removed via sufficient backwashing or surface washing, restoring the permeate flux through the membrane. However, irreversible fouling such as pore plugging and chemisorption result in a permanent loss in transmembrane flux, requiring the membranes to be extensively chemically cleaned or replaced.[44]

Studies have shown that the initiation of membrane fouling typically occurs due to the presence of low molecular weight natural organic matter (NOM) and the bulk of the fouling is effected due to higher MW colloidal substances, namely humic acids, fulvic acids, transphilic acids, amino acids and carbohydrates, amongst others.[44] Particularly for MF and UF membranes that have large enough pore sizes to allow these substances to pass through, NOM adsorbs on the membrane surface and inside the pores, forming a gel layer that reduces the channels available for solvent flow, causing a subsequent reduction in permeate flux.[45] Such fouling can significantly increase the operational costs, particularly for high pressure systems such as NF and RO processes, as a greater applied pressure will be required to maintain permeate flux as the extent of membrane fouling increases. In addition, chemical treatment to reverse the effect of pore plugging and chemisorption adds to the maintenance cost of the system and added downtime, requiring membrane replacement or effecting loss in productivity and production capacity.[46]

Typically, suitable pretreatment processes to reduce the fouling contaminants prior to membrane desalination must be employed to increase membrane lifetime. Wastewater can be run through MF/UF and NF filtration before being fed to the RO process, however, such sequential pretreatment systems still involve membrane fouling upstream of the RO process.[47] Increasing the lifetime of the RO membrane comes at the cost of fouling in the MF/UF/NF membranes, with them still requiring appropriate treatment to recover the permeate flux. In addition to the added cost of maintenance, operational costs are also increased due to the energy demand for all additional pretreatment systems used. With NF and RO desalination techniques capable of treating wastewater to generate potable water for direct reuse, it becomes imperative to develop alternative, environmentally benign pretreatment methods to combat the effects of membrane fouling and prolong membrane lifetime, while minimizing the process energy demand.

Heterogeneous photocatalysis

Heterogeneous photocatalysis has been widely studied as a potential substitute for wastewater treatment and hydrogen production technologies, due to its inherent environmentally benign nature and involved utilization of renewable sources of energy as opposed to fossil fuels. Photocatalysis involves the use of a catalytic material that is activated in the presence of solar energy, via the mechanism shown in Figure 8 below.

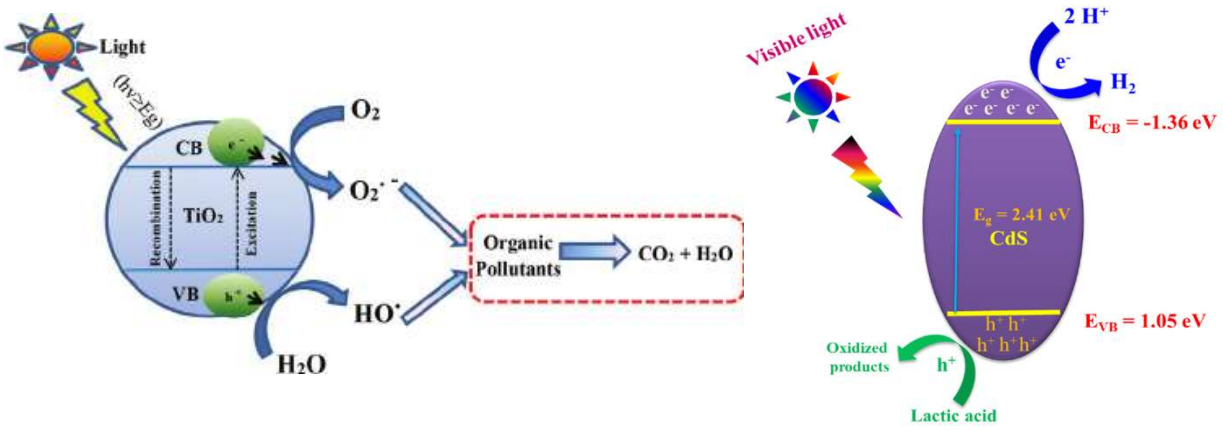

Figure 8*: a) Organic contaminant degradation, reprinted from Samsudin EM et al.*[48] *b) Photocatalytic hydrogen production, reprinted from Chava RK et al.*[49]

Figure 8a depicts the mechanism of photocatalytic organic contaminant degradation using titanium dioxide, TiO_2, a commonly used photocatalyst. When irradiated with solar energy, the photoexcited electrons react with O_2 molecules, provided the conduction band is suitably positioned, to form superoxide radicals, while the holes (h^+) react with water molecules to form hydroxyl radicals. The superoxide and hydroxyl radicals are strong oxidizing agents and react with organic pollutants, oxidizing them into CO_2 and water as degradation products.[48] Figure 8b depicts the mechanism of photocatalytic water splitting to produce H_2, using cadmium sulfide, CdS, and lactic acid as a sacrificial reagent. A sacrificial reagent is a chemical species that can be readily oxidized by the h^+ on the surface of the catalyst. The photoexcited electrons react with protons from water to produce hydrogen, while the reaction of the sacrificial reagent with the h^+ completes the other half of the photocatalytic cycle, consuming the h^+ and replenishing electrons to be subsequently photoexcited.[50]

When irradiated with sunlight, the electrons in the semiconducting photocatalyst absorb the photonic energy and move from the valence energy band to the conduction energy band, leaving holes (h^+) in the valence band, provided the photonic energy provided is equal to or greater than the material band gap (energy difference between the conduction band and valence band). The generated photo-excited electron (e^-) – hole (h^+) pairs can then catalyze redox reactions on the catalyst surface, with the photo-excited electrons and holes acting as reducing and oxidizing agents respectively.[51] The reaction conditions can be tailored to utilize photocatalysis for contaminant degradation in wastewater or water splitting to produce hydrogen by the choice of substrate compounds used in the reaction system.

Titanium dioxide (TiO_2) is the most widely studied material for photocatalytic applications, owing to its strong oxidizing capabilities, hydrophilicity, stability, nontoxicity and cost effectiveness.[52] It has been studied for a variety of environmental and energy applications, particularly water treatment and hydrogen production. However, TiO_2 has a band gap of 3.2 eV, corresponding to photonic energy in the UV light region. Solar energy radiant on the surface of the Earth is composed of approximately 5% UV light only, with visible light and lower energy infrared radiation making up the majority of the incident solar spectrum.[53] Ensuring effective utilization and maximum conversion of solar energy, therefore, requires the development of materials capable of harnessing visible light for efficient photocatalytic applications.

In 2011, Chen at al. developed hydrogenated TiO_2 crystals, also known since as black TiO_2. By exposing pristine TiO_2 nanocrystals to pressurized hydrogen at 20 bar and 200°C for 5 days, surface and lattice defects in the form of oxygen vacancies and H-doping resulted in a black TiO_2 material with increased light absorption (Figure 9a) in the visible light region and considerably enhanced photocatalytic activity for contaminant degradation and hydrogen production. The induced lattice disorders introduce several mid gap states with a distribution of energy levels near the conduction and valence bands of TiO_2.

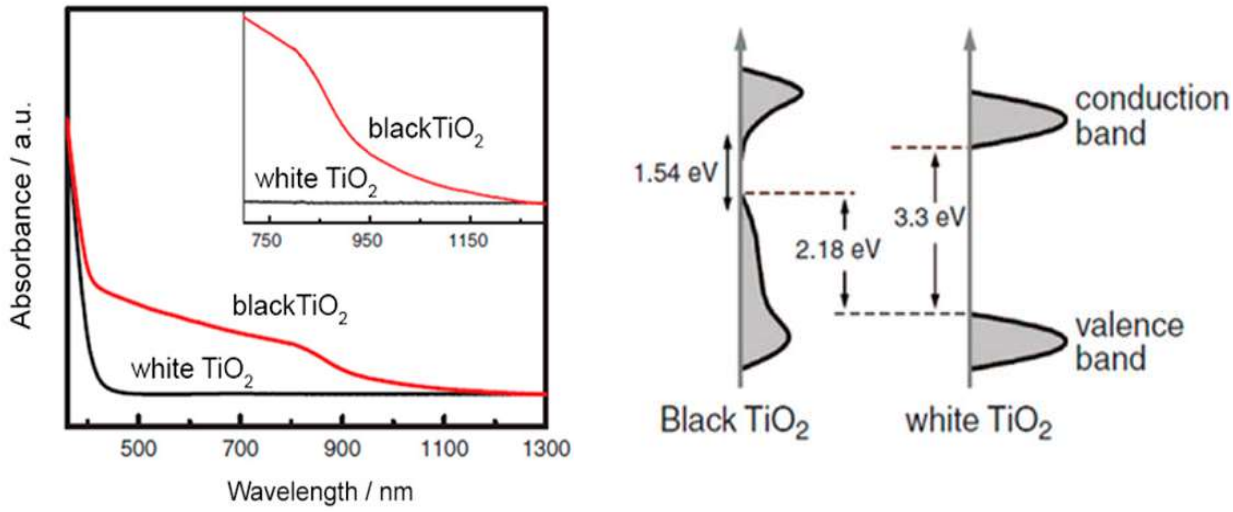

Figure 9: *a) Absorbance spectra of pristine and black TiO_2.[21] b) Band tailing in black TiO_2, reprinted from Chen X et al.[21]*

Instead of forming discrete energy states near the conduction and valence band edges, the distribution of mid gap states forms a continuum, overlapping with the original band edges as shown in Figure 14b[54], resulting in an effective narrowing of the optical band gap, from 3.3 eV to 1.54 eV.[21,54] In addition, the additional energy states (due to presence of Ti^{3+} as a result of Ti^{4+} reduction) act as trapping sites for the photoexcited electrons and holes, reducing the rate of electron-hole pair recombination and improving catalytic efficiency.[54] Black TiO_2 was found to

exhibit a hydrogen production rate of nearly 10 mmol g^{-1} h^{-1} under solar irradiation, with its platinum-doped pristine counterpart not producing any hydrogen under identical reaction conditions.[54] Since then, several other techniques of reducing TiO_2 to form black TiO_2 have been explored, with the physicochemical and solution based reduction with $NaBH_4$ under elevated operating conditions one of the most widely used techniques.

Studies on the bulk and surface oxygen vacancies (O_v) formed on black TiO_2 show that bulk O_v are deterrent for photocatalytic performance as they can act as electron-hole recombination centers, decreasing material performance. However, surface O_v are beneficial for contaminant degradation as they serve as O_2 binding sites, promoting the reaction between O_2 molecules and the photoexcited electrons to form superoxide radicals, a strong oxidizing agent.[55] While the effects of hydrogenation/reduction on TiO_2 have been widely studied, the concept can be theoretically extended to other similar oxide based semiconductors such as V_2O_5.

Vanadium pentoxide (V_2O_5) as a photocatalyst

V_2O_5 is a promising metal oxide for photocatalytic applications due to its narrower band gap when compared to TiO_2 and several other overlapping advantages such as non-toxicity, low cost, chemical and photostability, in addition to high lattice oxygen density and higher oxidation state of the transition metal involved (V^{5+} compared to Ti^{4+} in TiO_2). However, the relatively fast recombination rate coupled with a deep conduction band edge associated with V_2O_5 make several reduction reactions unfeasible and hinder the applications of V_2O_5 for photocatalytic processes. With the presence of a transition element with a higher oxidation state, in addition to higher density of lattice oxygen atoms, reduced V_2O_5 has the potential to surpass TiO_2 in terms of photocatalytic performance. The inherent material potential to incorporate a higher density of O_v and additional mid gap states due to the higher oxidation state of the transition metal than in TiO_2, greater band

gap narrowing and stronger suppression of electron-hole pair recombination may result in a vastly superior photocatalyst.

Thermodynamic limitations for hydrogen evolution from water require appropriately positioned conduction and valence band edges, with the conduction band edge required to be more negative than the H^+/H_2 reduction potential (-0.41 V) and the valence band edge required to be more positive then the O_2/H_2O redox potential (0.82 V).[23] V_2O_5 has a conduction band edge more positive than the H^+/H_2 reduction potential (0.3 V), rendering it thermodynamically incapable of reducing H^+ ions to form H_2.[56] Figure 10 below summarizes the band edges of several photocatalysts, highlighting several suitable candidates for hydrogen evolution from water.

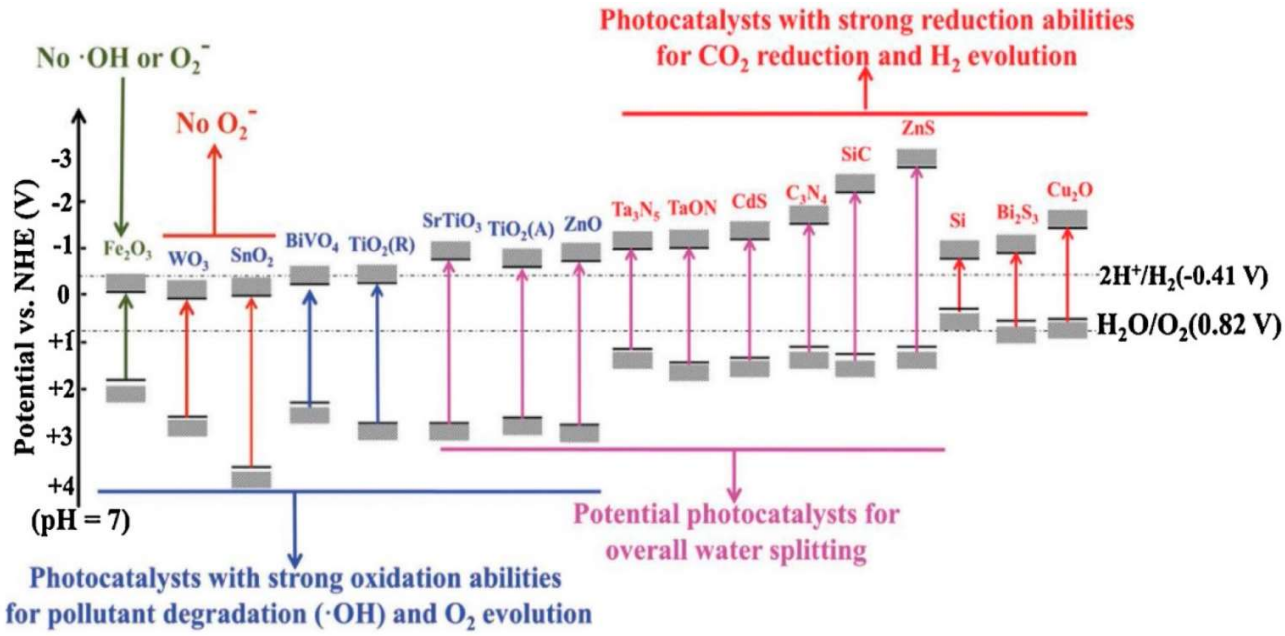

Figure 10: *Extended outline of known photocatalysts for various applications, reprinted from San Martín S.*[57]

While several photocatalysts such as $SrTiO_3$, TiO_2 and ZnO have appropriately placed band edges for photocatalytic water splitting, their large band gaps make them unsuitable for visible light

utilization. CdS is ideally suited for hydrogen evolution due to its narrower band gap (2.4 eV) in addition to advantageous band edge positioning.[58]

Cadmium sulfide (CdS) for photocatalytic hydrogen production

CdS exists in two different crystal structures; hexagonal and cubic, as shown in Figure 11 below. Both crystal structures are composed of CdS_4 tetrahedrons, with the cubic phase (ABCABC) having the tetrahedrons aligned along the (111) plane and the hexagonal phase (ABAB) having the tetrahedrons aligned along the (001) plane.[50,59]

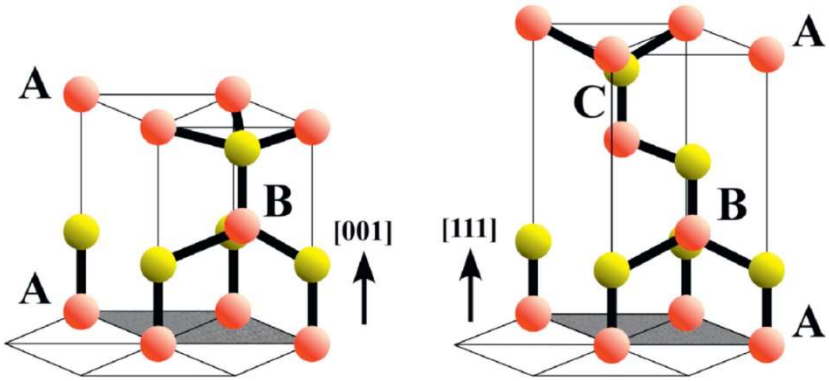

Figure 11: *a) Hexagonal CdS.[59] b) Cubic CdS, reprinted from Ghosh A et al.[59]*

Both crystal phases involve different electron transmission paths and directions, with the cubic and hexagonal phases displaying distinct photocatalytic activities. The hexagonal phase is more stable and crystalline than the cubic phase, with a subsequently superior photocatalytic activity.[60] Both phases also exhibit different band gaps (~2.6 eV for hexagonal and ~2.4 eV for cubic)[61], with the slightly larger band gap for the hexagonal phase probably resulting in a decrease in the rate of electron – hole pair recombination and, therefore, increasing catalytic efficiency. CdS prepared with both phases present has also been shown to outperform its single phase structural

counterparts, with the induced phase junctions acting to increase charge separation while narrowing the optical band gap.[62]

It has been generally found that cubic CdS is preferentially formed at low synthesis temperatures, and can be converted to the hexagonal phase by locally inducing stacking faults via sufficient grinding, heat treating the cubic CdS at elevated temperatures, or using higher temperatures and select cadmium and sulfur sources to preferentially form the hexagonal phase instead of the cubic.[63] It has been reported that the use of $CdCl_2$ as a cadmium precursor results in the formation of cubic CdS, while using $Cd(NO_s)_2$ (cadmium nitrate) results in the formation of hexagonal CdS.[64] XRD analysis can be used to identify the phase(s) present in CdS, with both crystalline phases exhibiting distinct XRD patterns as shown in Figure 12a below.

Haque et al. studied the effects of grinding and calcining the synthesized CdS, with the XRD analysis conducted along subsequent synthesis steps identifying the change in crystal phase, as shown in Figure 12b below.

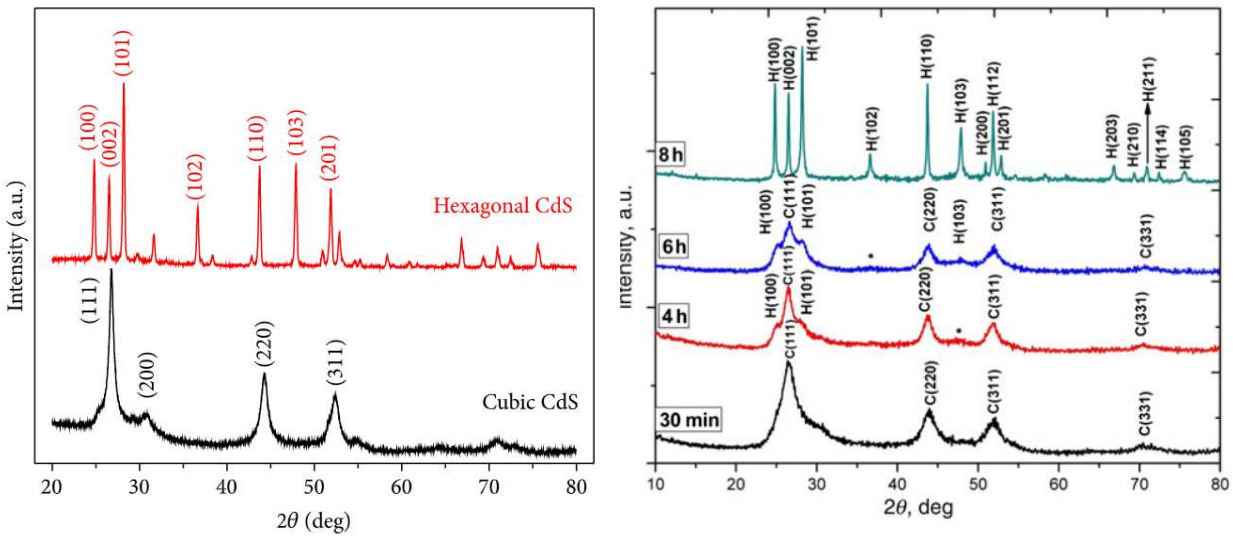

Figure 12: *a) XRD spectra of hexagonal and cubic CdS, reprinted from Yuan SQ et al.[65] b) XRD of various samples prepared by Haque et al, reprinted from Haque SE et al.[63]*

Following the room temperature synthesis of CdS from $CdCl_2$ and Na_2S, separate samples of the CdS product were subjected to grinding for various time periods (30 min, 4 h, 6 h, 8 h) before the ground samples were annealed at 200°C for 6 hours. XRD analysis of the samples, depicted above, show that the sample ground for 30 min and annealed was cubic CdS, with the peaks at 26.47°, 43.91°, 52.01° and 70.37° corresponding to cubic CdS present only (Figure 12b).[63,65] The sample ground for 8 h prior to annealing resulted in a purely hexagonal crystal structure, with sharp peaks at 24.83°, 28.21°, 36.65°, 47.88°, 50.93°, 52.85°, 54.64°, 66.84°, 69.33°, 72.45° and 75.55°, in addition to the very sharp peaks at 26.47°, 43.91°, 52.01° and 70.37°, characteristic of pure hexagonal CdS (Figure 12b).[63,65] Intermediate samples depict a mixture of hexagonal and cubic phases present in the same material, with a greater proportion of the hexagonal phase at higher grinding times.[63]

Although hexagonal CdS is more stable and exhibits greater photocatalytic activity than cubic CdS, it still requires significant improvements before it can be utilized on a commercial scale for photocatalytic applications. This is due to the relatively fast rates of charge recombination and induced photo-corrosion and chemical instability during application.[62] Several techniques to improve the stability and performance of CdS have been proposed and studied, including noble metal doping, coupling with other semiconductors, loading with a suitable cocatalyst and tuning the material structure and morphology.[58] The use of suitable cocatalysts as a technique to counter electron – hole recombination in particular has proven to be an effective method to improve CdS performance, with several materials such as TiO_2, ZnS, SnO_2, $NiSe_2$ and MoS_2, amongst others studied widely in literature.

Molybdenum disulfide (MoS_2) as a cocatalyst

Molybdenum disulfide (MoS_2) has recently attracted significant attention as a cocatalyst for hydrogen evolution reactions (HER) due to its tunable optical properties, unique layered structure, excellent physiochemical and electrical properties, and edge-controlled catalytic activity.[66,67] MoS_2 is classified as a layered transition-metal dichalcogenide, with weak Van der Waals forces layering the lamellar S – Mo – S units together to form 2-D layered MoS_2.[66] Typically, MoS_2 exists as three separate phases, 2H (hexagonal symmetry with dual-layered repeat unit), 3R (rhombohedral symmetry with three-layered repeat unit) and 1T (tetragonal symmetry with single-layer repeat unit), as shown in Figure 13.

The 2H phase is the most thermodynamically stable and most commonly found in bulk MoS_2.[68] While synthetically prepared MoS_2 is predominantly in the 3R phase, it readily rearranges to the 2H phase upon the application of heat. 3R and 2H MoS_2 phases exhibit semiconductor properties due to the presence of vacant d_{XY} and $d_{X^2-Y^2}$ orbitals, while the 1T phase exhibits a metallic nature.[69] The 1T crystalline phase is formed by the disorientation of one of the sulfur layers in MoS_2, and due to its metallic properties and a greater number of exposed active sites, it has the highest electrical conductivity of all the three possible phases.[69]

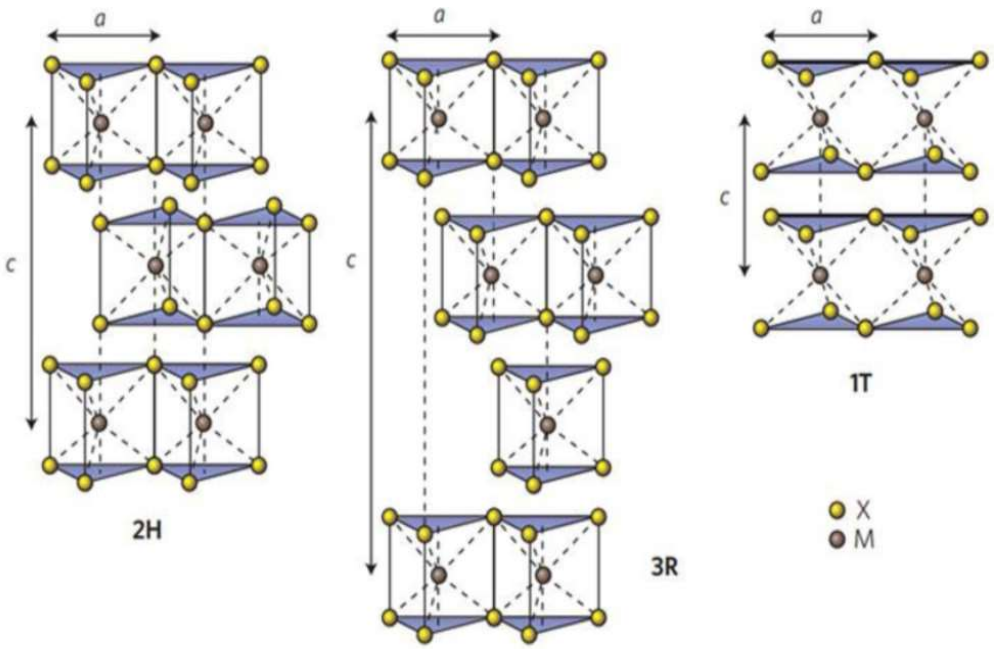

Figure 13: *Different phases of MoS_2, reprinted from Liang Z et al.*[66]

MoS_2 synthesis and exfoliation

Bulk MoS_2 can be synthesized by simple hydrothermal methods using a suitable molybdenum precursor (typically ammonium/sodium molybdate) and sulfur source (usually thiourea, thioacetamide, etc.). Obtaining controlled layered MoS_2 is then typically achieved via physical or chemical exfoliation of bulk MoS_2, with the exfoliation technique employed directing the monolayer phase obtained. The exfoliation techniques can be categorized as follows:

- Physical exfoliation[70] – Scotch tape-based micromechanical exfoliation to obtain single layer MoS_2 (2H phase).[71]
- Chemical assisted exfoliation
    - Liquid phase exfoliation (LPE) – Involves the extended sonication of bulk MoS_2 in a suitable solvent such as *N*-methyl pyrrolidone (NMP), Isopropyl alcohol or

ethanol, followed by complete removal of the solvent via centrifugation and evaporation/boiling off of the solvent, forming 2H crystalline MoS_2.[72]

- Chemical lithium intercalation exfoliation – The use of solvated lithium ions used to penetrate the bulk MoS_2 crystal lattice (usually in dimethyl sulfoxide solvent). The intercalated Li^+ ions cause the increase in interlayer spacing and expansion of the MoS_2 crystal structure, exfoliating the material and forming mono- and few-layer thick MoS_2 (1T and 2H phases).[71]

- Chemical vapor deposition (CVD) to form 2H crystalline MoS_2.[71]

Studies have shown that the optoelectronic properties differ from monolayer MoS_2 to bulk MoS_2. Bulk MoS_2 has an indirect band gap of 1.2 eV, which then switches to a direct band gap of 1.9 eV for monolayer MoS_2, a phenomenon that may be attributed to quantum size effects.[66] The shift in band gap is attributed to an upshift of the conduction band edge potential, from -0.16 V to -0.53 V for the bulk and monolayer respectively.[66] As shown in Figure 14 below, the H^+/H_2 reduction potential, referenced to the standard hydrogen electrode, is -0.41 V, making monolayer (and few/multilayer) MoS_2, unlike bulk MoS_2, thermodynamically capable of reducing H^+ ions to produce hydrogen.

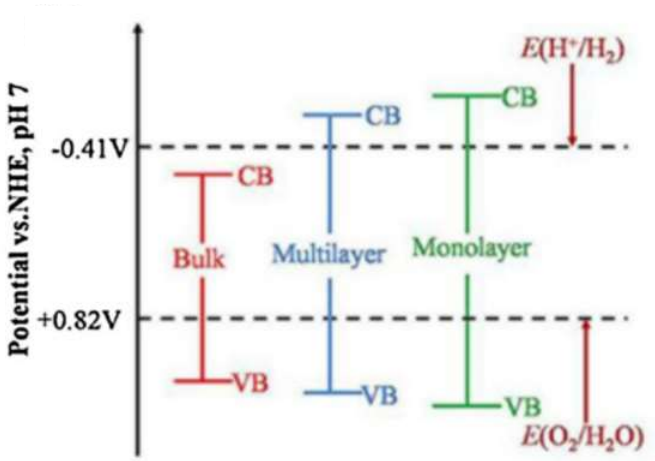

Figure 14: *Band edges and band gaps of MoS_2 with varying thickness, reprinted from Liang Z et al.*[66]

The heterojunction between CdS and MoS_2 is particularly feasible due to the formation of a p-n junction. Based on reported Mott-Schottky analyses, CdS is characterized as an n-type semiconductor, indicating that free electrons are involved as major charge carriers.[73] However, MoS_2 is characterized as a p-type semiconductor, indicating that positively charged holes are involved as major charge carriers.[73] Coupling CdS and MoS_2 results in the formation of an internal electrostatic field at the junction interface, effecting greater charge separation compared to other types of heterojunctions and enhanced photocatalytic activity, as outlined in Figure 15 below.

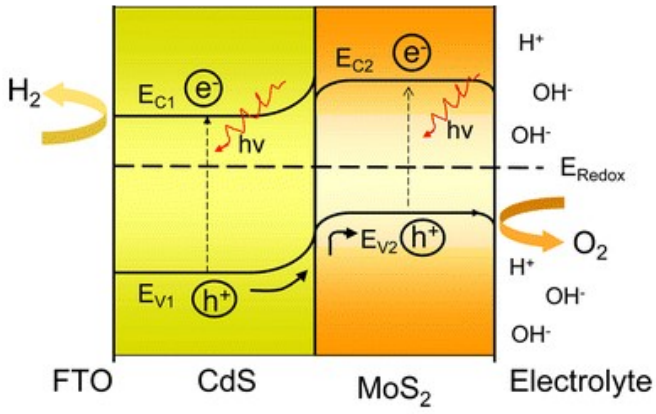

Figure 15: *p-n heterojunction between CdS and MoS_2 reprinted from Liu Y et al.*[73]

Photoexcited electrons from the conduction band of MoS_2 can migrate to the conduction band of CdS where hydrogen production and other reduction reactions can take place, with the positively charged holes moving in the opposite direction, from the valence band of CdS to MoS_2, where oxidation reactions can be catalyzed.[23]

Most reported literature has focused on preparing CdS/MoS_2 nanocomposites in sequential, multistep synthesis methods, involving separate synthesis of bulk MoS_2 followed by exfoliation to obtain few-layer MoS_2 sheets, with eventual deposition on synthesized 0D/1D CdS particles. Alternatively, the direct deposition of MoS_2 on CdS particles in solution via hydrothermal methods has also been extensively studied, with Table 2 below outlining several reported results for CdS/MoS_2 composites that have been used for photocatalytic hydrogen production. However, there has been limited study in the one-pot hydrothermal synthesis of CdS/MoS_2 nanocomposites. Preparation of bulk MoS_2 and subsequent physical/chemical exfoliation techniques are time consuming and usually involve the use of toxic chemical species. Moreover, with CdS and MoS_2 sharing a similar hexagonal crystal structure, the introduction of MoS_2 directly into the CdS lattice

as opposed to surface deposition may result in a greater number of high-quality p-n junctions and enhanced photocatalytic activity for hydrogen production.

Table 2: *Summary of several literature results for CdS/MoS_2 composite syntheses and tests.*

Synthesis method ***Morphology***	**Reaction conditions**	**Optimal cocatalyst loading (wt%)**	**Maximum H_2 production rate (mmol g^{-1} h^{-1})**	**Ref**
MoS_2 hydrothermally deposited on CdS nanowires (NW) in aqueous solution to form a core-shell structure *1D*	10 vol% lactic acid 300 W Xe lamp with UV filter	2	25	[74]
MoS_2 hydrothermally deposited on CdS in aqueous solution *0D*	10 vol% lactic acid 300 W Xe lamp with UV filter	2	4	[75]
CdS particles hydrothermally grown on 2D MoS_2 nanosheets in aqueous solution *2D*	10 vol% lactic acid 300 W Xe lamp with UV filter Light intensity: 50 mW cm^{-2}	20	7	[76]
Bulk MoS_2 prepared hydrothermally in aqueous solution, followed by ultrasonic treatment with CdS in DMF solvent for exfoliation and composite formation. *1D*	20 vol% lactic acid 300 W Xe lamp with UV filter Light intensity: 154 mW cm^{-2}	10	83	[77]
Glucose assisted MoS_2 hydrothermal synthesis on CdS NW in aqueous solution *1D*	0.35 M Na_2S and 0.25 Na_2SO_3 solution 300 W Xe lamp with UV filter Light intensity: 160 mW cm^{-2}	10	10	[78]

The incorporation of MoS_2 with CdS to form a nanocomposite has been known to facilitate the enhancement of CdS photostability, with the active edge sites of MoS_2 providing recombination centers for the dissolute Cd^{2+} to reform CdS, thereby reducing the extent of photo corrosion.[73] In addition, the incorporation of carbon has also been known to enhance catalyst stability and reduce the rate of electron-hole pair recombination, effectively ensuring a greater number of active species are available to catalyze the redox reactions on the catalyst surface.[79]

Multiwalled carbon nanotubes (MWCNTs) have drawn considerable attention as carbonaceous supports and dopants for several photocatalytic materials, with the 1-D morphology coupled with high electrical conductivity ensuring efficient separation of the photoexcited electrons, by providing an alternate transmission pathway away from the catalyst surface along the length of the nanotube.[79] Coupling photocatalysts with MWCNTs possessing a very high specific surface area allows for better dispersion of the catalyst in solution, ensuring enhanced active site exposure to the irradiated light and sacrificial reagents simultaneously, as the carbon material also provides excellent adsorption sites for many organic species.[80] With MWCNTs possessing a small band gap of between 0-1.1 eV[81], their use in photocatalyst nanocomposites improves the overall absorption of longer wavelength radiation and results in band gap narrowing, improving the material's ability to harness visible light for photocatalytic applications.

CHAPTER III – RESEARCH METHODOLOGY[1]

This work is aimed at developing photocatalytic material for two separate applications, organic contaminant degradation and hydrogen production from water splitting. This section will describe the catalyst synthesis techniques, characterization methods, and the experimental set up and procedure that were used for performance evaluation. Inspired by the development of black TiO_2 as a photocatalyst with significantly enhanced activity when compared to its pristine counterpart, a reduced (or "black") V_2O_5 was synthesized and tested for organic contaminant degradation. The appropriate characterization techniques were employed to identify the final product formed, determine the phases present, demonstrate the successful introduction of oxygen vacancies and their effect on the material optical band gap, and to evaluate the effect of reduction on the kinetics of the contaminant degradation reactions. Various organic dyes will be used as model contaminants to evaluate the effect of ionic charge on degradation performance.

In addition, a CdS/MoS_2 nanocomposites were developed via a one-pot synthesis technique, with MWCNTs used as a carbonaceous dopant. Photocatalytic performance was evaluated via hydrogen production experiments under visible light with lactic acid used as a sacrificial reagent. The MWCNT and MoS_2 loading were optimized and the material adequately characterized to quantify the dopant concentration in the material, identify phases present and determine the material's morphology.

[1] Part of this chapter is reprinted from "Surface microenvironment engineering of black V_2O_5 nanostructures for visible light photodegradation of methylene blue", by Ahmed Badreldin et al, 2021, *Journal of Alloys and Compounds*, 871.

Materials synthesis

All precursors used for materials synthesis were purchased from Sigma-Aldrich and used as received without any further purification.

Synthesis of black V_2O_5

2.5 g of ammonium metavanadate (NH_4VO_3) was measured in an alumina crucible and calcinated in a muffle furnace at 550°C under an air atmosphere, with a 40°C/min heating rate from an initial temperature of 25°C, and a subsequent heating time of 1 h at 550°C. The resulting orange sample was characterized and identified as pristine V_2O_5. 1 g of the prepared pristine V_2O_5 powder was weighed and ground with 0.22 g of sodium borohydride using a pestle and mortar (molar ratio of $NaBH_4$ to V_2O_5 at 1.05:1), forming bV_2O_5 that was labeled "bV_2O_5 (1:1.05)", and reduced in a tubular furnace at 400°C under an argon atmosphere, with a 1 h heating time (6.25°C/min) and 1 h reaction time at 400°C. The procedure was repeated with a $NaBH_4$ to V_2O_5 molar ratio of 1.25:1, with the sample labelled "bV_2O_5 (1:1.25)" to gauge the effect of extent of reduction on photoactivity. An inert argon atmosphere was used during the reduction of pristine V_2O_5 to ensure the induced oxygen vacancies would remain as such and not re-oxidize at the elevated operating temperature. In order to study the effect of the calcination environment during the preparation of pV_2O_5, NH_4VO_3 was also calcined under vacuum conditions in a tubular furnace, before being reduced using $NaBH_4$ to form the sample named "bV_2O_5 (vacuum)". The resulting samples was washed and centrifuged three times with de-ionized water, before being vacuum-dried at a pressure of -0.1 mbarg and 75°C for 7 h. Table 3 below summarizes the composites prepared and the reaction conditions.

Table 3*: Outline of various composites prepared.*

Composite	Precursors used	Synthesis conditions	Gas environment
pV_2O_5	NH_4VO_3	40°C/min heating rate in a muffle furnace followed by 1 h reaction time at 550°C	Air
bV_2O_5 (1:1.05)	pV_2O_5 and $NaBH_4$	6.25°C/min heating rate in a tubular furnace followed by 1 h reaction time at 400°C	Argon
bV_2O_5 (1:1.25)	pV_2O_5 and $NaBH_4$	6.25°C/min heating rate in a tubular furnace followed by 1 h reaction time at 400°C	Argon
bV_2O_5 (vacuum)	NH_4VO_3 and $NaBH_4$	NH_4VO_3 calcined at 550°C in a tubular furnace for 1 h under vacuum conditions. The resulting product was reduced with a 6.25°C/min heating rate in a tubular furnace followed by 1 h reaction time at 400°C	Vacuum calcination followed by reduction under argon

Functionalization of MWCNTs

Due to the highly hydrophobic nature of untreated MWCNTs, they were surface functionalized using a modified procedure[82] before being used for subsequent syntheses. 2 g of MWCNTs were added to a 30 mL solution of sulfuric acid and nitric acid (3:1 molar ratio) and refluxed at 100°C for 12 hours. Then the mixture was transferred to a 100 mL sealed Teflon-lined stainless-steel autoclave and maintained at 120°C for 6 hours. The resulting functionalized MWCNTs were then washed and centrifuged several times until the pH of the solution was near neutral. Subsequently,

the MWCNTs were vacuum filtered and dried in an oven at 60°C for 12 hours to obtain the final product.

Synthesis of CdS/MoS_2/CNTs nanocomposite

Cadmium nitrate tetrahydrate ($Cd(NO_3)_2.4H_2O$) and ammonium molybdate tetrahydrate ($(NH_4)_6Mo_7O_{24}.4H_2O$) were used as cadmium and molybdenum precursors respectively, with thiourea (CH_4N_2S) used as the sulfur source. Appropriate quantities of $Cd(NO_3)_2.4H_2O$ and $(NH_4)_6Mo_7O_{24}.4H_2O$ were dissolved in 30 mL of ethylenediamine and stirred for 1 hour. A certain quantity of the functionalized MWCNTs were then added to the solution, which was probe sonicated for 2 min to ensure a homogenously dispersed mixture and then magnetically stirred for a further 1 hour. Thiourea was then added to the mixture followed by stirring for 30 min, after which the solution was transferred to a Teflon-lined stainless-steel autoclave and maintained at 160°C for 24 h. The resulting dark green product was then washed and centrifuged several times with DI water to remove the excess thiourea and ethylenediamine solvent, followed by vacuum filtration and oven-drying at 50°C for 12 h.

The MoS_2 and MWCNTs loading was optimized in this study, with several samples being synthesized and tested. Optimal CNTs loading was determined by synthesizing a CdS - 3% MoS_2 sample (CM3) with 0%, 1%, 2%, 3%, 5% and 7% CNT concentrations, corresponding to samples CM3C0, CM3C1, CM3C2, CM3C3, CM3C5 and CM3C7. MoS_2 loading was optimized by preparing samples with a fixed CNTs concentration of 3% and theoretical Mo concentrations of 0%, 3%, 5%, 7% and 10%, corresponding to samples CM0C3, CM3C3, CM5C3, CM7C3 and CM10C3. Table 4 outlines the nomenclature used for the prepared samples and their respective composition.

Table 4: *Sample nomenclature and composition*

Sample	CNT content (%)	MoS_2 content (%)
CM3C0	0	3
CM3C1	1	3
CM3C2	2	3
CM3C3	3	3
CM3C5	5	3
CM3C7	7	3
CM0C3	3	0
CM3C3	3	3
CM5C3	3	5
CM7C3	3	7
CM10C3	3	10
CdS	0	0

Material characterization

Materials morphology

The morphology of materials was analyzed using high resolution scanning electron microscope (ESEM) images employing a FEI Quanta 400 environmental scanning electron microscope (FEI, Oregon, USA). The ESEM was operated at high vacuum mode with 30 Kv acceleration voltage and working distance of around 6.5 mm. An EDAX Octane Elect EDS System with silicon drift detector was used for EDS signal collection and analysis. The high-resolution transmission electron microscope (HRTEM) images were taken by a FEI Talos F200 with 200 kV acceleration voltage. HRTEM samples were prepared by first ultrasonication in ethanol, followed by drop-casting the dispersion onto TEM Cu grid (400 mesh) with holey film for characterization.

XRD Analysis

The prepared samples were analyzed using powder XRD spectra collected via a Rigaku Ultima IV Multipurpose X-ray Diffractometer (Rigaku Corp., Tokyo, Japan) equipped with cross beam optics, fixed monochromator and a scintillation counter. The XRD radiation source (Cu-Ka) was operated at 40 kV and 40 mA. A divergence slit (2/3°), divH.L. Slit (10 mm), scattering slit (2/3°), and a receiving slit (0.3 mm) were used. The XRD data was collected using a continuous scan mode in the 2θ range of 5–80° with a step width of 0.02° and a 1°/minute scan speed. Integrated Rigaku PDXL2 software with PDF4 + 2019 database was used for peak identification and phase analysis.

Material optical property analysis

UV–Vis–NIR diffuse reflectance spectroscopy (DRS) was performed on the samples using a PerkinElmer Lambda 950 Spectrophotometer in the range of 250–800 nm to quantify the solid-state absorption of the prepared solids in the UV – visible light region. Using DRS data, Tauc plots were developed to calculate the material direct band gaps.

X-ray Photoelectron Spectroscopy (XPS)

An AXIS Ultra DLD X-ray Photoelectron Spectroscopy (XPS) was used to collect large area survey and high-resolution X-ray Photoelectron spectra of the pristine and black vanadium oxide samples, as well as the CM0C3 and CM5C3 samples. The XPS Al mono (K-alpha) radiation (1486.6 eV) source was operated at 15 kV and 15 mA emission current. The high-resolution spectra of Vanadium 2p and Oxygen 1s peaks were collected with pass energy of 20 eV and 0.1 eV step size. An integrated Kratos Vision data processing software was used for calibration of spectra, peak analysis and deconvolution.

Performance evaluation

Photocatalytic organic contaminant degradation

Photocatalytic degradation efficiency of the prepared pristine and black V_2O_5 samples was evaluated using methylene blue (MB) as the model contaminant. In addition, methylene orange (MO) and quinoline yellow (QY) were used for comparative analysis of the effect of contaminant charge on the degradation efficiency. Material adsorptive capacity was determined by preparing a 50 mL solution with the target initial concentration of MB and adding 25 mg of the prepared photocatalyst material to it. This was followed by probe sonication for 1 min and subsequent magnetic stirring in dark conditions for 3 h, which was found to be adequate to reach equilibrium. 3 mL samples were taken before and after the adsorption test using a standard 10 mL syringe, filtered with a 0.45 μm mixed cellulose-ester filter paper and analyzed with liquid-phase UV-Vis spectroscopy to quantify the amount of MB adsorbed.

For the photodegradation experiments, a 50 mL solution of MB was prepared with an initial MB concentration that ensures 20 mg/L of the contaminant remained dissolved in solution after adsorptive equilibrium was achieved. 25 mg of the photocatalyst was added to the new stock solution, probe sonicated for 1 min and transferred to a 50 mL petri-dish, which was irradiated using an artificial solar simulator at intensity of 700 W m^{-2} for 1 h under continuous stirring, shown in Figure 16 below. The solar simulator was calibrated using a standard CMP6 Kipp & Zonen pyranometer with a spectral range of 285–2800 nm.

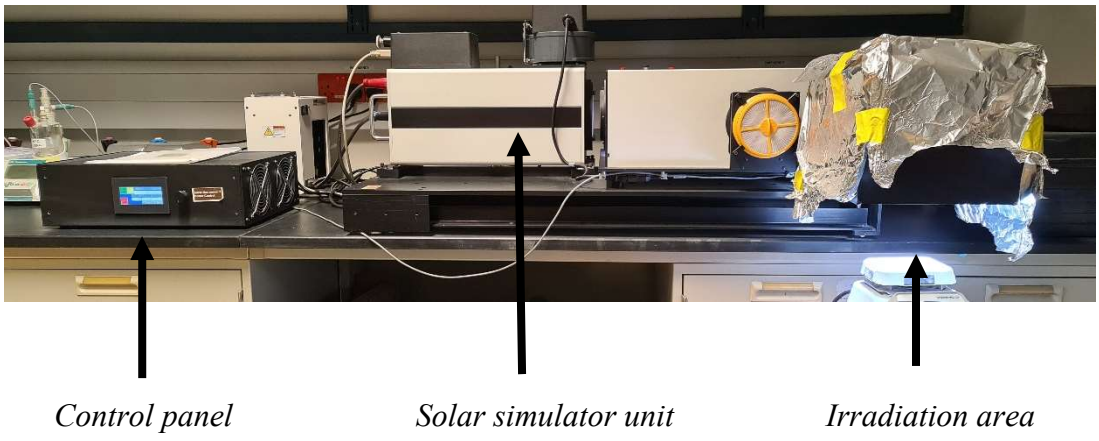

Figure 16: *Solar simulator set-up for organic contaminant degradation.*

2 mL samples were taken using a 10 mL syringe at continuous intervals during the experiment, with the samples analyzed via liquid-phase UV-Vis spectroscopy to quantify the extent of contaminant degradation. Samples were taken in 2 min intervals for the first 10 min and subsequently at 10 min intervals for the next 50 min.

Similar experiments were conducted using MO and QY as the target contaminants. The absorbance wavelength (λ_{max}) values that were used for UV-Vis spectroscopy to quantify MB, MO and QY quantifications were 664 nm, 464 nm and 414 nm, respectively. Degradation percentage was calculated as:

$$\text{Degradation } (\%) = \frac{100(C_0 - C_t)}{C_o}$$

Where C0 is the initial contaminant concentration and Ct is contaminant concentration after time (t).

Photocatalytic hydrogen production

The hydrogen production experiments were conducted in a sealed, circular 50 mL stainless-steel reactor with a quartz cover, equipped with gas inlet and outlet ports, a chiller and thermocouple for temperature control. The reactor is connected to a HIDEN Analytical HPR-20 Q/C Benchtop Gas Analysis mass spectrometer (MS) at the outlet for product gas quantification (Figure 17). The MS equipment continuously records the partial pressures of O_2, N_2, water vapor, argon and hydrogen (corresponding to m/z values of 32, 14, 18, 40 and 2, respectively) at 20 s intervals. O_2 and N_2 were monitored to ensure air had been fully purged from the system before the start of the experiment. Argon was used as the purge gas and since the equipment was operated in a continuous mode, the flow was monitored to ensure consistency. Water has a contribution at an m/z value of 2, the same peak position as hydrogen, with this contribution quantified and subtracted from the data to ensure the partial pressure corresponding to the species at 2 m/z was due to hydrogen only. Before any hydrogen production experiments, photolysis experiments without any suspended catalyst were conducted to ensure no hydrogen was produced from the sacrificial reagent alone under solar irradiation.

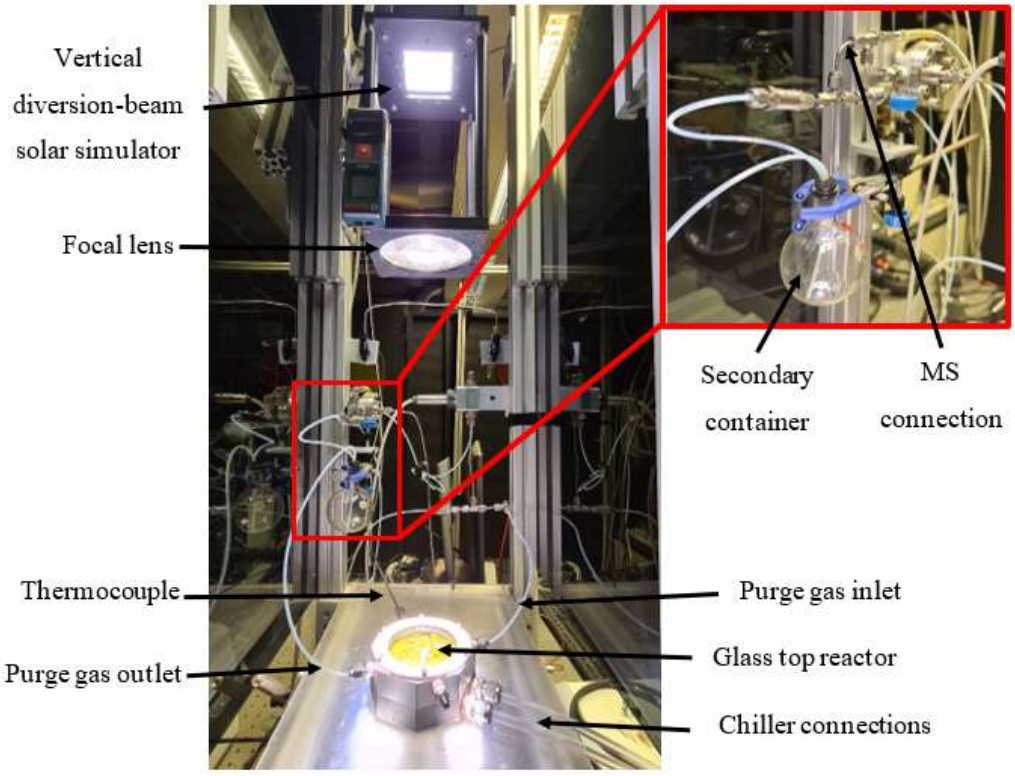

Figure 17: *Vertical divergent-beam solar simulator used for HER experiments.*

In a typical hydrogen production experiment, 5 mg of the catalyst was suspended in 25 mL of 0.5 M lactic acid solution and probe sonicated for 1 min to ensure good dispersion of the catalytic material. The solution was then transferred into the reactor, maintained at 25°C using an external chiller, and purged with argon flowing at 55 mL/min under dark conditions. The mass spectrometer was set to record continuous measurements every 20 s, until all dissolved O_2, N_2 and other gases were removed and the baseline for all species involved were stabilized. 50 µL of hydrogen was then injected into the reactor as a reference before irradiation, using a 250 µL gas tight syringe, and the reactor was purged with argon to flush out the injected hydrogen. The flushed hydrogen was quantified with the MS by calculating the area under the 2 m/z peak and equating it to 50 µL of hydrogen. This was used as a standard for quantification of the evolved hydrogen gas during

the experiments under solar light irradiation. After the re-stabilization of the baseline following the hydrogen injection, the reactor was then irradiated for 5 h using a vertical diversion beam solar simulator equipped with an air mass 1.5 global filter. The simulator was operated with a 1000 W ozone-free xenon lamp, with the light intensity at the surface of the solution in the reactor maintained at approximately 1000 W m^{-2}. At the end of the experiment, the recorded data was exported to Microsoft Excel for data analysis.

CHAPTER IV – RESULTS AND DISCUSSION[2]

This section will report experimental findings as well as material characterization data related to all synthesized composites.

Vanadium oxide (V_2O_5)

Material characterization

Material morphology and composition

SEM images of pV_2O_5 and bV_2O_5 are shown in Figure 18. Pristine V_2O_5 exhibits a brick-like morphology with very smooth surfaces and varying sizes. However, following the reduction procedure, clear surface defects growing perpendicularly from the bV_2O_5 surface are visible, which indicate an increase in the material surface area.

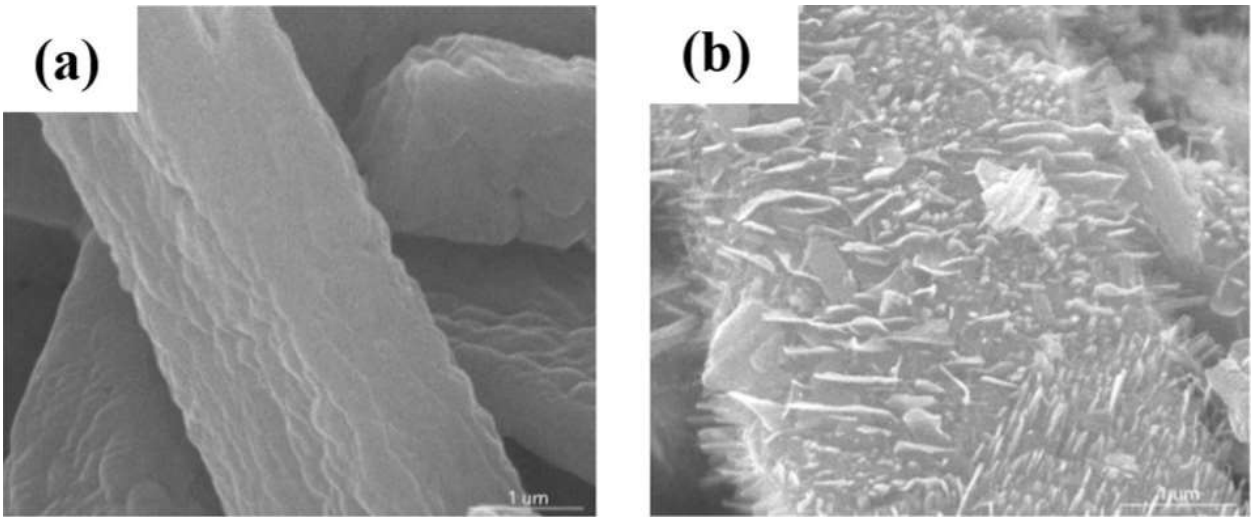

Figure 18: *SEM images of a) pV_2O_5 and b) bV_2O_5.*

[2] Part of this chapter is reprinted from "Surface microenvironment engineering of black V_2O_5 nanostructures for visible light photodegradation of methylene blue", by Ahmed Badreldin et al, 2021, *Journal of Alloys and Compounds*, 871.

High-resolution TEM images of the pV_2O5 and bV_2O_5 samples (Figure 19) shows the predominant growth of the (001) facet, with a corresponding lattice d-spacing of 0.43 nm. Lattice defects in the form of oxygen vacancies are visible on the bV_2O_5 surface, verifying the successful reduction procedure and surface defect formation.

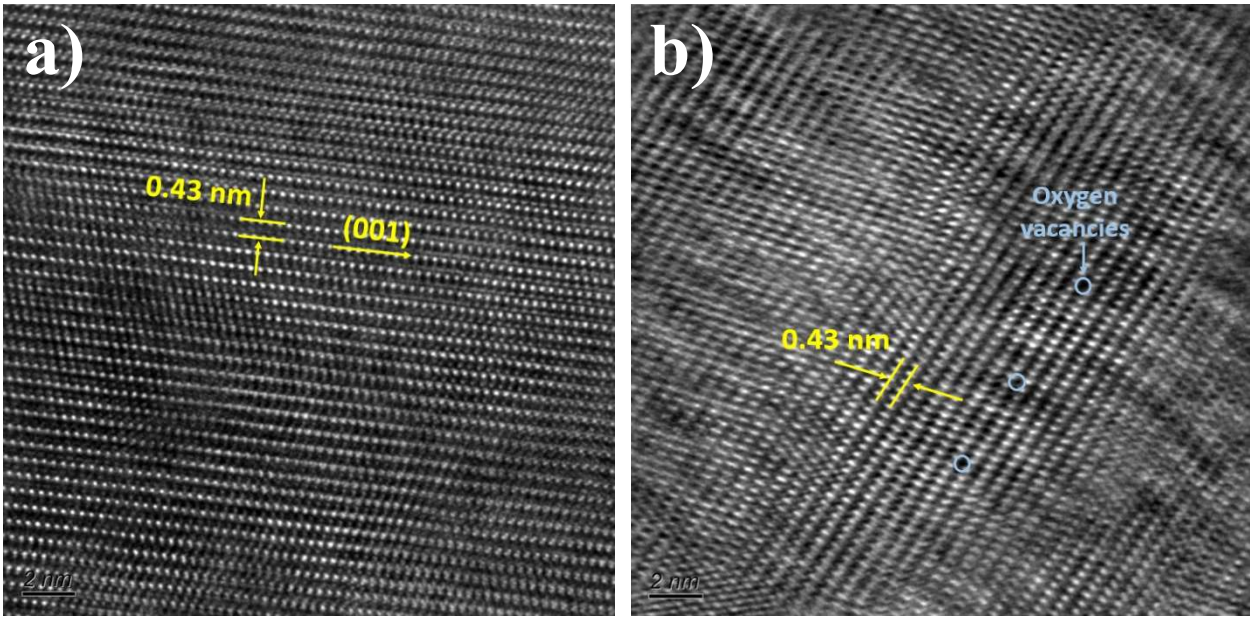

Figure 19: *TEM images with lattice spacing for a) pV2O5 and b) bV2O5, with oxygen vacancies shown on the bV2O5 surface.*

Energy dispersive spectroscopy (EDS) on the bV_2O_5 sample shows a predominant quantity of vanadium and oxygen content, indicating the high purity of the material, as shown in Figure 20. In addition, the presence of a small amount of sodium (3 wt%) can be attributed to the formation of a Na-V_2O_5 phase as a remnant of the reduction with $NaBH_4$. The induced oxygen vacancies result in the presence of a high concentration of vacant D-orbitals which become binding sites for OH^- ions in aqueous solution. During the reduction of pV_2O_5 with $NaBH_4$, cationic sodium ions can attach to this negatively charged surface, forming the Na-V_2O_5 phase to a limited extent.

Sodium intercalation in photocatalytic material has been known to have a positive effect on photocatalytic activity, with surface area enhancement and increased charge separation induced in the material linked to the presence of sodium doping.[83] While the effect of sodium doping is subtle and limited due to the relatively small quantity present, it can still influence the photocatalytic activity of the bV_2O_5 material in addition to the effect of the surface defects. The EDS spectra also shows the presence of platinum and carbon due to the platinum coating and carbon tape used during analysis respectively.

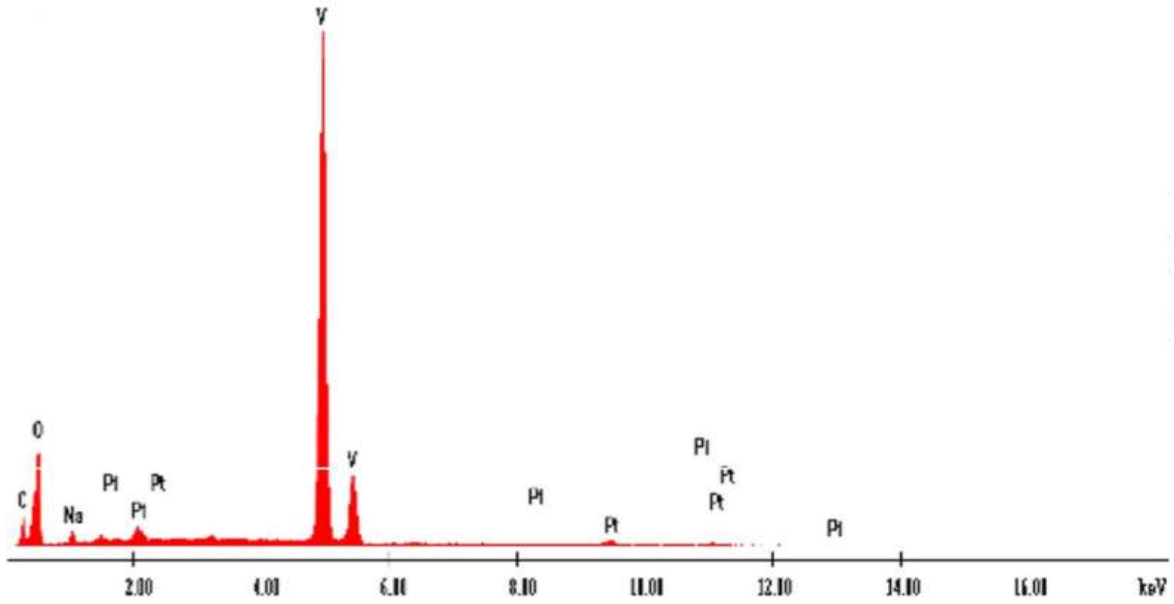

Figure 20: *EDS spectra of bV_2O_5.*

Material crystallinity and observed phases

X-ray diffraction (XRD) analysis was performed on the pristine and black V_2O_5 samples to study crystallinity and determine the predominant phases present in the materials. The observed XRD patterns are in good agreement with (PDF) 04-007-0398 for V_2O_5. Both samples show the presence of predominant polar (001) and non-polar (110) facets at 20.31° and 26.15°, respectively, with the

peak intensities for both facets diminished in the case of bV_2O_5 (Figure 21). In addition, the presence of the peaks at 18.45° and 27.93° correspond to the formation of the Na-V_2O_5 and V_4O_9 phases respectively.[84,85] As described earlier, the Na-V_2O_5 phase was formed as a result of Na^+ electrostatically bound to the negatively charged bV_2O_5 surface, and the presence of peaks corresponding to the V_4O_9 phase further verify the partial removal of oxygen atoms from the crystal lattice and subsequent formation of oxygen vacancies in bV_2O_5.

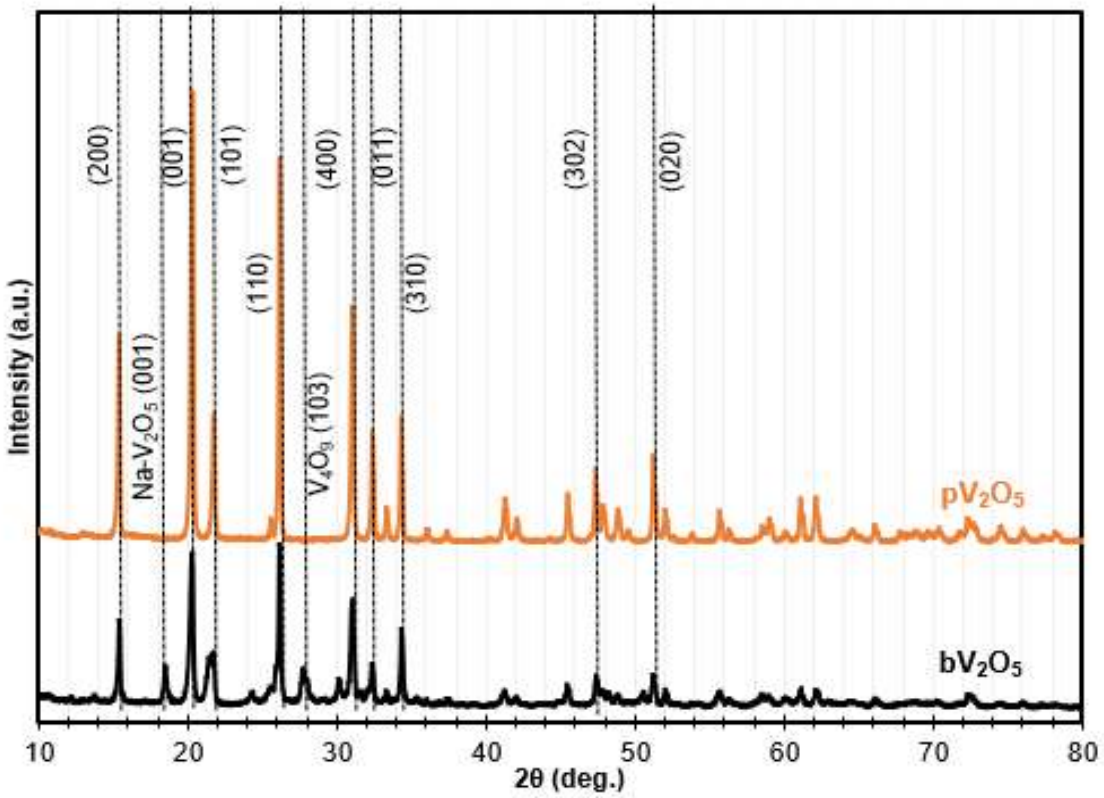

Figure 21: *XRD spectra of pV_2O_5 and bV_2O_5.*

Based on the obtained XRD spectra, the crystallite size of both samples was determined using the Scherrer approximation as shown below:

$$D = \frac{K\lambda}{\beta cos\theta}$$

Where D is the crystallite size (m), K is the dimensionless shape factor (typically holding a value of 0.9 for spherical crystallites), λ is the x-ray wavelength (0.15406 Knm), β is the full width at half maximum of the XRD peak and θ is the Bragg angle.[86] Crystallite sizes were determined to be 41.45 nm and 26.46 nm for pV_2O_5 and bV_2O_5 respectively, which indicates a decrease in crystallite size upon reduction. Previous work on black TiO_2 has shown a reduction in crystallite size during the hydrogenation of pristine TiO_2,[87] which is consistent with the finding herein. However, defect formation in the form of oxygen vacancies can result in peak broadening due to increased strain distribution, which may account for the significant reduction in crystallite size by nearly 40%, as calculated by the Scherrer equation. Since the Scherrer approximation does not account for strain contributions, the Williamson-Hall method was also employed to calculate the lattice sizes with these strain contributions factored in. The Williamson-Hall approximation is as follows:[88]

$$\beta cos\theta = \left(\frac{K\lambda}{D}\right) + 2A\varepsilon sin\theta$$

Where constants A and ε typically have values approaching unity.[88] The average crystallite sizes as approximated by the Williamson-Hall method were found to be 43.2 and 35.5 nm for pV_2O_5 and bV_2O_5 respectively. Despite the obvious reduction in crystallite size which is typically attributed to lower photocatalytic performance, crystallite sizes larger than 20 nm are usually sufficient for the suppression of electron-hole pair recombination due to a large enough charge migration distance.[89] Table 5 summarizes the crystallite sizes determined using both methods.

Table 5: *Average crystallite sizes for both prepared samples.*

Sample	Average crystallite size (nm)	
	Scherrer	**Williamson-Hall**
pV_2O_5	41.45	43.2
bV_2O_5	26.46	35.5

Surface chemical states and electronic structures

The effect of the reduction process on the chemical states and electronic structures of the transition element present was evaluated via x-ray photoelectron spectroscopy (XPS) of the pristine and black V_2O_5 samples, with the general survey scan of both materials shown in Figure 22.

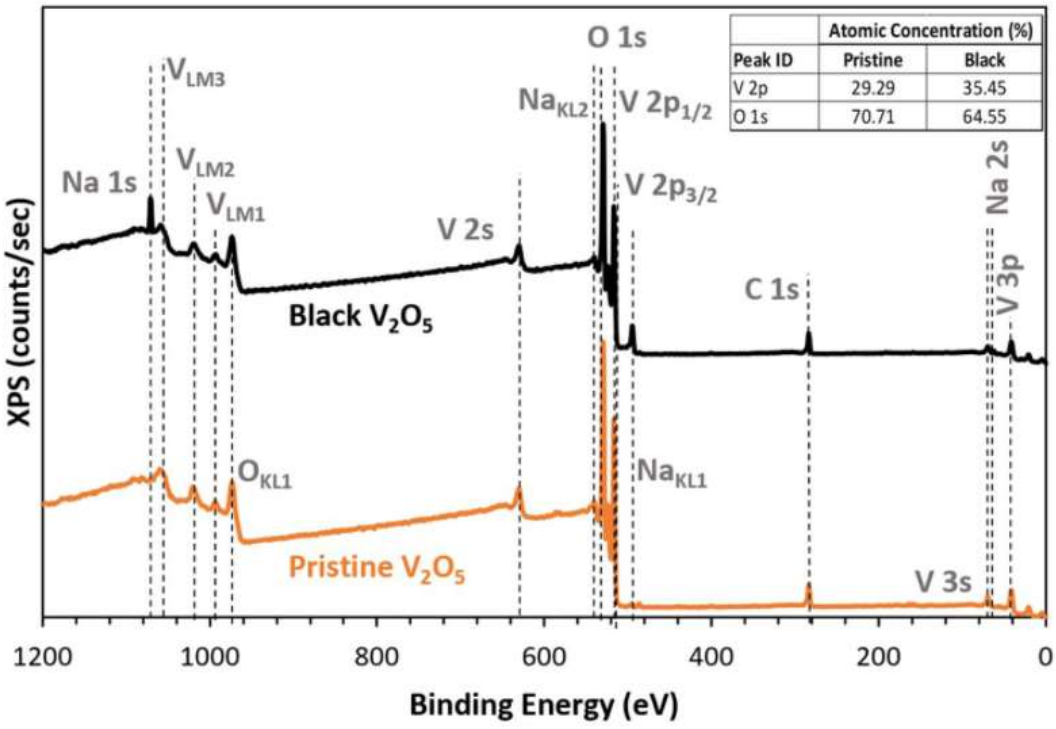

Figure 22: *XPS full survey scan for pV_2O_5 and bV_2O_5.*

Both materials show a predominant presence of vanadium and oxygen peaks, with the bV_2O_5 sample also showing additional peaks for sodium, validating the notion of sodium doping during the reduction process as shown in the EDS spectra (Figure 19).

Higher resolution V 2p spectra show significant differences upon peak deconvolution, as shown in Figure 23a. Pristine V_2O_5 shows the presence of $V^{5+}{}_{3/2}$ and $V^{5+}{}_{1/2}$ at binding energies of 517.2 eV and 524.4 eV respectively, which is in good agreement with known V 2p spectra for V_2O_5. However, the reduction process induces the formation of $V^{3+}{}_{3/2}$ at a binding energy of 515.4 eV and a reduction in intensity of the main $V^{5+}{}_{3/2}$ peak at 517.2 eV. With the reduction process removing oxygen atoms from the crystal lattice, the excess electrons left behind react with V^{5+} and partially reduce it to V^{3+}. In addition, deconvolution of the O1s peak shows the presence of surface hydroxide groups in the bV_2O_5 sample only, as shown in Figure 23b, a feature commonly attributed to the presence of surface defects like oxygen vacancies.

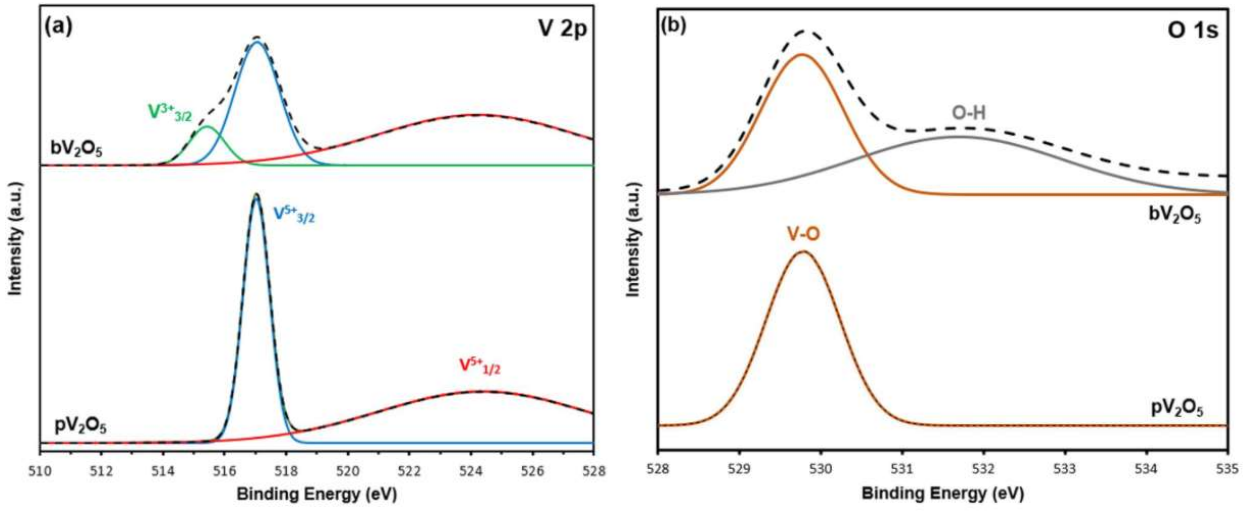

Figure 23: *a) V 2p and b) O1s deconvoluted spectra.*

Photocatalytic performance

Adsorption tests

Reduced, or black, V_2O_5 was prepared by subjecting pristine V_2O_5 to a facile reduction scheme using $NaBH_4$ as the reducing agent. Prior to performance evaluation for organic contaminant degradation, the effect of the reduction process on material adsorption was first determined, using MB as the target organic contaminant. The equilibrium adsorptive capacity, q_e (mg/g) of the pristine and black V_2O_5 nanocomposites was determined using the equation below:

$$q_e = \left(\frac{C_0 - C_e}{m}\right) \times V$$

Where C_0 and C_e are concentrations of MB at the start of the adsorption experiments and at equilibrium respectively (mg/L), m is the mass of the adsorbent (g) and V is volume of the solution (L). The adsorption experiments with both V_2O_5 samples were conducted for 3 h in dark conditions, using an initial solution of 100 ppm MB. After the adsorption equilibrium was established, pV_2O_5, bV_2O_5 (1:1.05), bV_2O_5 (1:1.25) and bV_2O_5 (vacuum) materials were found to have equilibrium adsorptive capacities of 50.0 mg/g, 151.2 mg/g, 189.6 mg/g and 177.2 mg/g with MB respectively. However, the bV_2O_5 (1:1.05) sample proved to have the fastest kinetics for contaminant degradation, as will be described in the following sections, and will be referred to as bV_2O_5 from now on. The increase in adsorptive capacities may be attributed to an increased porosity in the black V_2O_5 sample and a higher negative surface charge due to the reduction process. Table 6 summarizes the BET surface areas and zeta potential at near neutral conditions for the prepared samples and compared with known adsorbents in literature, namely activated carbon (AC), carbon nanotubes (CNTs) and graphene oxide (GO).

Table 6: *A comparison of surface area, pore volume, equilibrium adsorptive capacity and zeta potential values.*

Material	S_{BET} (m^2/g)	V_P (cm^3/g)	q_e (mg/g)	Zeta potential (mV)	Ref
pV_2O_5	3.0	0.047	50.0	-20.8	This work
bV_2O_5	3.2	0.052	151.2	-61.2	This work
AC	1688	1.04	270.3	-32	[90]
CNTs	177	0.54	188.7	-58	[90]
GO	32	0.11	243.9	-54	[90]

The prepared V_2O_5 samples seem apparently inferior to the carbonaceous adsorbents typically used for the removal of organic contaminants. However, this behavior can be attributed to the extremely porous nature of AC, CNTs and GO, with the total pore volume and surface area several orders of magnitude larger than the vanadium-based materials. Figure 24 below outlines the adsorption capacity of all materials shown in Table 5 normalized with respect to total surface area.

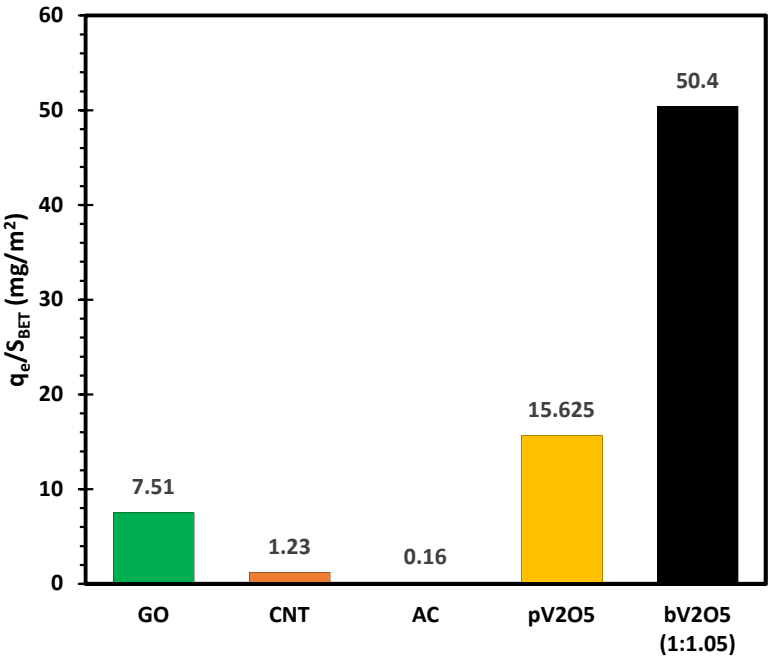

Figure 24: *Comparison of material adsorption capacities normalized by BET surface area.*

Based solely on surface properties normalized with the surface area, black V_2O_5 exhibits an adsorptive surface far superior to other adsorbents commonly used. The oxygen vacancies induced on the surface of black V_2O_5 are initially positively charged and act as binding sites for a larger concentration of OH^- ions in aqueous solution, inducing a net negative surface charge, as also verified by the highly negative zeta potential. This negative charge induces electrostatic attraction between the surface and cationic MB molecules, increasing the adsorptive capacity for the dye. In addition, the increase in the absolute zeta potential of black V_2O_5 compared to pristine V_2O_5 is indicative of a highly dispersed suspension due to repulsion between catalyst particles, which aids in increasing adsorption of MB due to a larger exposed surface, and enhances its photocatalytic activity.

Contaminant degradation

Photocatalytic degradation experiments were conducted using MB as the model contaminant, with all experiments conducted with a fixed catalyst loading of 0.5 g/L and solution volume of 50 mL. Based on the results from the adsorption tests, 0.025 g of pristine and black V_2O_5 were found to have an adsorptive capacity of nearly 76 and 25 ppm of MB, respectively. To eliminate the effect of initial contaminant concentration when comparing the photocatalytic performance of the pristine and black V_2O_5, stock solutions were initially prepared with different MB concentrations of 95 ppm and 45 ppm for pristine and black V_2O_5 samples, respectively. This warrants that 20 ppm of MB remained dissolved in solution after the 3 h adsorption period prior to irradiation. For each experiment, 25 mg of the catalyst was added to the solution, sonicated for 1 min and magnetically stirred in dark conditions for 3 h to ensure adsorption equilibrium had been achieved and 20 ppm of MB remained in solution. The mixture was then transferred to a 50 mL petri-dish and irradiated with the solar simulator for 1 h under continuous magnetic stirring. Samples were taken at regular time intervals for UV-Vis analysis and quantification of the MB concentration remaining in solution. Experiments were conducted on the synthesized pV_2O_5, bV_2O_5 (1:1.05), bV_2O_5 (1:1.25) and bV_2O_5 (vacuum), in addition to synthesized ZnO, commercial P25 (TiO_2) and synthesized black TiO_2 for comparison purposes, with the results depicted in Figure 25.

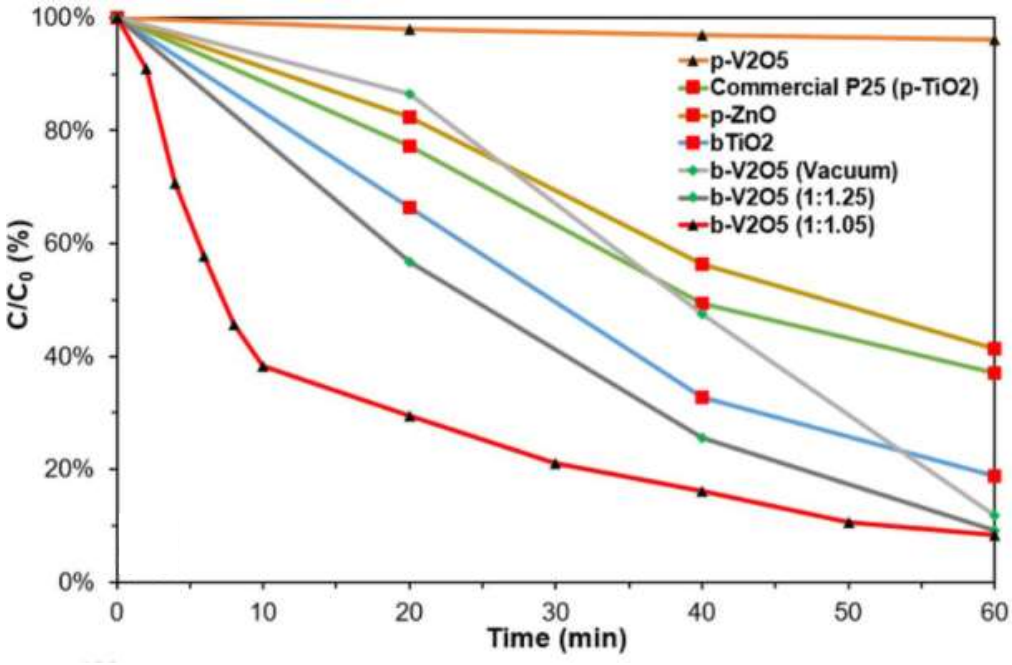

Figure 25: *Photocatalytic degradation of MB.*

After 1 h of irradiation, all the synthesized bV_2O_5 samples achieved more than 90% MB degradation. However, they differed in terms of their kinetic behavior. The bV_2O_5 (vacuum) sample showed apparent initial sluggish degradation kinetics, which may be linked to increased MB desorption rates at the start of the experiment. The bV_2O_5 (1:1.05) sample exhibited faster kinetics for MB degradation when compared to bV_2O_5 (1:1.25), particularly within the first 10 min, indicating that the higher reducing agent concentration and hence, greater extent of reduction may have induced a higher ratio of bulk to surface oxygen vacancies, with the bulk vacancies acting as charge recombination centers and resulting in slower kinetics. In addition, the bV_2O_5 samples all performed significantly better than the reference photocatalysts used, with pV_2O_5, ZnO, $pTiO_2$ and $bTiO_2$ only achieving 3%, 58.7%, 62.9% and 81.3% MB degradation under identical reaction conditions.

The enhanced photoactivity of bV_2O_5 compared to $bTiO_2$ can be attributed to the fact that V_2O_5 has a higher lattice-oxygen density when compared to TiO_2, allowing the formation of a larger density of surface oxygen vacancies. In addition, the higher oxidation state of the transition metal involved allows for the potential formation of additional valence states (V^{4+} and V^{3+}) that can act as electron-trap sites, increasing charge separation and further improving degradation performance.

Degradation kinetics

Photocatalytic degradation of MB is known to follow pseudo-first order kinetics of the form shown below:[91]

$$C = C_0 e^{-kt}$$

Where C_0 and C are contaminant concentrations before the start of the experiment and time (t) respectively, and k is the first-order degradation rate constant. Plotting $-\ln\left(\frac{C_t}{C}\right)$ vs t, as shown in Figure 26, allows for the determination of the rate constant by calculating the slope of the fitting curve. The optimal bV_2O_5 (1:1.05) ($k = 0.0408\ min^{-1}$) sample showed a nearly 58-fold increase in degradation kinetics compared to pV_2O_5 ($k = 0.0007\ min^{-1}$), verifying the sharp enhancement in photoactivity of V_2O_5 for MB degradation due to the facile reduction process.

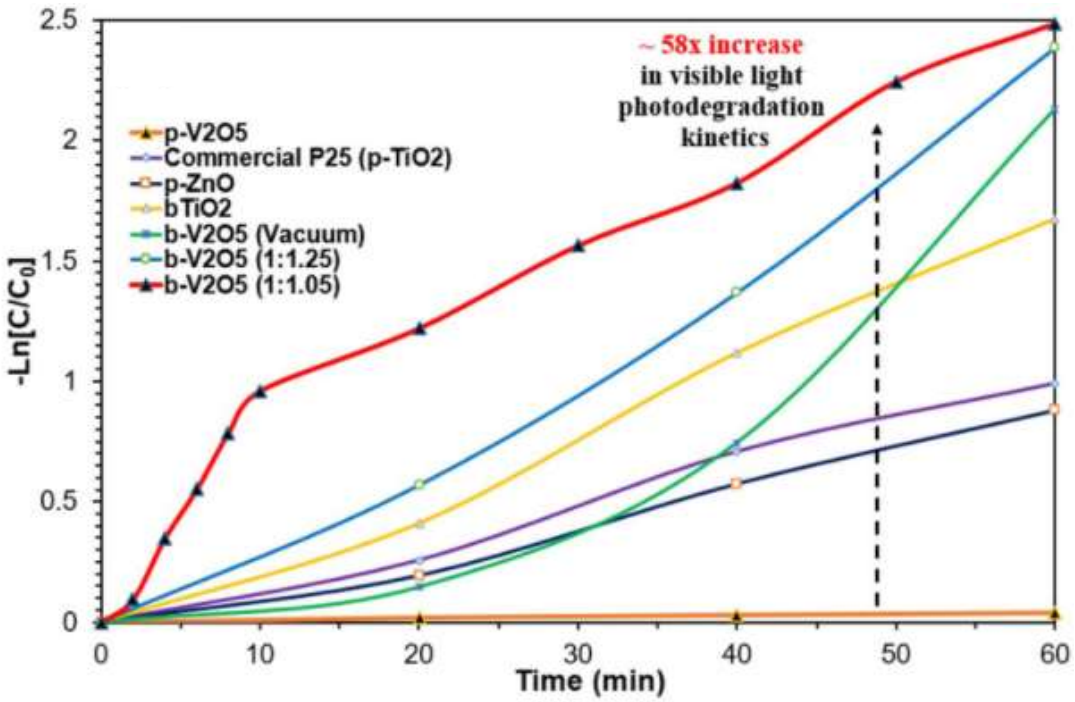

Figure 26: *Pseudo firsts order degradation kinetics.*

Effect of contaminant charge

The effect of contaminant charge on the degradation efficiency of bV_2O_5 was studied by evaluating the photocatalyst performance for degradation of a neutral dye, quinoline yellow (QY), and an anionic dye, methylene orange (MO). The adsorption capacity of QY and MO was experimentally measured in a manner like that used for MB, with the initial concentrations adjusted to ensure 20 ppm of the dye remained in solution after adsorption equilibrium had been achieved. Table 7 summarizes the equilibrium adsorption capacity of bV_2O_5 for MB, QY and MO.

Table 7: *Effect of contaminant charge on equilibrium adsorptive capacity with bV2O5.*

	Methylene blue	**Quinoline yellow**	**Methylene orange**
q_e (mg/g)	151.2	9.8	6.4

The sharp reduction in adsorption of MO is expected because of electrostatic repulsion between the like-charged catalyst surface and contaminant species. bV_2O_5 shows a slightly higher adsorption capacity for QY than MO, with the neutral species not affected by attractive or repulsive forces stemming from the negatively charged catalyst surface. However, the large molecular size of QY as compared to MB may sterically hinder its adsorption onto bV_2O_5 with limited access to the smaller pores of the catalyst.

Degradation experiments under identical reaction conditions to that for MB were then conducted, with the results shown in Figure 27 below.

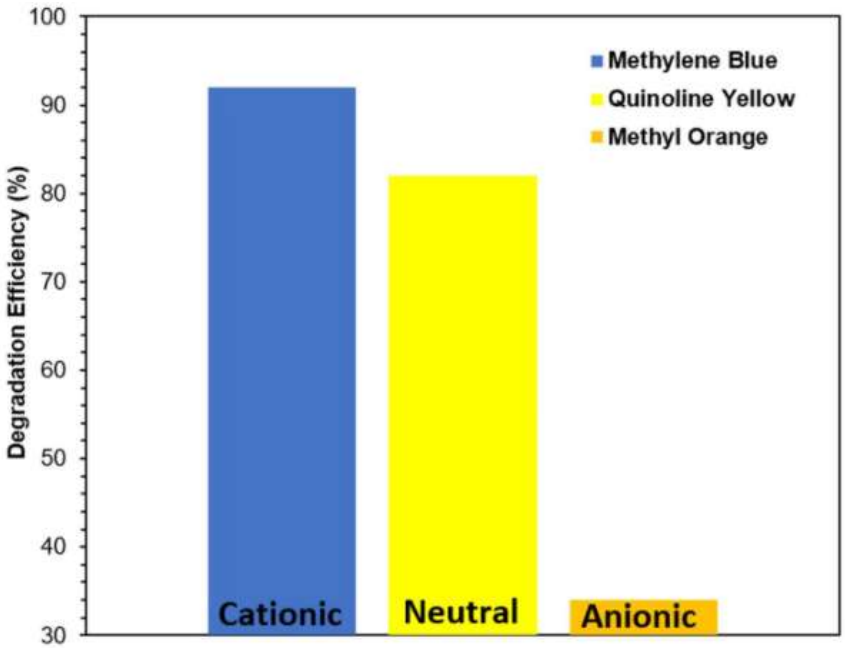

Figure 27: *Effect of contaminant charge on degradation efficiency with bV2O5.*

After 1 h of reaction time, the highest degradation was achieved for MB (92%) and lowest degradation was for MO (34%), with QY degradation (82%) slightly less than MB degradation efficiency. The low degradation of MO can be related to the electrostatic repulsion involved with

bV_2O_5, causing a reduction in contaminant contact with the catalyst surface. The highest degradation efficiency of MB can be explained by the smaller molecular size compared to QY, which help to reduce steric hindrance and allowing greater access to the catalyst pores and a greater number of active sites for degradation reactions to take place. In addition, the cationic species may possess a greater affinity for negatively charged superoxide radicals, formed during the photocatalytic process, as will be discussed in subsequent sections.

Catalyst recyclability

To evaluate material stability and recyclability, 5 MB degradation cycles of 1-hour each were performed using the same catalyst, with the results shown in Figure 28 below. After the five cycles, MB degradation dropped from 92% to 79%. The decrease in degradation efficiency can partly be attributed to the loss of material for every sequential run, resulting in a less than 0.5 g/L loading for subsequent cycles. Factoring for the loss of catalytic material, bV_2O_5 exhibits high operational stability, with partial re-oxidation of oxygen vacancies and particle agglomeration during photocatalytic operation perhaps accounting for the slightly reduced degradation efficiency.

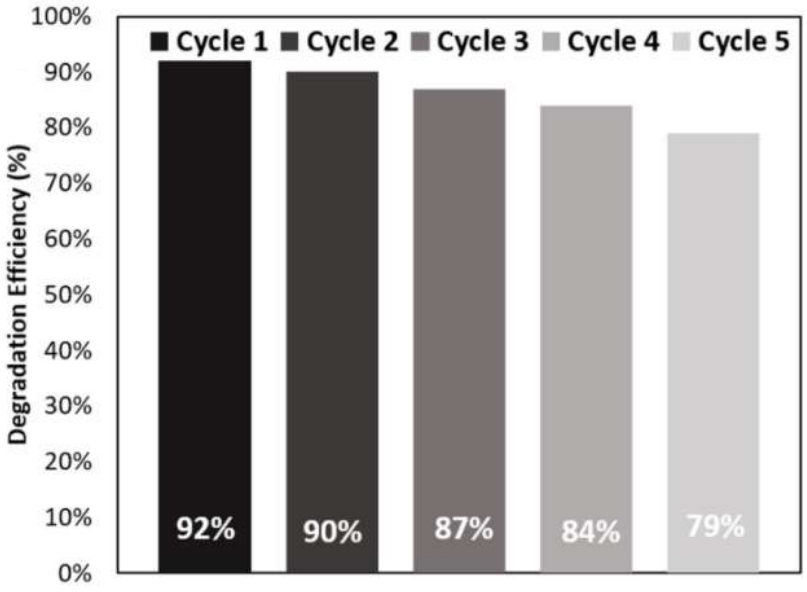

Figure 28: *Catalyst recyclability*

Mechanism of bV_2O_5 photocatalysis

The significant improvement in photoactivity of bV_2O_5 compared to pV_2O_5 can be attributed to the induced surface defects in the form of oxygen vacancies. The oxygen vacancies are formed when oxygen atoms are removed from the lattice structure during the reduction process with $NaBH_4$, initially leaving positively charged defects on the surface. The proposed mechanism for photocatalytic dye degradation using bV_2O_5 is similar to that reported for its pristine counterpart.[92] V_O^{2+} represents the positively charged surface oxygen vacancies at the time of induction.

$$V_2O_5 + hv \rightarrow V_2O_5(e_{cb}^-) + V_2O_5(h_{vb}^+)$$

$$V_O^{2+} + V_2O_5(e_{cb}^-) \rightarrow V_O^+$$

$$V_O^+ + O_2 \rightarrow V_O^{2+} + \bullet O_2^-$$

$$V_2O_5(h_{vb}^+) + OH^- \rightarrow V_2O_5 + \bullet OH$$

$$dye + \bullet OH + \bullet O_2^- \rightarrow \text{degradation products}$$

The oxygen vacancies on the surface form intermediate energy levels between the conduction and valence bands, effectively narrowing the optical band gap and enhancing photocatalytic properties in the visible light region.[93] In addition, they also act as trapping sites for the photoexcited electrons, lowering electron – hole pair recombination and increasing charge separation. A photodegradation schematic for the bV_2O_5 photocatalyst is shown in Figure 34, depicting the type-II heterojunction formed between the pristine and reduced V_2O_5 surface. With the concentration of the reducing agent controlled to ensure the hydrogenation reaction forms a high ratio of surface to bulk oxygen vacancies, the formation of bV_2O_5 occurs predominantly on the surface, with pV_2O_5 being the dominant phase in the bulk, with the interface between the 2 phases acting as a heterojunction for charge transfer. Figure 29 shows that the attained reduced V_2O_5 possesses a Z-scheme mechanism, whereby a photoexcited e^- from the VB of pV_2O_5 migrates to the CB on the same crystal, followed by transference to the VB of a coupled black V_2O_5 crystal acting as a trap state.[94,95] The same e^- can then be photoexcited to the CB with less energy, namely visible-light photons, to participate in the formation of a superoxide radical.

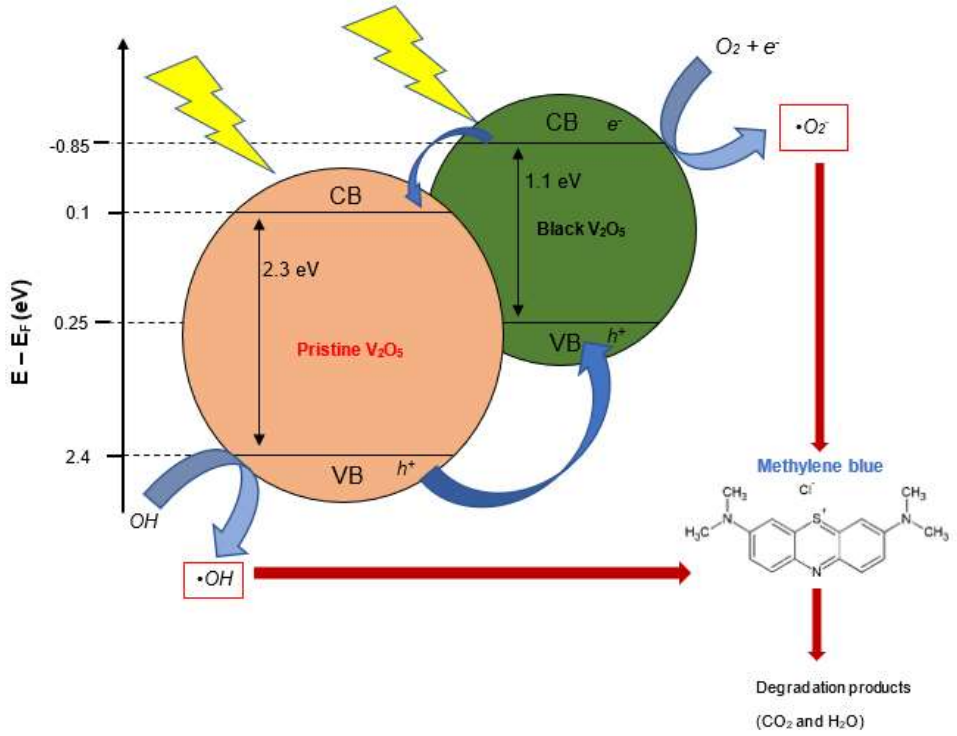

Figure 29: *Mechanism of photocatalytic degradation with the pV_2O_5/bV_2O_5 composite.*

Surface oxygen vacancy sites can act as binding sites for the adsorption of O_2 molecules from the aqueous environment. The trapped electron is transferred to the O_2 molecule, generating the superoxide radical anion $\bullet O^{2-}$, which is a strong oxidizing agent, and enhances the degradation of the organic dye.[96] The positively charged holes in the valence band react with the hydroxide OH^- ions in solution to form hydroxide radicals •OH. The hydroxide radicals, •OH, and the superoxide anionic radicals, $\bullet O^{2-}$, then oxidize the organic dye to form the degradation products. The individual contributions of both oxidizing species were evaluated via degradation experiments involving reactive oxidative species (ROS) scavengers, to determine the main ROS involved in the degradation mechanism. Isopropyl alcohol and hydroquinone were used as ROS scavengers for •OH and $\bullet O^{2-}$ radicals respectively, with the results shown in Figure 30 confirming

the $\bullet O^{2-}$ radicals as being the dominant ROS species. Hydroxide radical scavenging did not affect the degradation efficiency of MB to any significant extent, however, the absence of $\bullet O^{2-}$ decreased the degradation efficiency by nearly 80%.

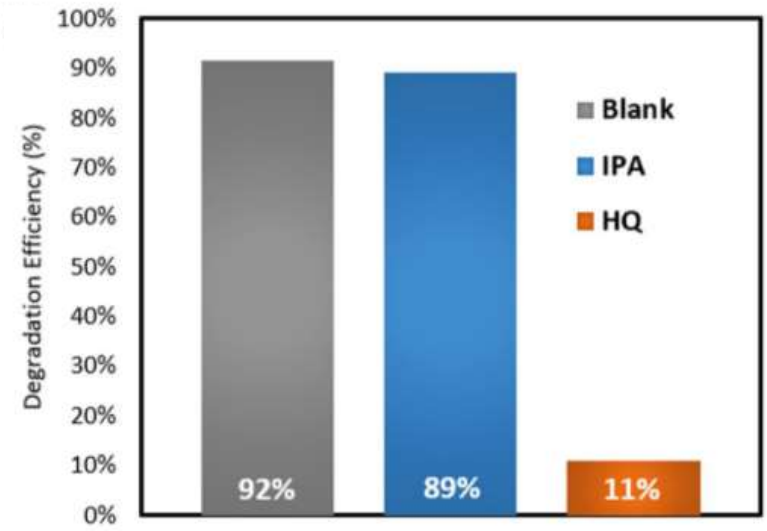

Figure 30: *Effect of ROS species on degradation performance.*

CdS – MoS_2 / CNTs nanocomposite

CdS – MoS_2 composites were prepared for hydrogen evolution reactions (HER) via photocatalytic water splitting. In addition, the composites were coupled with multiwalled CNTs as a carbonaceous support to enhance charge separation, increase visible light absorption and increase material surface area of the CdS – MoS_2 catalyst. The CNT and MoS_2 loadings were optimized during the synthesis procedure. Due to the large number of samples prepared, photocatalytic performance was evaluated to determine the optimal composites before materials characterization was conducted.

Photocatalytic hydrogen production

Optimization of carbon nanotubes (CNTs) content

Initially, a CdS – 3% MoS_2 sample (C3M) was coupled with varying amounts of functionalized CNTs to optimize the CNT concentration for HER. The composites with CNT loadings of 0%, 1%, 2%, 3%, 5% and 7% were labelled CM3C0, CM3C1, CM3C2, CM3C3, CM3C5 and CM3C7, respectively. HER performance was evaluated using 0.5 M lactic acid as a sacrificial reagent, with the results shown in Figure 31 below. The sample with 3% CNT loading exhibited the highest rate of H_2 evolution, indicating the optimal carbon loading for the CdS – MoS_2 composite. A CNT loading greater than 3% resulted in a drop in HER activity, which could be due to a decrease in active site density caused by increasing carbon surface area and thus reducing the number of photoactive sites available per unit area of illumination.

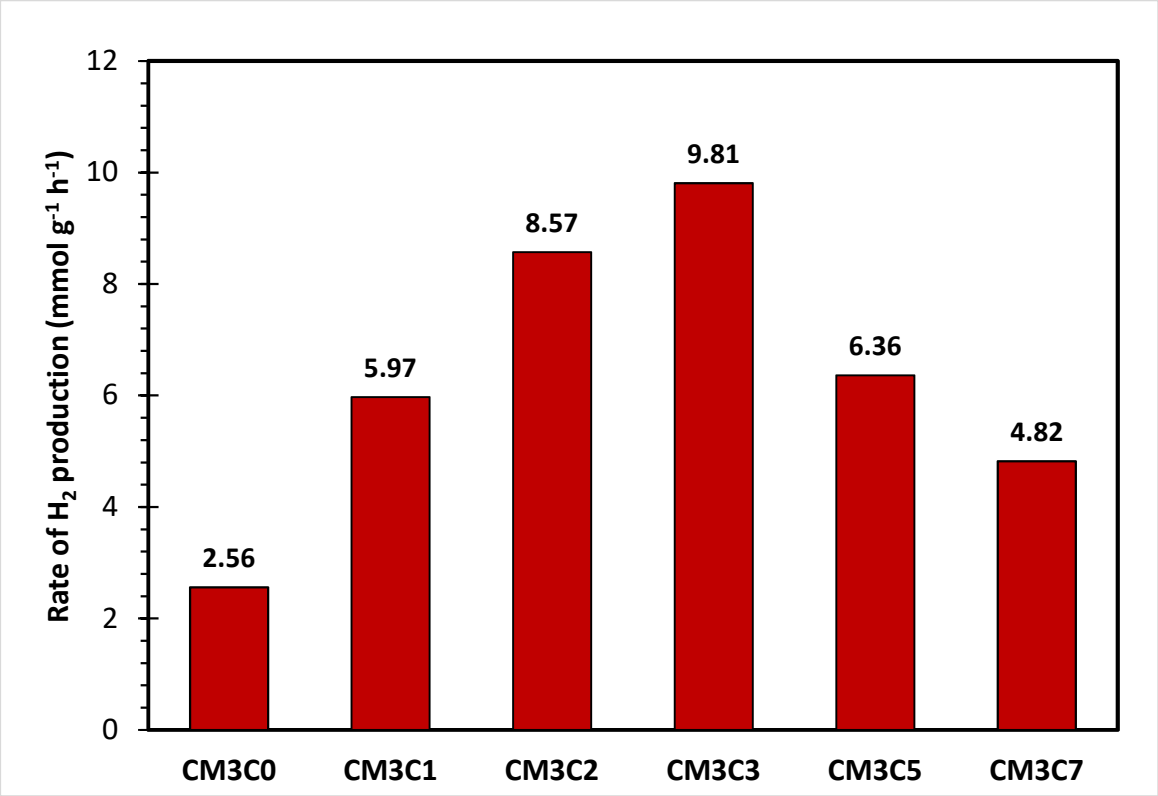

Figure 31: HER performance for CNT concentration optimization.

Optimization of MoS_2 content

After having optimized the carbon content, additional composites with a fixed CNT loading and varying MoS_2 concentration were synthesized and tested to determine the optimal MoS_2 content for hydrogen production. MoS_2 loadings of 0%, 3%, 5%, 7% and 10%, corresponding to samples CM0C3, CM3C3, CM5C3, CM7C3 and CM10C3 were prepared and tested, with HER performance results summarized in Figure 32 below.

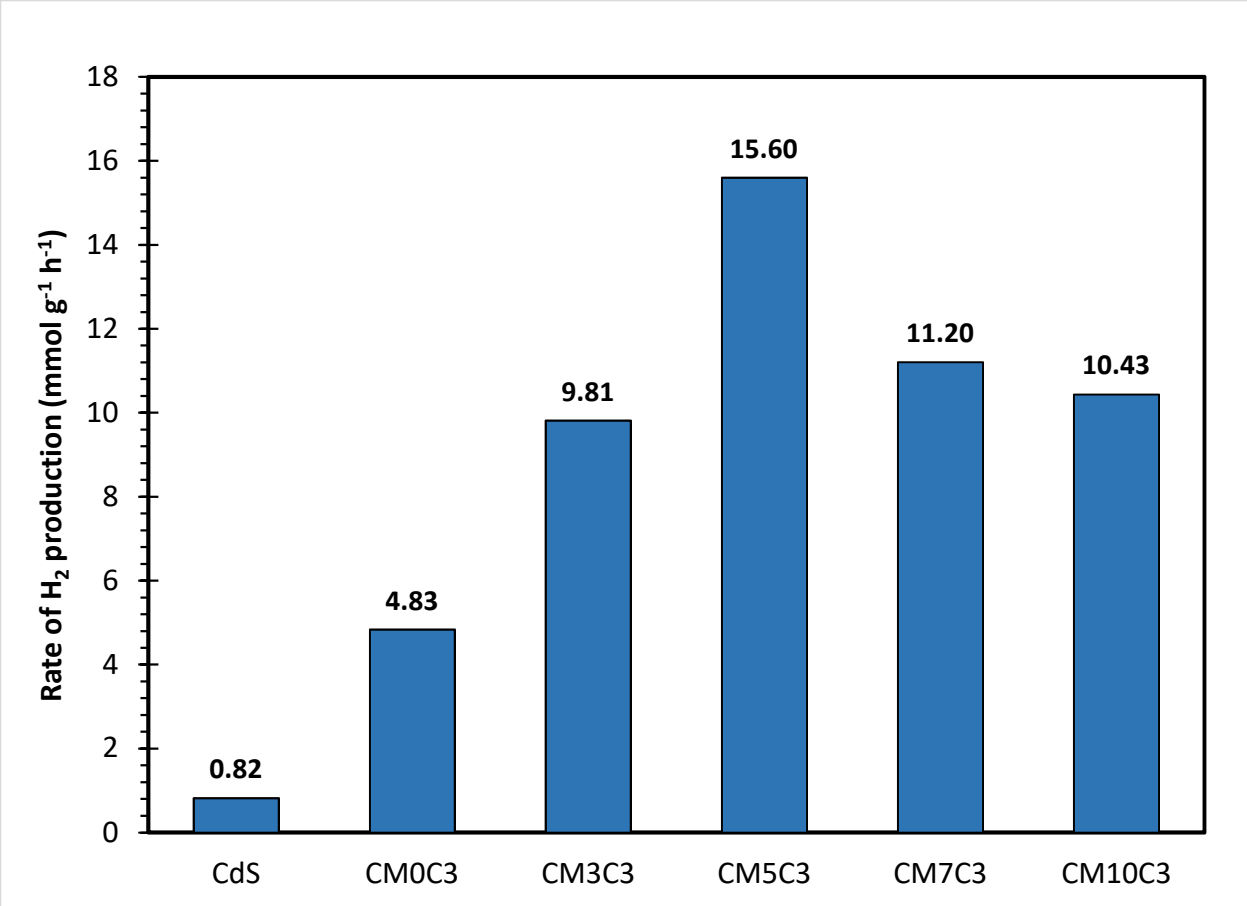

Figure 32: *HER performance for MoS_2 concentration optimization.*

A CdS – MoS_2 / CNT composite with a 5% MoS_2 and 3% CNT loading was found to be optimal for hydrogen evolution. Notably, the CM0C3 represents pure CdS coupled with CNTs, with the material achieving a rate of hydrogen production of approximately 4.83 mmol g^{-1} h^{-1}. Pure CdS nanorods synthesized and tested under identical operating conditions were found to achieve only 0.82 mmol g^{-1} h^{-1}, indicating an approximately 6-fold increase in HER performance when pure CdS nanorods are hydrothermally grown on the optimized amount of CNTs. For the optimized composite, CM5C3, a nearly 20-fold increase in photocatalytic activity for HER was observed when compared to pure CdS nanorods.

Stability Testing

Pure CdS and the CM5C3 sample were tested for stability and recyclability, with the results depicted in Figure 33. Cyclic HER performance experiments were conducted, with a total duration of 5 h each, to determine material stability for hydrogen production using lactic acid. For the CM5C3 composite, the rate of hydrogen production was unchanged during the first 3 cycles, with a 10% and 12% drop in cycles 3 and 4, and a total 22% drop in photocatalytic performance witnessed after the 20 h irradiation period. In contrast, the HER performance of pure CdS degraded rapidly, with a nearly 80% loss in activity after the same time-period. The slight reduction in activity of CM5C3 may be attributed to photo-corrosion of CdS and MoS_2. It could also be due to the partial detachment of the CNTs from the catalyst surface in the acidic solution. In addition, the catalyst deposition on the reactor surface and magnetic stirrer may also partially account for the apparent loss in photocatalytic performance for both materials.

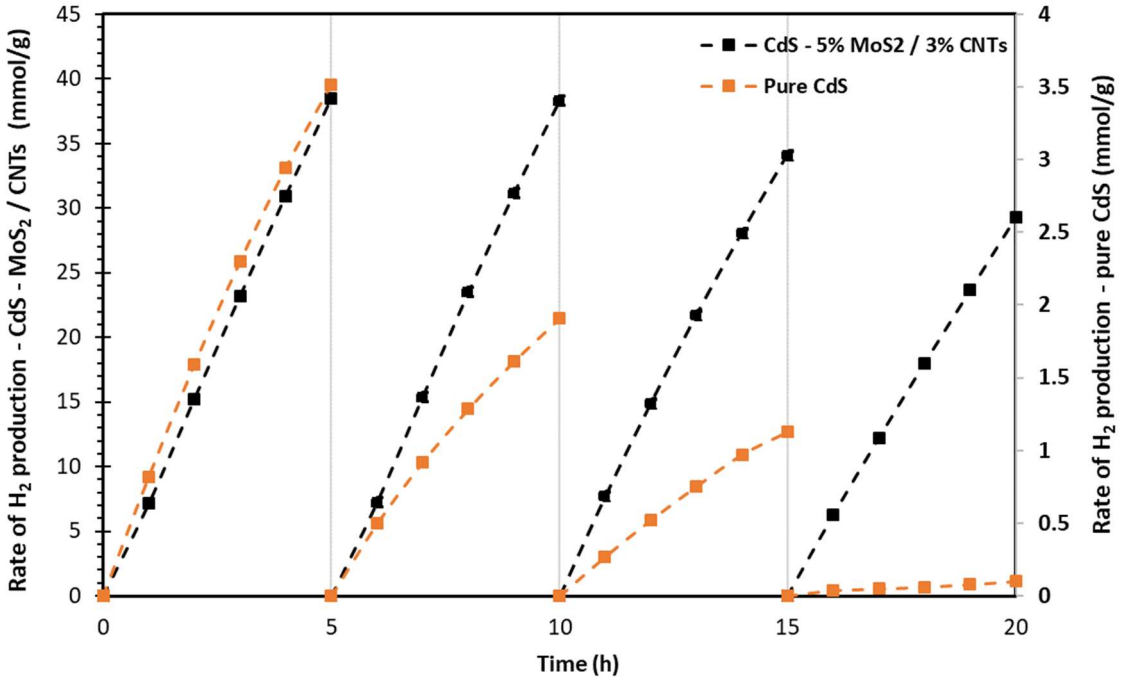

Figure 33: *Catalyst stability testing over 4 cyclic HER experiments.*

Apparent quantum yield (AQY)

The apparent quantum yield (AQY) is a measure of the catalyst efficiency to harvest solar energy for photocatalytic applications. It describes the ratio between the number of incident photons on the catalyst surface and number of photoexcited electrons reacted, with an efficiency approaching unity indicating a nearly perfect utilization of the incident photonic energy. The AQY is calculated using the equation shown below:[97]

$$AQY(\%) = \frac{number\ of\ reacted\ electrons}{number\ of\ incident\ photons} \times 100$$

Every molecule of hydrogen produced requires the consumption of 2 electrons, with the equation being modified to:

$$AQY(\%) = \frac{2 \times number\ of\ hydrogen\ molecules\ produced\ in\ time\ (t)}{number\ of\ incident\ photons\ in\ time\ (t)} \times 100$$

The number of incident photons can be calculated using the photonic energy and total energy of the incident light, as shown below:[97]

$$Number\ of\ incident\ photons = \frac{E_{total}}{E_{photo}} = \frac{PS\lambda_{inc}t}{hc}$$

Where P is the power density of the incident light (W m^{-2}), S is the incident surface area (m^2), λ_{inc} is the wavelength of the incident light (m), t is the irradiation time (s), h is Planck's constant (J/s) and c is the speed of light (m/s).

Table 8 below outlines the calculated AQY for the pure CdS, CM0C3 and CM5C3 samples, irradiated by 1 kW m^{-2} light intensity.

Table 8: *Apparent quantum yield calculations.*

Material	Catalyst amount (mg)	Irradiation Area (cm^2)	AQY (%)
CdS	25	38.5	0.29
CM0C3	25	38.5	1.89
CM5C3	25	38.5	7.34

While AQY absolute values are highly specific to the reactor design used and catalyst loading, relative comparisons between materials tested under the same conditions and in the same reactor provide meaningful insights. Compared to pure CdS, incorporation of the CNTs increases the material AQY by nearly 7 times, and the optimal CM5C3 catalyst exhibits a remarkable 25-fold AQY increase.

Material Characterization

Material morphology and composition

Figure 34 shows the SEM images taken of pure CdS nanorods and the sample that exhibited the highest photocatalytic performance for HER, CM5C3. Both samples are composed of nanorod shaped particles, with the MoS_2 content not affecting the surface morphology in any significant way. This could be in part due to the small concentration of MoS_2 involved. In addition, due to both materials possessing similar hexagonal lattice structures, the in-situ growth of MoS_2 with CdS resulted in MoS_2 embedding well within the crystal lattice of CdS, with no observed change to surface morphology. The CNTs are clearly seen in the CM5C3 composite, with the nanorods forming larger agglomerates in the pure CdS sample. The incorporation of CNTs resulted in smaller particle clusters, which is beneficial for photocatalytic applications by exposing a larger surface area for light absorption and active sites for catalytic reactions.

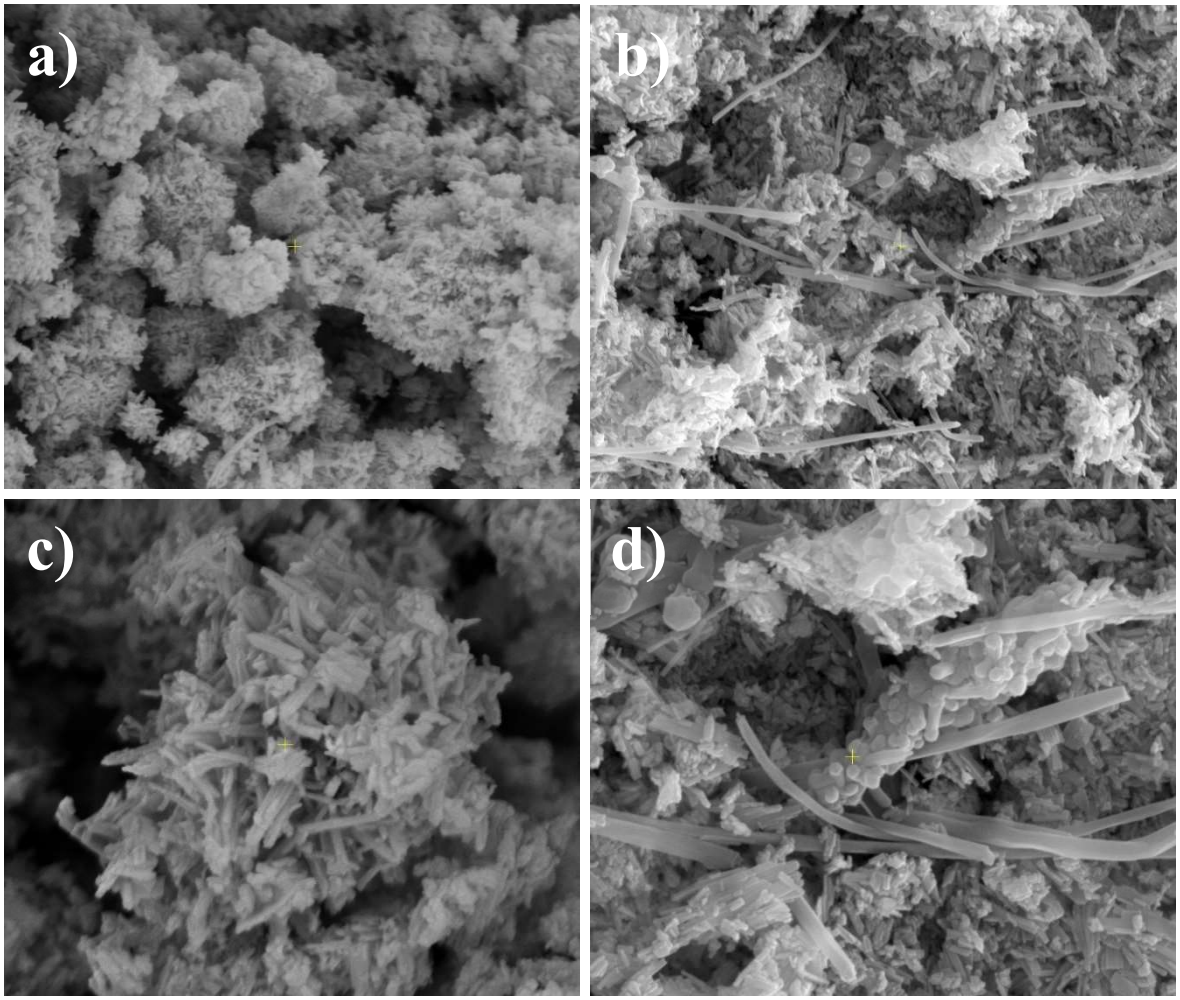

Figure 34: *SEM images of a), c) Synthesized CdS sample and b), d) Synthesized CM5C3 sample.*

HRTEM was used to determine facet growth and lattice spacing as well as identifying the nanorod growth pattern. Figure 35 depicts a single carbon nanotube with CdS – MoS_2 nanorod growth clearly shown along its length. With the synthesis procedure involving adequate time for the Cd and Mo precursors to adsorb on the CNTs prior to heat treatment, eventual growth of the photocatalytic material occurred on the CNT surface. This maximized contact with the carbonaceous support results in increased pathways for charge transfer from the CdS – MoS_2

composite along the carbon nanotube length and subsequently enhanced charge separation and improved photocatalytic activity.

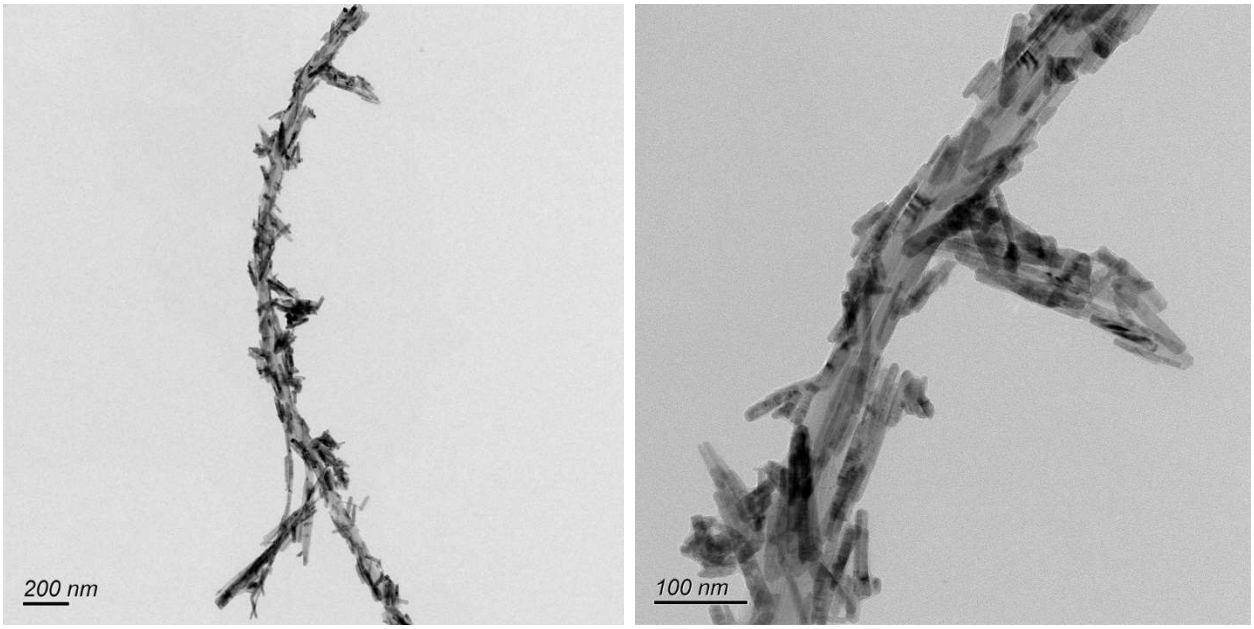

Figure 35: *HRTEM images of the CM5C3 sample.*

In addition, HRTEM elemental mapping was performed to analyze the composition of the CM5C3 sample, as shown in Figure 36. An even distribution of Cd, S, Mo and C can be seen, with Cd and S exhibiting the highest intensities due to the relative abundance of the elements, with Mo expectedly registering the least intense signal. A greater background noise is detected for both Mo and C signals due to the low composition and carbon tape used during analysis, respectively. However, both Mo and C signals are concentrated in the sample region, indicating the presence of both elements within the catalytic material in addition to Cd and S.

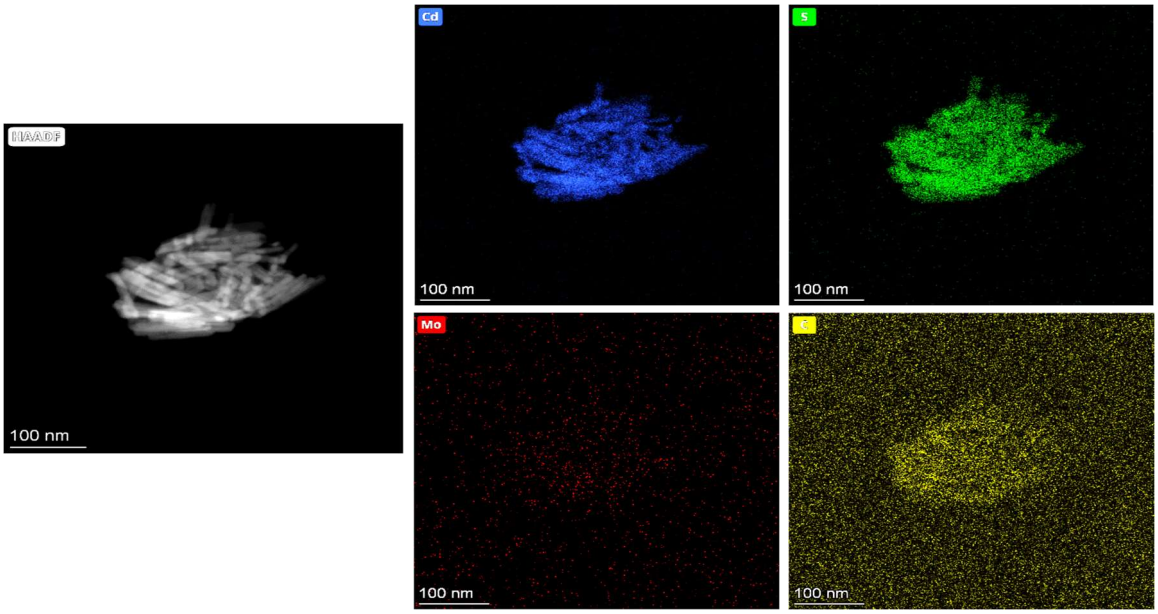

Figure 36: *HRTEM EDS elemental mapping.*

XPS analysis was employed to further probe the composition and chemical states of the surface elements in the fresh CM5C3 sample. The XPS survey scan shown in Figure 37 indicates the presence of Cd, S, Mo and C, with trace oxygen impurities present, with higher resolution C1s, Cd 3d, Mo 3d and S 2p spectra acquired to identify the chemical states of the involved species.

Upon peak deconvolution, the C1s spectra (Figure 38a) showed the presence of 3 distinct peaks at 284.8 eV (used as the reference for curve calibration), 286.2 eV and 287.0 eV, corresponding to the C = C (sp^3), C – O and C = O respectively.[98] The C – O alcohol and C = O carboxyl peaks are

representative of the successful acid functionalization of the MWCNTS prior to composite synthesis.[98]

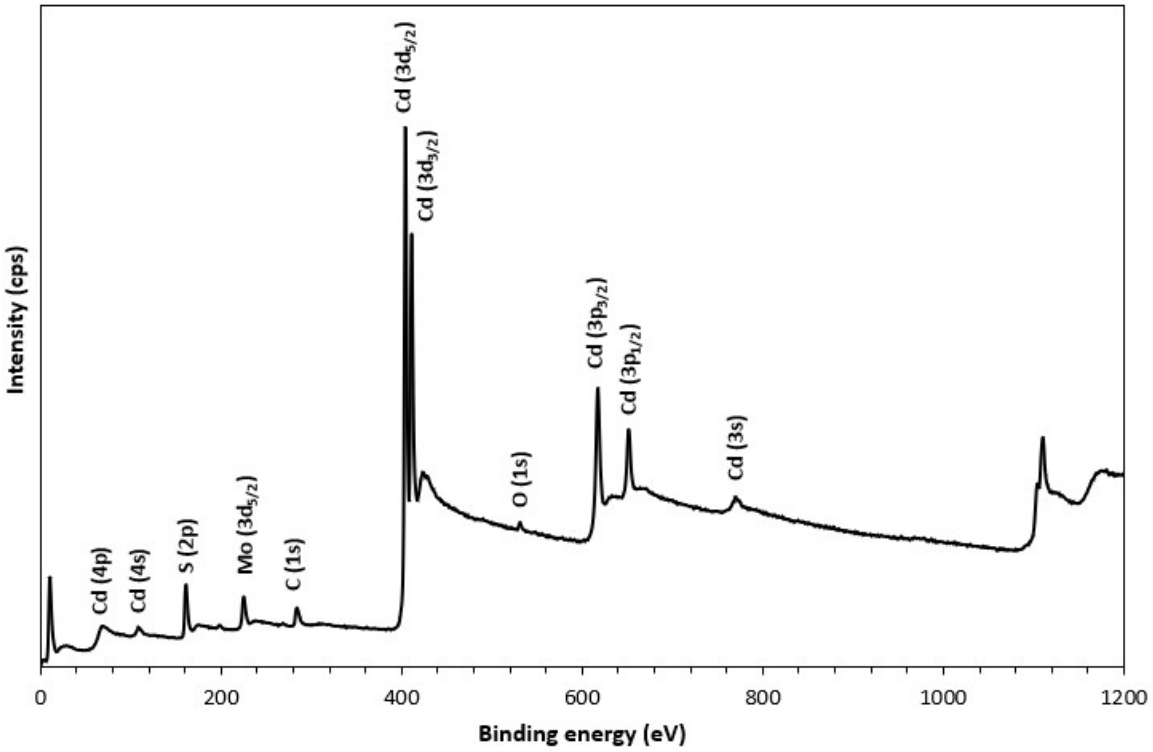

Figure 37: *XPS survey scan*

Analysis of the Cd 3d (Figure 38b) spectra yields the presence of 2 distinct peaks at 405.7 eV and 412.5 eV assigned to the binding energies of Cd ($3d_{5/2}$) and Cd ($3d_{3/2}$) respectively, corresponding to Cd^{2+} present in CdS.[99] In addition, 2 separate peaks at 406.4 eV and 413.4 eV were observed and can probably be attributed to the Cd – C bond formed between CdS and the CNTs during composite synthesis.[100] The Mo spectral region (Figure 38c) contains the S 2s and Mo 3d peaks at 226.6 eV and 229.0 eV. The peak at 229.0 eV is assigned to the binding energy of Mo ($3d_{5/2}$), corresponding to the Mo^{4+} oxidation state of the transition metal in MoS_2 and successful conversion of the Mo precursor (ammonium molybdate, which involves the Mo^{6+} oxidation

state).[101] Interestingly, the Mo spectra typically has an Mo ($3d_{3/2}$) peak positioned at 231.3 eV stemming from defect edge-Mo^{4+} positioned close to sulfur vacancies.[102] Absence of the Mo ($3d_{3/2}$) peak confirms the growth of MoS_2 within the lattice of the composite as opposed to near the edges.

Deconvolution of the S 2p spectra (Figure 38d) showed the presence of 2 major peaks at 162.0 eV and 162.9 eV assigned to S ($2p_{3/2}$) and S ($2p_{1/2}$) respectively.[101] In addition, a small peak at 165.3 eV was clearly visible that could be attributed to edge-site defects that result in the presence of coordinately unsaturated S_2^{2-} 2p orbitals, which can act as active sites for hydrogen evolution and boost photocatalytic performance.[101]

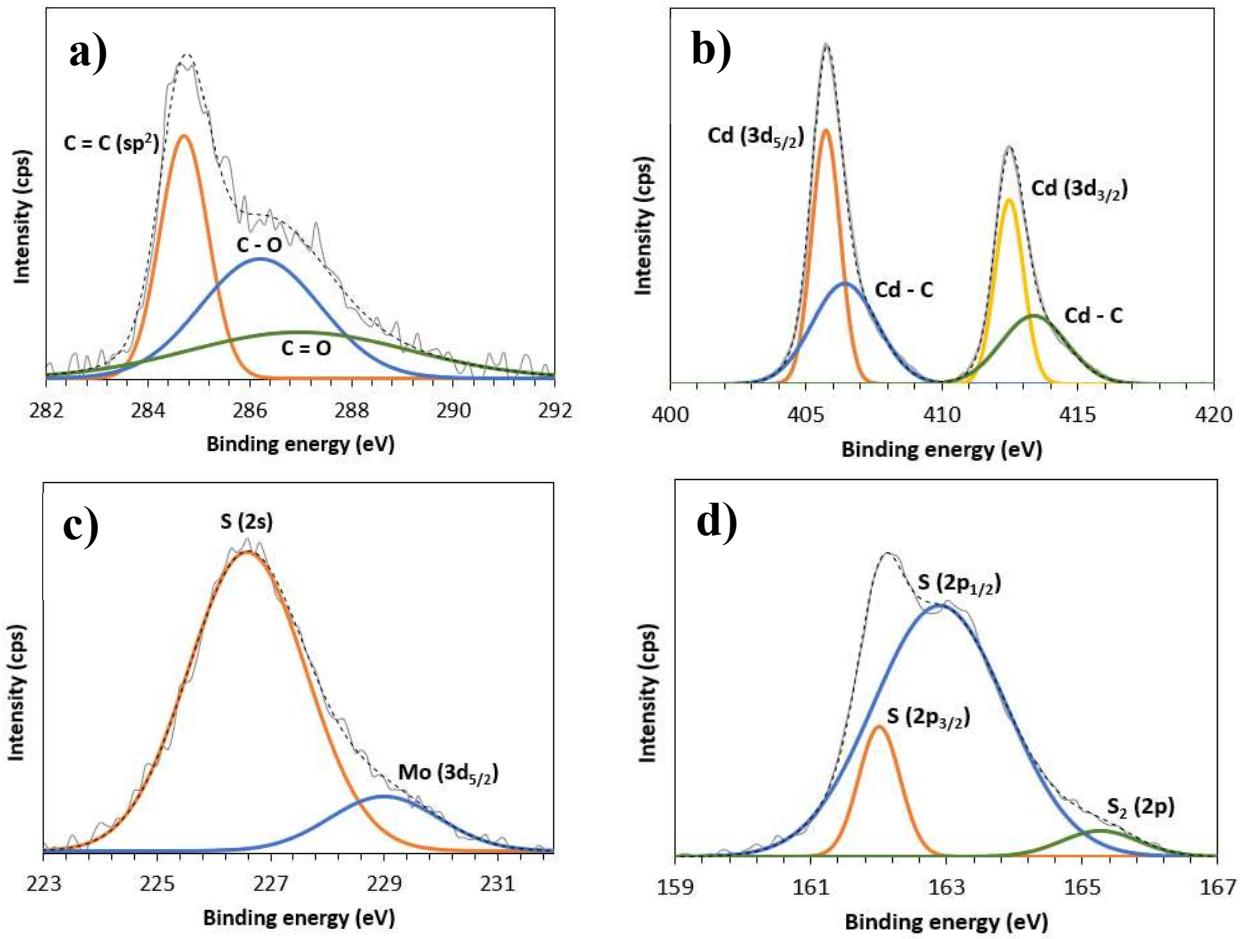

Figure 38: *XPS spectra of a) C 1s, b) Cd 3d, c) Mo 3d and d) S 2p.*

Material crystallinity and phases

Probing the material with higher resolution TEM imaging led to identification of three separate phases within the CM5C3 sample, namely cubic CdS, hexagonal CdS and MoS_2-2R. As shown in Figure 39 below, the material is predominantly composed of cubic CdS with d-spacing of 0.33 nm, corresponding to growth of the (111) phase[103], and hexagonal CdS with d-spacings of 0.36 nm and 0.34 nm consistent with the (100) and (002) facets.[104] In addition, the atomic arrangements of

MoS_2, with a d-spacing of 0.24 nm that is consistent with the (112) plane is also shown, with the honey-comb like structure typical of the 2H phase.[105] Figure 44b and 44c show additional spots in material CM5C3 depicting cubic and hexagonal CdS phases present respectively.

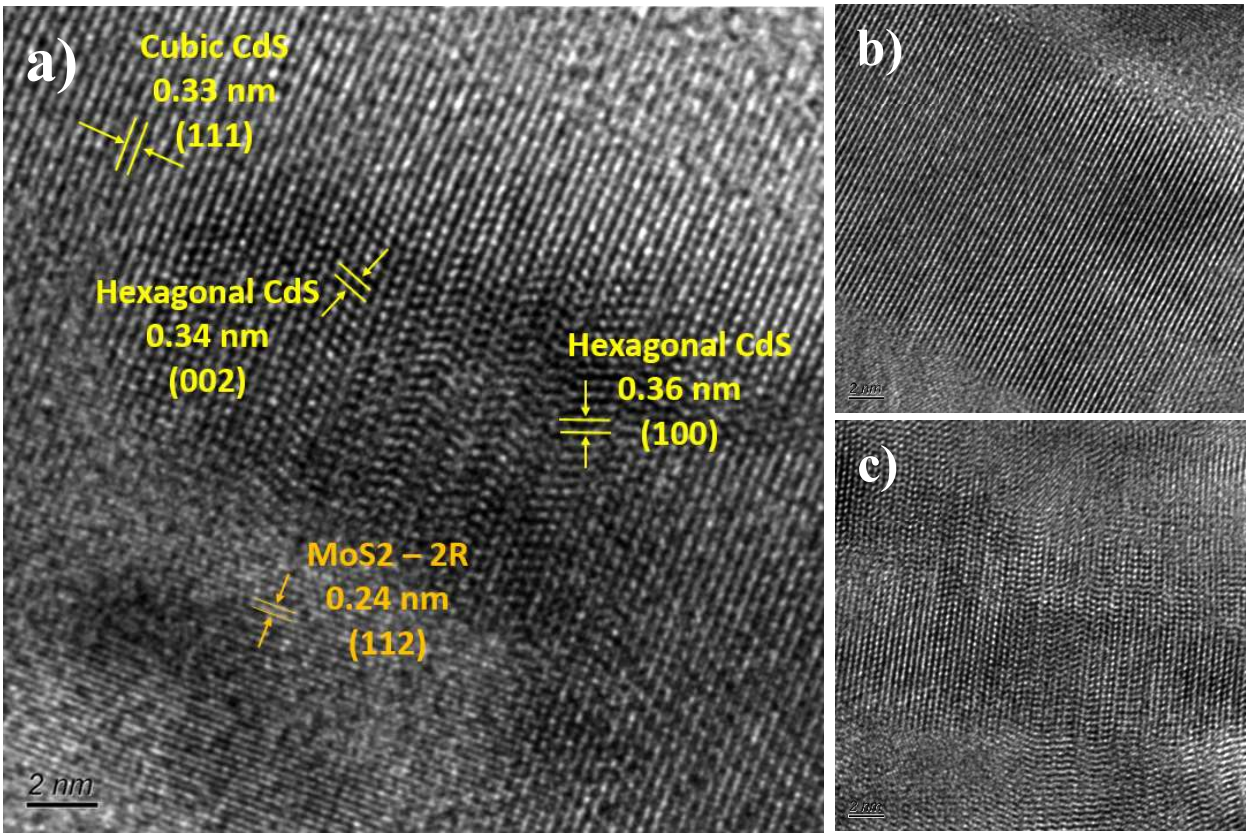

Figure 39: *HRTEM imaging of the CM5C3 sample showing a) Hexagonal CdS, cubic CdS and MoS_2 d-spacing, b) Cubic CdS growth, c) Hexagonal CdS growth.*

The crystalline structure of the prepared CM0C3 and CM5C3 composites was further investigated via XRD analysis as shown in Figure 40a. The results confirm the presence of a mixed-phase CdS, with the peaks showing hexagonal and cubic characteristics. The most intense peak appears at 26.505° corresponds to the hexagonal (002) and cubic (111) facets, and a mixed phase confirmed by the presence of shorter and broader peaks at 24.92 and 28.1 corresponding to the hexagonal

(100) and (101) facets, respectively. In the case of a fully hexagonal CdS structure, the H(100) and H(101) peaks are typically more intense with a much narrower full width at half maximum (FWHM), as shown in Figure 40b. However, a fully cubic CdS crystal structure does not register (100) and (101) peaks at all. No impurity peaks were present and interestingly, no peaks for MoS_2 were detected either, which can be attributed to the existence of MoS_2 within the bulk of the material in low concentration.[106]

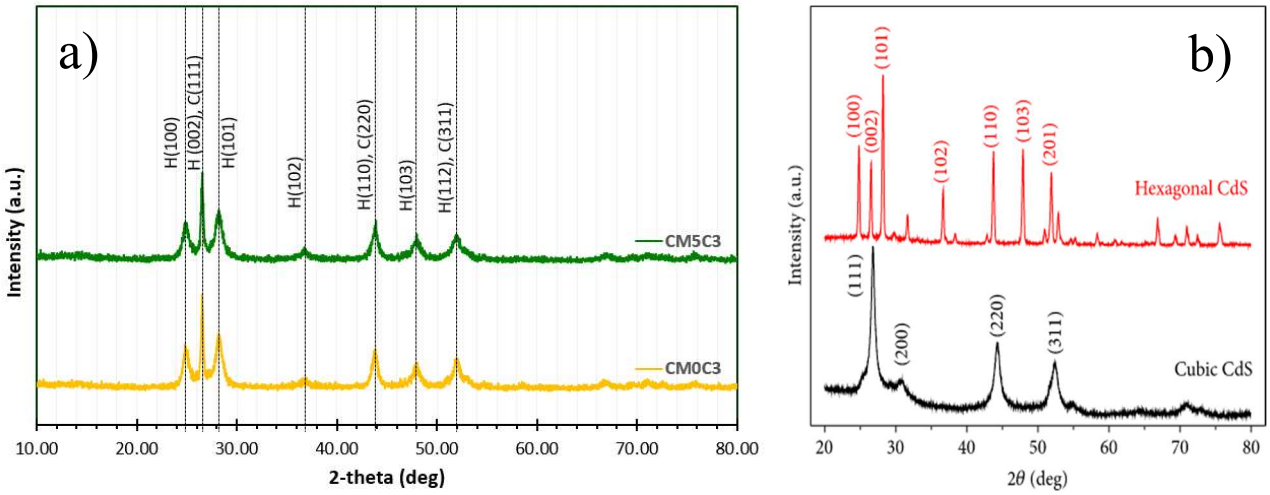

Figure 40*: a) XRD spectra of CM0C3 and CM5C3, b) Known XRD spectra for hexagonal and cubic CdS.*[65]

Table 9 summarizes the obtained XRD peak positions and their corresponding hexagonal or overlapping hexagonal and cubic facets (if any).

Table 9: *XRD peak positions and corresponding phases.*

Peak position (°)	Hexagonal facet	Cubic facet
24.92	(100)	-
26.505	(002)	(111)
28.10	(101)	-
36.58	(102)	-
43.8	(110)	(220)
47.813	(103)	-
51.97	(112)	(311)

Optical band gap and visible light absorption

Solid state UV-Vis analysis was conducted across 400 – 800 nm wavelengths to determine the effect of the CNT and MoS_2 doping on material optical properties and visible light absorption, as shown in Figure 41. Incorporation of CNTs significantly improved light absorption of CdS, particularly in the longer wavelength visible light region. CNTs possess excellent visible light absorption, as evident from the nearly 60% increase in light absorption for the CM0C3 sample compared to pure CdS. MoS_2 also possesses a smaller band gap and better visible light absorption when compared to CdS, with the MoS_2 doping showing an enhancement of the CM5C3 sample's visible light absorption in the range of 500 – 800 nm.

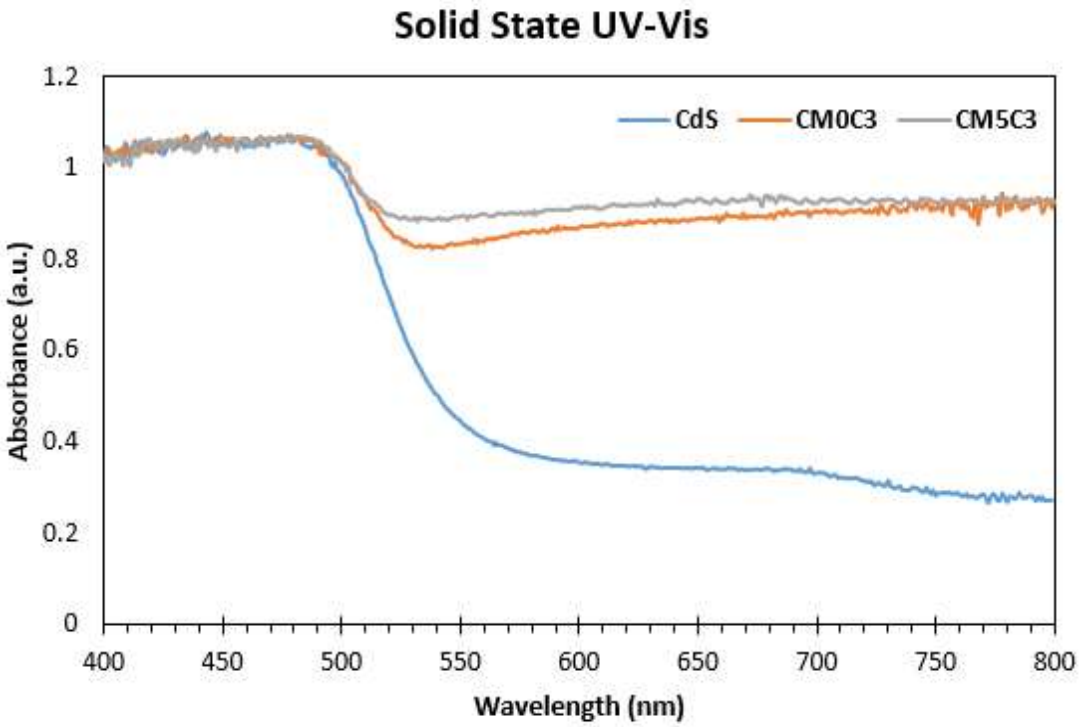

Figure 41: *Solid state UV-Vis analysis and absorbance data.*

Carbon-doping of CdS results in a blue shift of the absorption edge from 580 nm for the CM0C0 sample to 530 nm for the CM0C3 sample. MoS_2-doping also produces the same blue-shift effect of the absorption edge with the CM5C3 sample exhibiting an absorption edge of 520 nm. This blue-shift can be attributed to increased quantum confinement effects with a decreasing crystallite size. The Scherrer and Williamson-Hall approximations were used to calculate the crystallite size of the CM0C0, CM0C3 and CM5C3 samples from the XRD spectra, shown in Table 10 below, indicating the decreasing particle size with increased molybdenum doping.

Table 10: *Crystallite size calculations for prepared samples.*

Material	Average crystallite size (nm)	
	Scherrer	**Williamson-Hall**
Pure CdS	19.24	19.22
CM0C3	19.94	19.92
CM5C3	18.35	18.33

Both methods show excellent agreement for the average crystallite size, indicating that CNT and MoS_2 doping does not induce any significant lattice strains within the material structure. It is worth noting that the addition of CNTs resulted in a slight increase in crystallite size, perhaps owing to the greater dispersion of the involved precursors allowing the individual crystals to grow more unhindered. Contrarily, the incorporation of MoS_2 decreased the average crystallite size, as pure MoS_2 generally possesses a small crystallite size of about 10 nm, with a resultant blue-shift in the absorption band edge as confirmed by solid state UV-Vis analysis in Figure 46.[107]

Despite the blue shift in the adsorption edge, the overall improvement in the absorption of visible light in the 500 – 800 nm region suppresses any negative effect from the apparent blue shift. In addition, the effect of the crystallite size on electron-hole pair recombination is insignificant for crystallite sizes greater than 15 nm[89], hence, the slightly reduced crystallite size for the MoS_2 doped sample is not expected to have a detrimental impact on photocatalytic activity.

The optical band gap of the samples was calculated based on the solid-state UV-Vis data using Tauc plots. The Tauc method specifies that the energy-dependent absorption coefficient is expressed by the equation below:[108]

$$(\alpha h\nu)^{\frac{1}{\gamma}} = B(h\nu - E_g)$$

Where α is the absorption coefficient, h is planck's constant, v is the photonic frequency, E_g is the material band gap, B is a constant, and γ is a factor with a value of ½ or 2 depending on whether the semiconductor possesses a direct or indirect band gap respectively. CdS and MoS_2 are known to have direct band gaps, so the γ factor is presumed to have a value of ½.[109] Figure 42 shows Tauc plot of $(\alpha h\nu)^{\frac{1}{\gamma}}$ vs hv ,which indicate a steep linear increase of light absorption with increasing energy. Extrapolating this linear region to the x-axis results in the estimation of the optical band gap energy of the material.[108] Pure CdS exhibited a band gap energy of 2.3 eV, in close agreement with widely reported CdS data in literature.[110]

The addition of CNTs in the CM0C3 sample resulted in a narrower band gap of 2.22 eV, with the increased visible light absorption due to the carbonaceous support narrowing the effective optical band gap energy. Additionally, MoS_2 generally possesses a much smaller band gap of 0.9 and 1.6 eV for the bulk and monolayer, respectively[111]. Therefore, incorporating MoS_2 in the CdS composite (CM5C3) resulted in additional narrowing of the composite band gap to 2.18 eV, with the relatively smaller effect related to the low concentration of MoS_2 involved in the material.

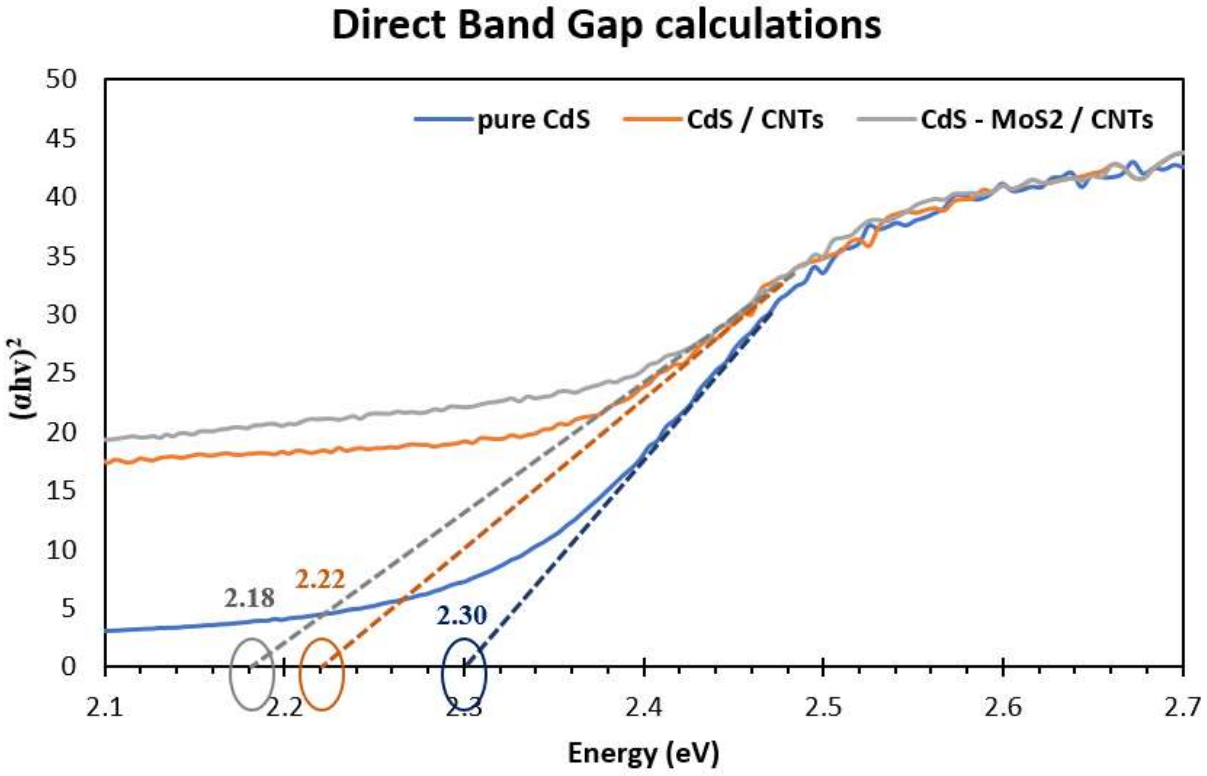

Figure 42: *Band gap estimation using Tauc plots.*

Mechanism of photocatalytic hydrogen production

As mentioned earlier, MoS_2 and CdS are generally characterized as p-type and n-type semiconductors, respectively. P-type semiconductors involve positively charged holes (absence of an electron) as the major charge carriers, while n-type semiconductors involve negatively charged electrons as the major charge carriers. Before coming into contact, the CB band edge of CdS is slightly more negative than the CB for MoS_2, and the VB band edge slightly more positive than that for MoS_2, as shown in Figure 43, with the Fermi energy levels of both semiconductors within the material band gap. The Fermi level refers to the highest energy level occupied by electrons, and is a measure of energy required to add an electron to the material.[112] P-type semiconductors

have the Fermi level located closer to the valence band, and n-type semiconductors have the Fermi level closer to the conduction band.[112]

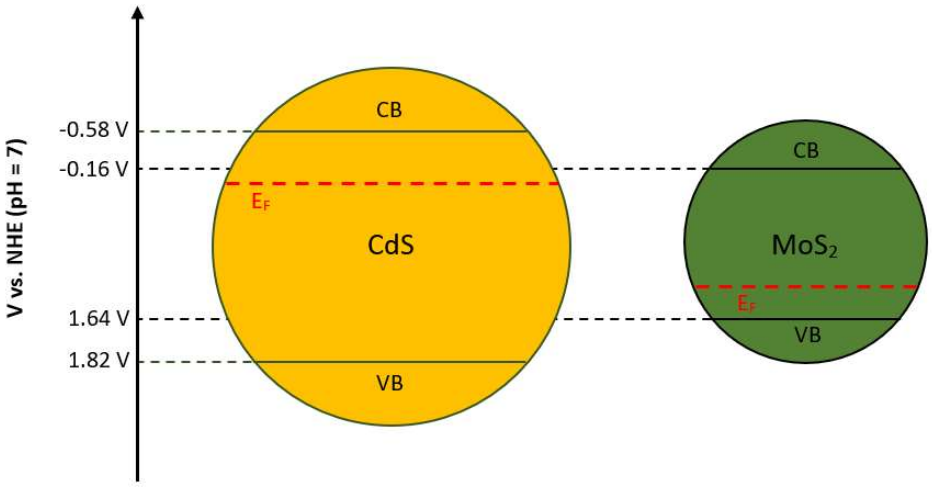

Figure 43: *Semiconductor Fermi energy levels.*

When p-type and n-type semiconductors come into contact, electrons can flow from n-type semiconductor, decreasing its Fermi level, to the p-type, increasing its Fermi level, until both Fermi levels align and the material achieves equilibrium. This is associated with a simultaneous shifting of the CB and VB edges due to the Fermi alignment.[112] Following the same principle, when n-type CdS and p-type MoS_2 are combined to form a p-n junction, the resulting Fermi alignment causes the negative shift of the MoS_2 CB and VB edges, making the CB of MoS_2 more negative than the CB for CdS, as shown in Figure 44. Due to the primitive accumulation of the oppositely charged carriers in the p-type and n-type semiconductors, an inner electric field is established on the junction interface between CdS and MoS_2. Upon illumination, the negatively charged photoexcited electrons migrate from the CB of the p-type MoS_2 to the CB of n-type CdS.[113]

The positively charged holes transfer from the VB of CdS to the VB of MoS_2. Contact with a carbonaceous support like carbon nanotubes allows the photoexcited electrons additional transmission pathways away from the catalyst surface along the length of the tube, where they can reduce H^+ ions to produce H_2. The formation of a p-n junction and subsequent inner electric field, in addition to contact with the CNTS, results in significantly increased charge separation and suppressed electron-hole recombination, with the positively charged holes in the VB of MoS_2 oxidizing the sacrificial reagent (lactic acid) to complete the photocatalytic cycle.[76]

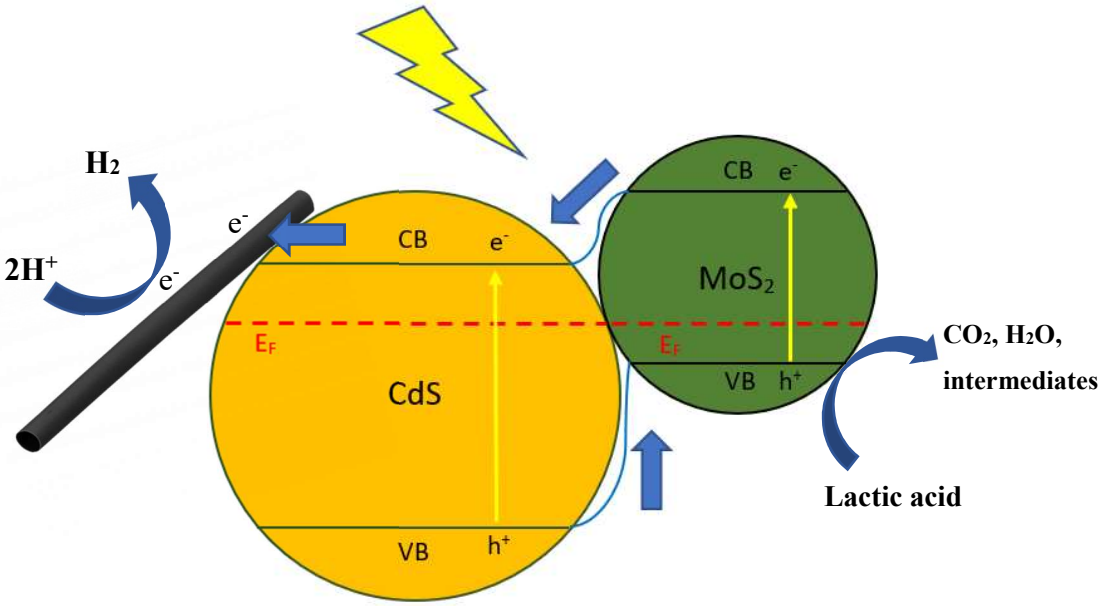

Figure 44: *Fermi alignment and photocatalytic mechanism.*

The one-pot synthesis technique ensures the MoS_2 content is well dispersed throughout the CdS lattice structure, ensuring a maximization of the CdS – MoS_2 p-n junction formation. In addition, coupled with CNTs that results in increased visible light absorption, increased dispersion, larger surface area and a reduced optical band gap, the CdS – MoS_2 / CNTs composite is found to possess significantly superior photocatalytic HER performance compared to pure CdS.

CHAPTER V – CONCLUSIONS AND RECOMMENDATIONS

With the advent of black TiO_2 via the formation of surface defects in the form of oxygen vacancies, significant photocatalytic enhancements have been exhibited when compared to its pristine counterpart. However, the same technique had not been previously applied to other metal oxide semiconductors. Therefore, the facile reduction technique was performed on V_2O_5, a promising candidate for photocatalytic organic contaminant degradation. Pristine V_2O_5, which possesses a narrower band gap than TiO_2, suffers from rapid electron-hole pair recombination with hindered photocatalytic performance. However, with a larger lattice oxygen density than TiO_2 and a higher oxidation state of the transition metal involved, black V_2O_5 has shown to outperform its TiO_2 predecessor.

Black V_2O_5, "bV_2O_5" was synthesized by employing a facile reduction procedure using $NaBH_4$. It is hypothesized that the reducing environment created by the decomposition of $NaBH_4$ and subsequent formation of H_2, results in the removal of oxygen atoms from the lattice structure of V_2O_5 via reaction with the formed H_2. This results in the creation of surface defects in the form of oxygen vacancies. These oxygen vacancies induce a significant negative charge on the bV_2O_5 surface, by providing OH^- ion binding sites and increasing the hydroxyl anion concentration around the material surface. This can significantly improve photocatalytic activity as these oxygen vacancies can act as electron trap sites, providing additional energy levels for the photoexcited electrons and improving charge separation. In addition, these oxygen vacancies have been found to alter the degradation mechanism, by facilitating the formation of anionic superoxide radicals, which are strong oxidizing agents and were found to be the primary species involved in the degradation of organic contaminants.

Black V_2O_5 was found to possess a remarkable degradation efficiency, achieving nearly 93% degradation of methylene blue (MB) after 1 hour of irradiation, compared to nearly no degradation achieved by pV_2O_5 during the same time-period. Degradation kinetics was improved by 58-fold, and the photocatalytic efficiency was found to be much higher than black TiO_2, which achieved only 82% degradation of MB in 1 hour, exhibiting slower kinetics than its vanadium counterpart.

With oxygen vacancies predominantly present only on the V_2O_5 surface, the resultant catalyst assumes the form of a nanocomposite, with black V_2O_5 present on the surface and pristine V_2O_5 hetero-junctioned in the bulk. This creation of a junction interface between both phases allows for the creation of a Z-scheme mechanism, whereby the photoexcited electrons from the CB of pV_2O_5 can migrate to the VB of bV_2O_5. These electrons then require less energy for photoexcitation as the induced oxygen vacancies result in the narrowing of the optical band gap of bV_2O_5 (from 2.3 eV for pV_2O_5 to 1.1 eV for bV_2O_5). In addition, with the resulting bV_2O_5 being much darker than pV_2O_5, visible light absorption is significantly increased, as confirmed by UV-Vis measurements, which further improved the photocatalytic activity. In addition, the presence of the V^{5+} and V^{3+} oxidation states introduce additional electron trap states and further suppress electron-hole pair recombination, boosting degradation performance.

For photocatalytic water splitting reactions, a thermodynamic limitation placed on band edges limits the number of photocatalysts capable of hydrogen production from water. The conduction band edge is required to be more negative than the H^+/H_2 reduction potential (-0.41 V) and the valence band edge is required to be more positive then the O_2/H_2O redox potential (0.82 V). Cadmium sulfide, CdS, is a widely studied photocatalyst for hydrogen production due to its favorable band edge positions and narrow band gap. However, it too suffers from rapid electron-hole recombination and induced photo-corrosion under irradiation. In this work, the photocatalytic

performance of CdS has been enhanced via the one-step coupling with MoS_2, a cocatalyst having recently attracted a considerable attention due to its tunable optical properties, unique layered structure, excellent physiochemical and electrical properties, and edge-controlled catalytic activity. P-type MoS_2 has been known to form p-n junctions with n-type CdS, with the resulting inner electric field inducing strong charge separation and boosting photocatalytic activity.

Most previous studies focused on a two-step preparation technique involving sequential CdS and MoS_2 syntheses. However, this work focuses on a one-pot synthesis of CdS – MoS_2 composites coupled with CNTs, to maximize the number of p-n junctions and enhance photocatalytic activity by increasing charge separation. The CdS – MoS_2 / CNTs composites were hydrothermally prepared using ethylenediamine as the solvent. The optimal CNT and MoS_2 concentrations were found to be 3% and 5% respectively. The successful synthesis of the composite was validated by TEM and XPS analysis. TEM images have shown the presence of cubic CdS, hexagonal CdS and MoS_2 within the lattice structure. Deconvoluted Cd 3d peaks obtained via XPS showed peak broadening attributed to the Cd – C bond formation during synthesis. Mo 3d high resolution peaks also showed the presence of Mo^{4+}, which has the same valence state of Mo in MoS_2.

XRD analysis confirmed the presence of cubic and hexagonal CdS in the material crystal structure. Scherrer and Williamson-Hall approximations were used to determine the effect of doping on the crystallite size of the composites. The addition of CNTs was found to increase crystallite size, while MoS_2 doping had an opposite effect. The incorporation of both CNTs and MoS_2 significantly improved visible light absorption in the range of 500 – 800 nm, and band gap narrowing from 2.3 eV for pure CdS to 2.22 eV and 2.18 eV for CM0C3 and CM5C3, respectively.

The coupling of CNTs was shown to have a prominent effect on HER performance by increasing the rate of hydrogen evolution nearly 7 times when compared to pure CdS nanorods. The CdS /

3% CNT composite (labelled CM0C3) achieved a hydrogen production rate of 4.83 mmol g^{-1} h^{-1}. MoS_2 doping further enhanced the hydrogen production rate to 15.6 mmol g^{-1} h^{-1} for an optimal loading of 5% (CM5C3). Furthermore, cyclic HER experiments verified the increased stability and recyclability of the optimal CM5C3 sample when compared to pure CdS nanorods, with the doped material only losing 20% efficiency after 20 hours of irradiation compared to a nearly 80% loss in activity of pure CdS after the same time-period.

For future work, it may be recommended to study the effect of CdS phase on the material photoactivity. It is widely known that hexagonal CdS is more photoactive than cubic CdS, however, the interface between both phases can serve as charge transfer junction which can enhance charge separation. It remains to be seen whether a purely hexagonal CdS exhibits higher HER performance when compared to the mixed phase for this specific composite. CdS based composites suffer from deposition to the bottom surface of the reactor over extended time periods. To achieve maximum yield of hydrogen, the development of counter measures is imperative, with the use of suitable surfactants and peptizing agents being potential candidates for increasing photocatalyst dispersion. Optimizing reactor design to ensure proper mixing without loss of catalytic material due to deposition on reactor walls and surface is recommended, in addition to developing suitable designs to maximize light penetration and illumination of the photocatalysts below the water surface.

For photocatalytic contaminant degradation, the effect of other water constituents on degradation efficiency should be evaluated. Some ionic compounds are known to improve photocatalytic efficiency, while others have detrimental impacts. Wastewater systems generally have a significant quantity of various dissolved substances, which can lead to catalyst deactivation or poisoning. Evaluation of such effects is of paramount importance before this technique can be used

commercially for wastewater treatment and hydrogen production. Additionally, it would be ideal if both hydrogen production and contaminant degradation can occur simultaneously. Several organic species having the potential to act as sacrificial reagents in the hydrogen production cycle. The use of contaminants in need of oxidative degradation as electron donors for hydrogen production can be the way to couple the two systems for efficient, cost-effective, and simultaneous solar-driven wastewater treatment and clean hydrogen production.

REFERENCES

1. Dudley B. BP statistical review of world energy. *BP Statistical Review, London, UK, accessed Aug.* 2018;6:2018.
2. Berner RA. The long-term carbon cycle, fossil fuels and atmospheric composition. *Nature.* 2003;426(6964):323-326.
3. Ritchie H, Roser M. Fossil fuels. *Our World in Data.* 2017.
4. Hasanuzzaman M, Zubir US, Ilham NI, Seng Che H. Global electricity demand, generation, grid system, and renewable energy polices: a review. *Wiley Interdisciplinary Reviews: Energy and Environment.* 2017;6(3):e222.
5. O'Dwyer J, Dowling A, Adley C. The impact of climate change on the incidence of infectious waterborne disease. *Urban Water Reuse Handbook; CRC Press: Boca Raton, FL, USA.* 2016:1053-1062.
6. Xu Y, Ramanathan V. Well below 2 C: Mitigation strategies for avoiding dangerous to catastrophic climate changes. *Proceedings of the National Academy of Sciences.* 2017;114(39):10315-10323.
7. Ramseur JL. US Carbon Dioxide Emissions Trends and Projections: Role of the Clean Power Plan and Other Factors. *US Congressional Research Service.* 2017.
8. Züttel A, Remhof A, Borgschulte A, Friedrichs O. Hydrogen: the future energy carrier. *Philosophical Transactions of the Royal Society A: Mathematical, Physical and Engineering Sciences.* 2010;368(1923):3329-3342.
9. Trimm D. The steam reforming of natural gas: problems and some solutions. *Studies in Surface Science and Catalysis.* Vol 36: Elsevier; 1988:39-50.

10. Nowotny J, Sorrell C, Sheppard L, Bak T. Solar-hydrogen: environmentally safe fuel for the future. *International journal of hydrogen energy.* 2005;30(5):521-544.

11. Torres-Pinto A, Sampaio MJ, Silva CG, Faria JL, MT Silva A. Recent strategies for hydrogen peroxide production by metal-free carbon nitride photocatalysts. *Catalysts.* 2019;9(12):990.

12. Prasse C, Stalter D, Schulte-Oehlmann U, Oehlmann J, Ternes TA. Spoilt for choice: a critical review on the chemical and biological assessment of current wastewater treatment technologies. *Water research.* 2015;87:237-270.

13. Han F, Kambala VSR, Srinivasan M, Rajarathnam D, Naidu R. Tailored titanium dioxide photocatalysts for the degradation of organic dyes in wastewater treatment: a review. *Applied Catalysis A: General.* 2009;359(1-2):25-40.

14. Darwish M. Qatar water problem and solar desalination. *Desalination and Water Treatment.* 2014;52(7-9):1250-1262.

15. Abdel-Fatah MA. Nanofiltration systems and applications in wastewater treatment. *Ain Shams Engineering Journal.* 2018;9(4):3077-3092.

16. Rout PR, Zhang TC, Bhunia P, Surampalli RY. Treatment technologies for emerging contaminants in wastewater treatment plants: A review. *Science of The Total Environment.* 2021;753:141990.

17. Laursen S, Poudyal S. Photo-and Electro-Catalysis: CO2 Mitigation Technologies. *Novel Materials for Carbon Dioxide Mitigation Technology*: Elsevier; 2015:233-268.

18. Meng A, Zhang L, Cheng B, Yu J. Dual cocatalysts in TiO2 photocatalysis. *Advanced Materials.* 2019;31(30):1807660.

19. Serpone N. Is the band gap of pristine TiO2 narrowed by anion-and cation-doping of titanium dioxide in second-generation photocatalysts? *The Journal of Physical Chemistry B.* 2006;110(48):24287-24293.

20. Chedup S, Subba B, Dorji S, Perera TDP, Rajaram A, Jayakody DNK. Visible light energy harvesting in modern communication systems. Paper presented at: Proc. EECCMC2015.

21. Chen X, Liu L, Peter YY, Mao SS. Increasing solar absorption for photocatalysis with black hydrogenated titanium dioxide nanocrystals. *Science.* 2011;331(6018):746-750.

22. Teixeira IF, Quiroz J, Homsi MS, Camargo PH. An overview of the photocatalytic H2 evolution by semiconductor-based materials for nonspecialists. *Journal of the Brazilian Chemical Society.* 2020;31:211-229.

23. Han B, Hu YH. MoS2 as a co-catalyst for photocatalytic hydrogen production from water. *Energy Science & Engineering.* 2016;4(5):285-304.

24. Ning X, Lu G. Photocorrosion inhibition of CdS-based catalysts for photocatalytic overall water splitting. *Nanoscale.* 2020;12(3):1213-1223.

25. Low J, Yu J, Jaroniec M, Wageh S, Al-Ghamdi AA. Heterojunction photocatalysts. *Advanced materials.* 2017;29(20):1601694.

26. by fuel type-Exajoules C, Emissions CD. bp Statistical Review of World Energy June 2020. 2006.

27. Abas N, Kalair A, Khan N. Review of fossil fuels and future energy technologies. *Futures.* 2015;69:31-49.

28. Shaheen SA, Lipman TE. Reducing greenhouse emissions and fuel consumption: Sustainable approaches for surface transportation. *IATSS research.* 2007;31(1):6-20.

29. Höök M, Tang X. Depletion of fossil fuels and anthropogenic climate change—A review. *Energy policy.* 2013;52:797-809.

30. Edwards PP, Kuznetsov VL, David WI, Brandon NP. Hydrogen and fuel cells: towards a sustainable energy future. *Energy policy.* 2008;36(12):4356-4362.

31. Iulianelli A, Liguori S, Wilcox J, Basile A. Advances on methane steam reforming to produce hydrogen through membrane reactors technology: A review. *Catalysis Reviews.* 2016;58(1):1-35.

32. Sengodan S, Lan R, Humphreys J, et al. Advances in reforming and partial oxidation of hydrocarbons for hydrogen production and fuel cell applications. *Renewable and Sustainable Energy Reviews.* 2018;82:761-780.

33. Rowshanzamir S, Eikani M. Autothermal reforming of methane to synthesis gas: Modeling and simulation. *International journal of hydrogen energy.* 2009;34(3):1292-1300.

34. Kalamaras CM, Efstathiou AM. Hydrogen production technologies: current state and future developments. Paper presented at: Conference papers in science2013.

35. Stiegel GJ, Ramezan M. Hydrogen from coal gasification: An economical pathway to a sustainable energy future. *International journal of coal geology.* 2006;65(3-4):173-190.

36. Muradov N, Veziroğlu T. From hydrocarbon to hydrogen–carbon to hydrogen economy. *International journal of hydrogen energy.* 2005;30(3):225-237.

37. Gedda G, Kolli Balakrishna RUD, Shah KJ. Introduction to Conventional Wastewater Treatment Technologies: Limitations and Recent Advances. *Advances in Wastewater Treatment I.* 2021;91:1-36.

38. Dhodapkar RS, Gandhi KN. Pharmaceuticals and personal care products in aquatic environment: chemicals of emerging concern? *Pharmaceuticals and Personal Care Products: Waste Management and Treatment Technology*: Elsevier; 2019:63-85.

39. Singh R, Hankins NP. Introduction to membrane processes for water treatment. *Emerging Membrane Technology for Sustainable Water Treatment.* 2016:15-52.

40. Sillanpää M, Metsämuuronen S, Mänttäri M, Silaanpää M. Membranes. *Natural organic matter in water: characterization and treatment method Butterworth-Heinemann, Oxford.* 2015:113-157.

41. Zhao Y. Chapter 2-Physical and Chemical Treatment Processes for Leachate. *Pollution Control Technology for Leachate from Municipal Solid Waste Butterworth-Heinemann.* 2018:31-183.

42. Zazouli M, Ulbricht M, Naseri S, Susanto H. Effect of hydrophilic and hydrophobic organic matter on amoxicillin and cephalexin residuals rejection from water by nanofiltration. 2010.

43. Khulbe K, Feng C, Matsuura T. Pore size, pore size distribution, and roughness at the membrane surface. Springer; 2008.

44. Guo W, Ngo H-H, Li J. A mini-review on membrane fouling. *Bioresource technology.* 2012;122:27-34.

45. Lee N, Amy G, Croué J-P, Buisson H. Identification and understanding of fouling in low-pressure membrane (MF/UF) filtration by natural organic matter (NOM). *Water research.* 2004;38(20):4511-4523.

46. Jiang S, Li Y, Ladewig BP. A review of reverse osmosis membrane fouling and control strategies. *Science of the Total Environment.* 2017;595:567-583.

47. Al-Juboori RA, Yusaf T. Biofouling in RO system: mechanisms, monitoring and controlling. *Desalination.* 2012;302:1-23.

48. Samsudin EM, Goh SN, Wu TY, Ling TT, Hamid SA, Juan JC. Evaluation on the photocatalytic degradation activity of reactive blue 4 using pure anatase nano-TiO2. *Sains Malaysiana.* 2015;44(7):1011-1019.

49. Chava RK, Son N, Kim YS, Kang M. Controlled growth and bandstructure properties of one dimensional cadmium sulfide nanorods for visible photocatalytic hydrogen evolution reaction. *Nanomaterials.* 2020;10(4):619.

50. Li Q, Li X, Yu J. Surface and interface modification strategies of CdS-based photocatalysts. *Interface science and technology.* Vol 31: Elsevier; 2020:313-348.

51. Kim J, Choi W. Hydrogen producing water treatment through solar photocatalysis. *Energy & Environmental Science.* 2010;3(8):1042-1045.

52. Nakata K, Fujishima A. TiO2 photocatalysis: Design and applications. *Journal of photochemistry and photobiology C: Photochemistry Reviews.* 2012;13(3):169-189.

53. Loeb SK, Alvarez PJ, Brame JA, et al. The technology horizon for photocatalytic water treatment: sunrise or sunset? : ACS Publications; 2018.

54. Naldoni A, Altomare M, Zoppellaro G, et al. Photocatalysis with reduced TiO2: from black TiO2 to cocatalyst-free hydrogen production. *ACS catalysis.* 2018;9(1):345-364.

55. Tian J, Hu X, Yang H, Zhou Y, Cui H, Liu H. High yield production of reduced TiO2 with enhanced photocatalytic activity. *Applied Surface Science.* 2016;360:738-743.

56. Park K-W, Kolpak AM. Optimal methodology for explicit solvation prediction of band edges of transition metal oxide photocatalysts. *Communications Chemistry.* 2019;2(1):1-10.

57. San Martín S, Rivero MJ, Ortiz I. Unravelling the Mechanisms that Drive the Performance of Photocatalytic Hydrogen Production. *Catalysts.* 2020;10(8):901.

58. Wei R-B, Huang Z-L, Gu G-H, et al. Dual-cocatalysts decorated rimous CdS spheres advancing highly-efficient visible-light photocatalytic hydrogen production. *Applied Catalysis B: Environmental.* 2018;231:101-107.

59. Ghosh A, Paul S, Raj S. Structural phase transformation from wurtzite to zinc-blende in uncapped CdS nanoparticles. *Solid state communications.* 2013;154:25-29.

60. Matsumura M, Furukawa S, Saho Y, Tsubomura H. Cadmium sulfide photocatalyzed hydrogen production from aqueous solutions of sulfite: effect of crystal structure and preparation method of the catalyst. *The Journal of Physical Chemistry.* 1985;89(8):1327-1329.

61. Kodigala SR. Fabrication and Properties of Window Layers For Thin Film Solar Cells. *Thin Films and Nanostructures.* Vol 35: Elsevier; 2010:393-504.

62. Li K, Han M, Chen R, et al. Hexagonal@ cubic CdS core@ shell nanorod photocatalyst for highly active production of H2 with unprecedented stability. *Advanced Materials.* 2016;28(40):8906-8911.

63. Haque SE, Ramdas B, Padmavathy N, Sheela A. Facile one-pot low-temperature solid-state approach towards phase transformation of nanoCdS. *Micro & Nano Letters.* 2014;9(10):731-735.

64. Yang X, Wang B, Mu Y, Zheng M, Wang Y. Photocatalytic performance of cubic and hexagonal phase CdS synthesized via different Cd sources. *Journal of Electronic Materials.* 2019;48(5):2895-2901.

65. Yuan SQ, Ji PF, Li Y, Song YL, Zhou FQ. Unusual blueshifting of optical band gap of CdS nanocrystals through a chemical bath deposition method. *Advances in OptoElectronics.* 2015;2015.

66. Liang Z, Shen R, Ng YH, Zhang P, Xiang Q, Li X. A review on 2D MoS2 cocatalysts in photocatalytic H2 production. *Journal of Materials Science & Technology.* 2020;56:89-121.

67. Jo W-K, Selvam NCS. Fabrication of photostable ternary CdS/MoS2/MWCNTs hybrid photocatalysts with enhanced H2 generation activity. *Applied Catalysis A: General.* 2016;525:9-22.

68. Campos-Roldán C, Alonso-Vante N. The hydrogen evolution reaction on nanostructured molybdenum disulfide. *Journal of the Mexican Chemical Society.* 2019;63(3):28-38.

69. Thomas N, Mathew S, Nair KM, et al. 2D MoS2: structure, mechanisms and photocatalytic applications. *Materials Today Sustainability.* 2021:100073.

70. Radisavljevic B, Radenovic A, Brivio J, Giacometti V, Kis A. Single-layer MoS 2 transistors. *Nature nanotechnology.* 2011;6(3):147-150.

71. Chang K, Hai X, Pang H, et al. Targeted synthesis of 2H-and 1T-phase MoS2 monolayers for catalytic hydrogen evolution. *Advanced Materials.* 2016;28(45):10033-10041.

72. Sahoo D, Kumar B, Sinha J, Ghosh S, Roy SS, Kaviraj B. Cost effective liquid phase exfoliation of MoS 2 nanosheets and photocatalytic activity for wastewater treatment enforced by visible light. *Scientific Reports.* 2020;10(1):1-12.

73. Liu Y, Yu Y-X, Zhang W-D. MoS2/CdS heterojunction with high photoelectrochemical activity for H2 evolution under visible light: the role of MoS2. *The Journal of Physical Chemistry C.* 2013;117(25):12949-12957.

74. Han B, Liu S, Zhang N, Xu Y-J, Tang Z-R. One-dimensional CdS@ MoS2 core-shell nanowires for boosted photocatalytic hydrogen evolution under visible light. *Applied Catalysis B: Environmental.* 2017;202:298-304.

75. Xu J, Cao X. Characterization and mechanism of MoS2/CdS composite photocatalyst used for hydrogen production from water splitting under visible light. *Chemical Engineering Journal.* 2015;260:642-648.

76. Zhang J, Zhu Z, Feng X. Construction of two-dimensional MoS2/CdS p–n nanohybrids for highly efficient photocatalytic hydrogen evolution. *Chemistry–A European Journal.* 2014;20(34):10632-10635.

77. He J, Chen L, Wang F, et al. CdS nanowires decorated with ultrathin MoS2 nanosheets as an efficient photocatalyst for hydrogen evolution. *ChemSusChem.* 2016;9(6):624-630.

78. Li Y, Wang L, Cai T, et al. Glucose-assisted synthesize 1D/2D nearly vertical CdS/MoS2 heterostructures for efficient photocatalytic hydrogen evolution. *Chemical Engineering Journal.* 2017;321:366-374.

79. Mohammed MK. Carbon nanotubes loaded ZnO/Ag ternary nanohybrid with improved visible light photocatalytic activity and stability. *Optik.* 2020;217:164867.

80. Saleh TA. The role of carbon nanotubes in enhancement of photocatalysis. *Syntheses and applications of carbon nanotubes and their composites.* 2013:479-493.

81. Zhao D, Zong W, Fan Z, et al. Synthesis of carbon-doped BiVO 4@ multi-walled carbon nanotubes with high visible-light absorption behavior, and evaluation of their photocatalytic properties. *CrystEngComm.* 2016;18(47):9007-9015.

82. Zhao Z, Yang Z, Hu Y, Li J, Fan X. Multiple functionalization of multi-walled carbon nanotubes with carboxyl and amino groups. *Applied surface science.* 2013;276:476-481.

83. Singh I, Birajdar B. Synthesis, characterization and photocatalytic activity of mesoporous Na-doped TiO 2 nano-powder prepared via a solvent-controlled non-aqueous sol–gel route. *RSC advances.* 2017;7(85):54053-54062.

84. Zhang G, Zhang Y, Bao S, Zhang L. A Novel Process for the Synthesis of NaV2O5 Mesocrystals from Alkaline-Stripped Vanadium Solution via the Hydrothermal Hydrogen Reduction Method. *Minerals.* 2019;9(5):271.

85. Benkahoul M, Zayed M, Solieman A, Alamri S. Spray deposition of V4O9 and V2O5 thin films and post-annealing formation of thermochromic VO2. *Journal of Alloys and Compounds.* 2017;704:760-768.

86. Ingham B, Toney M. X-ray diffraction for characterizing metallic films. *Metallic Films for Electronic, Optical and Magnetic Applications*: Elsevier; 2014:3-38.

87. Chen S, Wang Y, Li J, et al. Synthesis of black TiO2 with efficient visible-light photocatalytic activity by ultraviolet light irradiation and low temperature annealing. *Materials Research Bulletin.* 2018;98:280-287.

88. Tamiji T, Nezamzadeh-Ejhieh A. Electrocatalytic behavior of AgBr NPs as modifier of carbon past electrode in the presence of methanol and ethanol in aqueous solution: a kinetic study. *Journal of the Taiwan Institute of Chemical Engineers.* 2019;104:130-138.

89. Jung KY, Park SB, Ihm S-K. Linear relationship between the crystallite size and the photoactivity of non-porous titania ranging from nanometer to micrometer size. *Applied Catalysis A: General.* 2002;224(1-2):229-237.

90. Li Y, Du Q, Liu T, et al. Comparative study of methylene blue dye adsorption onto activated carbon, graphene oxide, and carbon nanotubes. *Chemical Engineering Research and Design.* 2013;91(2):361-368.

91. Wang R, Shi K, Huang D, Zhang J, An S. Synthesis and degradation kinetics of TiO 2/GO composites with highly efficient activity for adsorption and photocatalytic degradation of MB. *Scientific reports.* 2019;9(1):1-9.

92. Jayaraj SK, Sadishkumar V, Arun T, Thangadurai P. Enhanced photocatalytic activity of V2O5 nanorods for the photodegradation of organic dyes: a detailed understanding of the mechanism and their antibacterial activity. *Materials Science in Semiconductor Processing.* 2018;85:122-133.

93. Lv Y, Yao W, Ma X, Pan C, Zong R, Zhu Y. The surface oxygen vacancy induced visible activity and enhanced UV activity of a ZnO 1− x photocatalyst. *Catalysis Science & Technology.* 2013;3(12):3136-3146.

94. Omrani N, Nezamzadeh-Ejhieh A. Focus on scavengers' effects and GC-MASS analysis of photodegradation intermediates of sulfasalazine by Cu2O/CdS nanocomposite. *Separation and Purification Technology.* 2020;235:116228.

95. Raeisi-Kheirabadi N, Nezamzadeh-Ejhieh A. A Z-scheme g-C3N4/Ag3PO4 nanocomposite: Its photocatalytic activity and capability for water splitting. *International Journal of Hydrogen Energy.* 2020;45(58):33381-33395.

96. Wang C, Wu D, Wang P, Ao Y, Hou J, Qian J. Effect of oxygen vacancy on enhanced photocatalytic activity of reduced ZnO nanorod arrays. *Applied Surface Science.* 2015;325:112-116.

97. Yu Y-G, Chen G, Hao L-X, et al. Doping La into the depletion layer of the Cd 0.6 Zn 0.4 S photocatalyst for efficient H 2 evolution. *Chemical Communications.* 2013;49(86):10142-10144.

98. De Menezes B, Ferreira F, Silva B, et al. Effects of octadecylamine functionalization of carbon nanotubes on dispersion, polarity, and mechanical properties of CNT/HDPE nanocomposites. *Journal of materials science.* 2018;53(20):14311-14327.

99. Chai B, Xu M, Yan J, Ren Z. Remarkably enhanced photocatalytic hydrogen evolution over MoS2 nanosheets loaded on uniform CdS nanospheres. *Applied Surface Science.* 2018;430:523-530.

100. Liu H, Liu S, Zhang Z, Dong X, Liu T. Hydrothermal etching fabrication of TiO 2@ graphene hollow structures: mutually independent exposed {001} and {101} facets nanocrystals and its synergistic photocaltalytic effects. *Scientific reports.* 2016;6(1):1-12.

101. Peng Y, Li J, Qian X, Zhang J, Lin J. Photodeposition of ultrathin MoS 2 nanosheets onto cubic CdS for efficient photocatalytic H 2 evolution. *Journal of Nanoparticle Research.* 2018;20(4):1-8.

102. Syari'ati A, Kumar S, Zahid A, El Yumin AA, Ye J, Rudolf P. Photoemission spectroscopy study of structural defects in molybdenum disulfide (MoS 2) grown by chemical vapor deposition (CVD). *Chemical Communications.* 2019;55(70):10384-10387.

103. Pal M, Mathews N, Santiago P, Mathew X. A facile one-pot synthesis of highly luminescent CdS nanoparticles using thioglycerol as capping agent. *Journal of nanoparticle research.* 2012;14(6):1-13.

104. Poulose AC, Veeranarayanan S, Yoshida Y, Maekawa T, Kumar DS. Rapid synthesis of triangular CdS nanocrystals without any trap emission. *Journal of Nanoparticle Research.* 2012;14(4):1-10.

105. Kumar H, Bharti B, Aslam S, et al. Structural tailoring of molybdenum disulfide by argon plasma for efficient electrocatalysis performance. *International Journal of Energy Research.* 2020;44(9):7846-7854.

106. Liang S, Zhou Z, Wu X, et al. Constructing a MoS2 QDs/CdS core/shell flowerlike nanosphere hierarchical heterostructure for the enhanced stability and photocatalytic activity. *Molecules.* 2016;21(2):213.

107. Nadeem Riaz K, Yousaf N, Bilal Tahir M, Israr Z, Iqbal T. Facile hydrothermal synthesis of 3D flower-like La-MoS2 nanostructure for photocatalytic hydrogen energy production. *International Journal of Energy Research.* 2019;43(1):491-499.

108. Makuła P, Pacia M, Macyk W. How to correctly determine the band gap energy of modified semiconductor photocatalysts based on UV–Vis spectra. ACS Publications; 2018.

109. Liu X, Li J, Yao W. CdS@ MoS2 Hetero-structured Nanocomposites Are Highly Effective Photo-Catalysts for Organic Dye Degradation. *ACS omega.* 2020;5(42):27463-27469.

110. Wang S, Yun J-H, Wang L. Nanostructured semiconductors for bifunctional photocatalytic and photoelectrochemical energy conversion. *Semiconductors and Semimetals.* Vol 97: Elsevier; 2017:315-347.

111. Rahman IA, Purqon A. First principles study of molybdenum disulfide electronic structure. Paper presented at: Journal of Physics: Conference Series2017.

112. Pashley M, Haberern K, Feenstra R, Kirchner P. Different Fermi-level pinning behavior on n-and p-type GaAs (001). *Physical Review B.* 1993;48(7):4612.

113. Chen Z, Gong H, Liu Q, Song M, Huang C. NiSe2 nanoparticles grown in situ on CdS nanorods for enhanced photocatalytic hydrogen evolution. *ACS Sustainable Chemistry & Engineering.* 2019;7(19):16720-16728.